An investigation into complex inorganic materials with Mössbauer spectroscopy

Dissertation
zur Erlangung des Grades
"Doktor der Naturwissenschaften"
im Promotionsfach Anorganische Chemie

am Fachbereich Chemie, Pharmazie und Geowissenschaften
der Johannes Gutenberg-Universität Mainz

vorgelegt von
Verena Jung
geboren in Limburg / Lahn

Mainz, 2008

Contents

1 Introduction

Natural glasses have been used by mankind since ancient times. The earliest archaeological evidence of glass manufacturing dates at 7000 B.C. from a sample of glass unearthed in Egypt of probable Asian origin [1]. In the beginning glass was used purely for creation of ornamental objects. In the first century B.C. the handcraft of glass blowing was invented, and this allowed for the use of glass for practical purposes such as vessels, and windows in Roman times. The Romans further developed the art of glass blowing and introduced it to Germany where it experienced a period of prosperity centred around Cologne. After the fall of the Roman Empire glass manufacturing was dispersed to isolated sites [1, 2, 3].

The industrial production of glasses started at the turn of the last century. Around the year 1900 John H. Lubbers developed a method to produce glass by blowing large cylinders. The cylinders were then cut open and flattened [4, 3]. A further improvement came with the invention of the Fourcault method, which came into popular use after 1914. With this method glass could be produced continuously by lifting the glass as it forms to pass through a vertical cooling channel. By varying the lifting velocity the thickness of the glass sheet maybe controlled. Yet another improvement to this method was the development of the horizontal turn of the cooling channel, which came into use after 1917 and is known as the Libbey-Owens-process. Alternatively, flat glasses were produced as cast glass. That is produced by forming a band between cooled rolls, cutting it into plates and cooling it in a furnace. This process was further enhanced by the development of a method to produce a continuous ribbon of glass by forming the ribbon between rollers. This process was expensive, as the surface of the glass needed polishing. That was the starting point for the development of the float process [4, 3].

Float glass process

In 1959 the company Pilkington invented the float process [5, 3, 6]. Here the raw materials are mixed and fed into a furnace at 1500 ℃ to form a large pool of molten glass which then may be fed into a bath of molten tin through a delivery canal (see Figure 1.1). A refractory gate controls the amount of glass allowed to pour onto the molten tin. The tin bath is protected from oxidising by the presence of a forming gas consisting of a mixture of nitrogen and hydrogen. The ribbon is held at a high enough temperature for a long enough time for the irregularities to melt out and for the surface to become flat and parallel. The temperature in the float chamber is gradually reduced from 1100 ℃ to approximately 600 ℃ to cool the ribbon. At 1100 ℃ the melt is cast on the tin and at 600 ℃ the surfaces are hard enough for the sheet to be taken out of

the bath. Therewith a floating ribbon with a uniform thickness and a perfectly smooth glossy surface on both sides is formed.

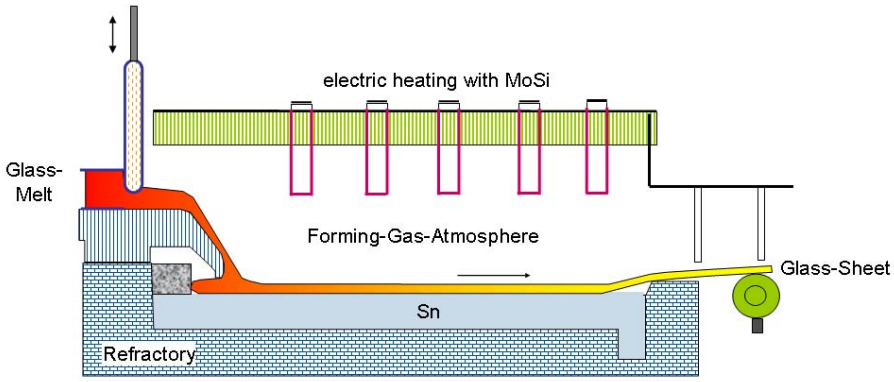

Figure 1.1: Scheme of a float bath.

A great advantage of this process is that in such a system the liquid surfaces become naturally flat and parallel. By varying the speed at which the ribbon is formed and by stretching the glass in a gentle and controlled way thicknesses between 3 mm and 15 mm can be produced. One determining factor for this process is the material on which the melt floats [7]. The requirements on a metal bath compress the number of possible metals. A suitable material should:

- be liquid between 600 ℃ and 1100 ℃
- have a density high enough to support the glass
- show little interaction with glass
- have a low toxicity and a low metal vapour pressure
- be readily available
- have low costs.

The only metal satisfying all these requirements is tin. Nevertheless, there are some disadvantages which restrict the usage of tin as a float bath material. First, in the presence of oxygen tin evaporates as SnO and in the presence of sulfur tin evaporates as SnS. Through condensation and reduction of these compounds small specks of tin

can be produced on the top surface of the ribbon. Second, in the presence of oxygen tin precipitates as SnO_2. Third, the ribbon absorbs Sn^{2+}. Subsequent heat treatment leads to an oxidation of Sn^{2+} to Sn^{4+}. This causes a bluish haze, which is called bloom. Consequently the concentrations of sulphur and oxygen should be reduced in the bath.

In conclusion, for every glass system the applicability has to be checked [7]. For instance if very high temperatures are necessary the evaporation of SnO and SnS can not be handled any more and defects on the surface of the glass ribbon appear. Additionally glass components such as P, Pb, As, Sb or Bi can react with the float bath. Consequently, glasses containing these elements to a high amount can not be fabricated by the float process. To produce glasses free of bubbles a refining agent is added to the glass mixture. For borosilicate glasses this is NaCl and for speciality glasses this can be oxides of As, Sb or Sn. As As and Sb can not be used in combination with the float process SnO_2 is frequently used as refining agent in speciality glasses such as display glasses. In these tin containing glasses other effects play an important role in combination with the float process. Evaporation of Sn^{2+} on the ribbon surface or "bloom on the top" due to interactions of the tin rich surface with the reducing atmosphere in the float bath then occurs.

^{119}Sn Mössbauer spectroscopy [8]

Mössbauer spectroscopy is an invaluable tool for the analysis of oxidation states and local structure in amorphous systems. As it is a local probe the environment of Mössbauer active atoms can be investigated even if their concentration is very low. Details of the ^{119}Sn Mössbauer spectroscopy follow below.

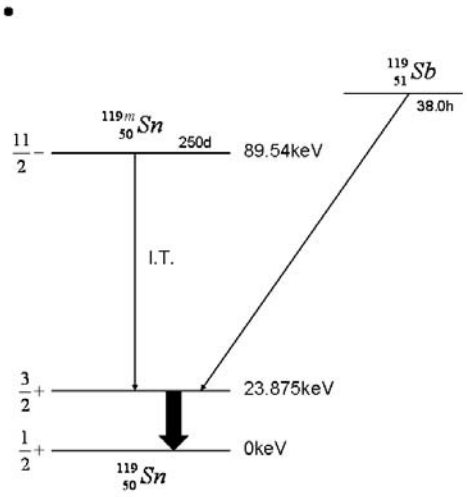

Figure 1.2: The decay scheme for ^{119m}Sn [8].

The 23.875 keV decay from the first excited state as shown in Figure 1.2 is the γ-ray transition used for Mössbauer spectroscopy. The radioactive ^{119m}Sn with a half life of 250 days and can be prepared in adequate activity by neutron capture in isotropically enriched ^{118}Sn. The 23.875 keV transition is a $\frac{3}{2} \rightarrow \frac{1}{2}$ magnetic dipole transition. The excited state lifetime of 18.3 $\pm$ 0.5 ns [8] corresponds to a linewidth following from a Heisenberg uncertainty relation of Γ_r=0.313 mm/s (see Figure 1.2). The most popular source material is $Ca^{119}SnO_3$, as it does not show line broadening due to the cubic symmetry of the matrix.

The 65.66 keV γ-ray are strongly converted and are consequently of low intensity. The resulting 25.04 and 25.27 keV x-rays can be preferentially absorbed by using a palladium filter, while measuring in transmission geometry. For measurements in reflection geometry, independent from the detected radiation (γ-rays, x-rays or conversion electrons) that is not needed. The information depth in conversion electron Mössbauer spectroscopy is $\approx$ 1 μm while the emitted x-rays monitor a depth of $\approx$ 10 μm (see Figure 1.3).

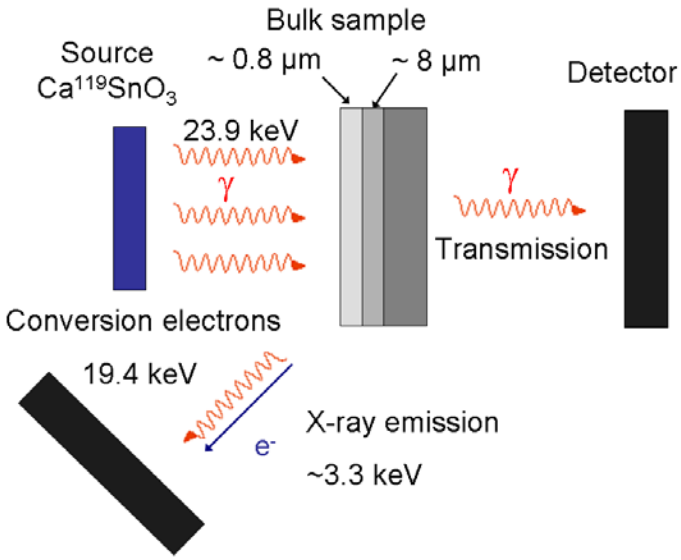

Figure 1.3: Probing depth in different kinds of Mössbauer experiments [9], Depth from which 90 % of the backscattered photons / conversion electrons emerge in the metallic tin probe. The absorption of the in going γ-rays and the emerging radiation is taken into account.

Using these methods, Mössbauer spectroscopic depth selective measurements can be performed. Despite the low tin concentrations in industrially produced samples ($\leq$ 0.5 wt% SnO_2) Mössbauer spectroscopy is sensitive enough to allow for the measurements of high quality spectra.

^{57}Fe Mössbauer spectroscopy

More than fifty per cent of all publications on Mössbauer spectroscopy are concerned with the Fe atom, researchers often concider Mössbauer spectroscopy and ^{57}Fe as synonymous. In this work it is used in combination with other methods such as x-ray diffraction to investigate local ordering in intermetallic compounds. The decay scheme of the ^{57}Co source is shown in Figure 1.4.

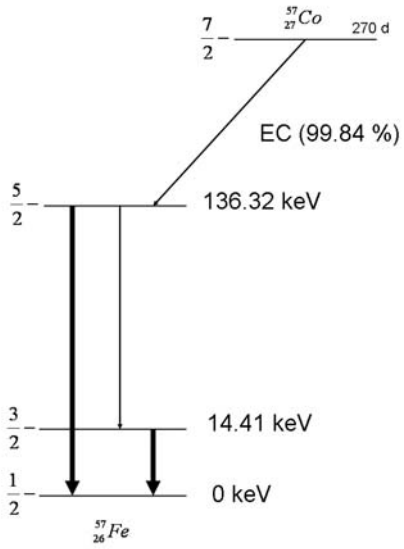

Figure 1.4: The decay scheme for ^{57}Co [8].

The exited state at 136.32 keV is populated by electron capture from ^{57}Co. The efficiency of this process is 99.84 % and the half life time of the ^{57}Co is 270 d. 85 % of the decays from the 136.32 keV level result in a 121.9 keV γ-ray and populate the first excited state at 14.41 keV efficiently. The transition from the first state excited with a spin quantum number 3/2 occurs to the ground state of spin 1/2. The lifetime of this level is about 99 ns and thus a Heisenberg width of 0.19 mm/s is obtained.

Local structure in silicate glasses

Until recently most of the advances in glass manufacturing were achieved empirically. One of the first researchers who studied glasses more systematically was Michael Faraday [10]. He investigated the electrolysis and the conductivity of melts, and also found out that the red colour of a gold ruby glass is due to very small gold particles [11].

Otto Schott was the first researcher who studied glass building oxides fundamentally and systematically. He investigated new glasses such as lithiumglass and produced samples in an extremely high homogeneity which made a spectroscopical investigation

possible. With this knowledge he developed glasses with novel optical properties and found borosilicate glasses as excellent material for optical lenses [12].

Zachariasen [13] and Warren [14] conducted pioneering research into the structure of glasses by studying the reasons why certain molecules are glass formers and developed the network hypothesis. Their research relied heavily upon the newly invented x-ray diffraction. A result of their study was the formulation of defined conditions which have to be fulfilled so that an oxide is able to build a three-dimensional network:

- The coordination number of the cation must be small (≈ 3 or 4).
- An oxygen atom is linked to not more than two cations.
- The oxygen polyhedra share only corners with each other, not edges or faces.
- At least three corners in each oxygen polyhedra must be shared with other polyhedra.

Under these rules B_2O_3, SiO_2, GeO_2 P_2O_5, As_2O_5, P_2O_3, As_2O_3,Sb_2O_3, V_2O_5, Sb_2O_5 and Ta_2O_5 were presumed to be network forming oxides.

With this model the structure of vitreous SiO_2 is regarded as a continuous random network of corner-sharing [SiO_4] tetrahedra. The bond lengths and bond angles within the tetrahedra are well defined. The random nature of the structure arises from the distribution of the Si–O–Si and torsion angels between the tetrahedra. An extension to this model is required to enable the accurate description of alkali silicate glasses. Whereby the alkali cations are regarded as network modifiers. When a network modifier is added, bridging oxygen atoms which connect two tetrahedra are replaced by two non-bridging oxygen atoms. In other words, a covalent bond transforms to an ionic bond. A reaction equation for which is shown in Figure 1.5.

For the description of alkali silicate glasses this model has to be extended.

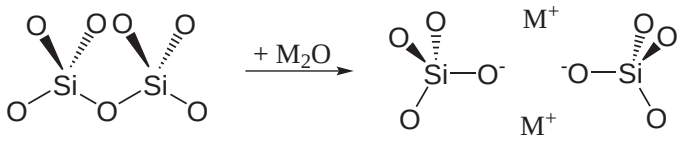

Figure 1.5: Bridging oxygen (BO) connecting two tetrahedra is replaced by two non-bridging oxygen atoms by the addition of a network modifier M_2O [15].

Zachariasen classified the cations in a glass in three groups [12]:

- network formers: Si, B, P, Ge, As with coordination numbers 3 or 4
- network modifiers: Na, K, Ca, Ba with coordination numbers 6 or more
- intermediate oxides: Al, Mg, Zn, Pb with coordination numbers between 4 and 6

The classification of Sn^{2+} and Sn^{4+} ions in a glass network and their coordination is still under investigation.

Thermodynamics of polyvalent glass components

The properties of glasses do not only depend on the chemical composition, but also on the oxidation state of polyvalent components. They are determined by the thermal and chemical boundary conditions of the production process. In tin containing samples the predominant equilibrium is:

$$Sn^{4+} + O^{2-} \rightleftharpoons Sn^{2+} + \frac{1}{2}O_2 \tag{1.1}$$

The equilibrium constant K can be derived as follows:

$$K' = \frac{a(Sn^{2+})\sqrt{pO_2}}{a(Sn^{4+})} = \frac{\gamma(Sn^{2+})[Sn^{2+}]\sqrt{pO_2}}{\gamma(Sn^{4+})[Sn^{4+}]} \tag{1.2}$$

with γ the activity coefficients and a the activities for Sn^{2+} and Sn^{4+}. Then

$$K = K'\frac{\gamma(Sn^{4+})}{\gamma(Sn^{2+})} = \frac{[Sn^{2+}]\sqrt{pO_2}}{[Sn^{4+}]} \tag{1.3}$$

The solubility and the vapour pressure of Sn^{2+} and Sn^{4+} in silicate glasses influence the activity coefficients and therewith the equilibrium constant. Sn^{2+} is highly soluble in silicate melts (up to 70 mol%), but it has also a high vapour pressure and therefore a high rate of evaporation. Contrarily Sn^{4+} has a very low solubility in pure SiO_2, and a low vapour pressure. This all influences the Sn^{2+}/Sn^{4+} ratio in the glass after the production.

The reduction of Sn^{2+} to Sn^0 does not appear in float glasses as Sn^0 was not observed by Mössbauer spectroscopy and square wave voltammetry [16]. In alkali free glasses the electrical conductivity is too low to obtain good results with square wave voltammetry. Therefore a small amount of Na_2O is added to the melt. If the amount of Na_2O is small enough the chemical equilibrium (Equation 1.1) is not influenced and the error of measurement can be neglected. This procedure is not always possible and it has to be checked if the assumption, that the chemical equilibrium is not influenced by the

addition of Na_2O is correct. For that reason Mössbauer spectroscopy is a powerfull tool, as it can be carried out in glasses. The equilibrium constant K is connected with the free enthalpie ΔG via the following Equation:

$$\Delta G = \Delta H - T\Delta S = -RTln\{K\} \tag{1.4}$$

ΔH and ΔS values of the melts can be determined by square wave voltammetry [17, 18, 19, 20, 21, 22, 23, 24, 25]. They are presented in the appendix.

Transport properties [1, 2, 12]

- Viscosity

The viscosity η of a glass is one of its most important physical properties. It determines for instance the melting conditions of a glass, the fining process and the further processing. The temperature dependency of the viscosity η can be described by the following empirical Equation:

$$\log \eta = A + \frac{B}{T - T_0} \tag{1.5}$$

A, B and T_0 are constants. A plot of that type is shown in Figure 1.6.

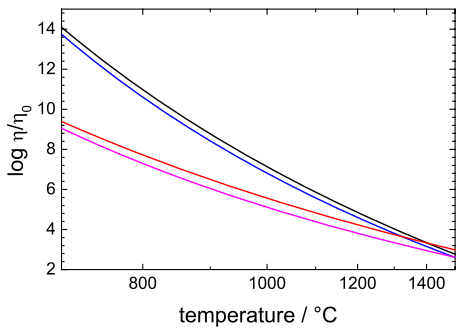

Figure 1.6: Arrhenius type plot of the viscosity against the temperature. The blue and the black lines correspond to alkali free borosilicate glasses, the red and the violet lines correspond to alkali containing borosilicate glasses.

As Figure 1.6 clearly illustrates the addition of alkalioxides lowers the viscosity of the glass. The slope of the curves for the alkali-free glasses is bigger than the slope for the curves of the alkali containing ones. On that account the alkali-free glasses are mentioned as “short” and the alkali containing ones as “long”. The viscosity is connected with the diffusion coefficient D_i of the networkforming units via the Stokes-Einstein Equation:

$$D_i = \frac{kT}{6\pi\eta r_i} \tag{1.6}$$

Where the parameter r_i is the radius of the moving unit i. It can be calculated by measuring the viscosity and the diffusion coefficient.

- Electrical conductivity and ionic diffusion

The electrical conductivity of virtually all oxide glasses results from ionic motion. In certain special compositions containing multivalent oxides - such as vanadium pentoxide or iron oxide - the conduction is electronic. The ionic conductivity of virtually all oxide glasses results from the transport of monovalent cations. In most commercial glasses the conducting ion is Na^+. Lithium ions also are quite mobile in oxide glasses. In some glasses impurities of monovalent ions suffice to determine the conductivity. If the electrical current in a glass is carried by a single ionic species the electrical conductivity is related to the diffusion of the ion by the Nernst-Einstein Equation:

$$\sigma = \frac{z^2F^2Dc}{RT} \tag{1.7}$$

Where σ is the electrical conductivity, z is the ionic charge, D is the diffusion coefficient, R is the gas constant, T is the temperature, and c is the concentration. Hence the electrical conductivity is proportional to the product of the concentration of the current-carrying ion and its diffusion coefficient. It can be used to determine the diffusion coefficient by measuring the electrical conductivity. That was done for an alkali-free special glass containing Ca^{2+} ions. The results are shown in Table 1.1.

Table 1.1: Diffusion coefficient from the electrical conductivity.

σ / $\Omega^{-1}cm^{-1}$	T / K	c / mol/cm^3	D / cm^2/mol
0.00208	1670	$5.71 \cdot 10^{-3}$	$1.36 \cdot 10^{-7}$

It was shown that with Equations 1.7 and 1.6 the Diffusion coefficients can be determined by measurements of the electrical conductivity or the viscosity. Alternatively that can be done by analysing depth profiles after diffusion experiments on a special setup. Subsequent description of the data with a solution of Ficks second law results in a determination of the diffusion coefficients.

When a glass is placed in contact with a medium containing monovalent cations these cations can exchange with the monovalent cations in the glass and interdiffusion phenomena will take place. To preserve electrical neutrality the fluxes J of the two ions must be equal and opposite. The fluxes for ionic transport in the ξ direction are defined by the Nernst-Planck Equation:

$$J = -u\left(RT\frac{\partial c}{\partial \xi}\frac{\partial lna}{\partial lnc} + zcFE\right) \tag{1.8}$$

where a is the thermodynamic activity, c is the concentration, F is the Faraday constant, E is the electrical potential, and u is the mobility of the ion. The mobility u is connected to the Diffusion coefficient D of the ion by: $u = \frac{D}{RT}$. If two monovalent cations A and B interdiffuse, each has a flux J equals Equation 1.8. The conditions of neutrality requires that $J_A = -J_B$.

Then the chemical diffusion coefficient can be written as:

$$\tilde{D} = \frac{D_A D_B}{x_A D_A + x_B D_B} \cdot \frac{\partial lna}{\partial lnc} \tag{1.9}$$

State of the art and aim of the study

With the development of the float process understanding the role of tin in silicate glasses has become a fundamental challenge to the industry. The questions of interest are:

- How are Sn^{2+} and Sn^{4+} coordinated in the glass matrix?
- Are there influences from other components like alkali metals on the Sn polyeder?
- How does thermal treatment change the Sn^{2+}/Sn^{4+} ratio?
- What is the diffusion rate of tin ions in the silicate melt?

In 1976 Dannheim *et al.* examined laboratory made ternary SiO_2–Na_2O–SnO_x and quarternary SiO_2–Na_2O–Al_2O_3–SnO_x samples with Mössbauer spectroscopy [26]. Dannheim found that the Sn^{2+}/Sn^{4+} ratio could be shifted under oxidising or reducing atmospheres, and glasses containing only Sn^{2+} or Sn^{4+} were prepared. As the concentration of Na^+ was increased a change in the isomer shift of ^{119}Sn Mössbauer spectra was observed. For both tin species coordination numbers of four and six were recommended. Also Conversion Electron Mössbauer Spectroscopy (CEMS) was successfully implemented for the investigation of tin in float glass. Principi *et al.* started their investigations on original float glasses to compare both surfaces of the float ribbon [27]. The side which was in contact to the reducing atmosphere was more reduced than the side which was in contact to the tin bath. Nishida determined the Debye temperatures of WO_3 and P_2O_5 glasses using low temperature Mössbauer spectroscopy [28]. The role of the two Sn species was discussed and Sn^{4+} was proposed to be a network former (NWF). Until 1994 it was shown that Mössbauer spectroscopy may be employed to accurately examine the following factors:

- The oxidation state
- The local surrounding of the tin atoms
- The behaviour as network forming or netword modifying oxide
- Reduction or oxidation due to the applied atmosphere
- Influences from other glass components on the local surrounding of the tin atoms.

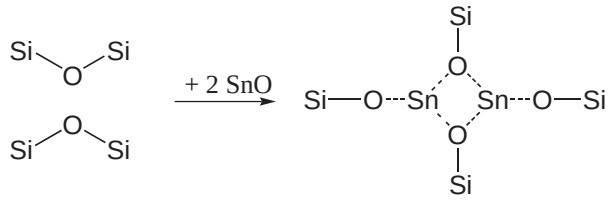

Figure 1.7: A possible configuration for the inclusion of three-coordinated tin in a silicate glass network [29].

A more systematic investigation began when Johnson *et al.* [30] and Bent *et al.* [29] concerned themselves with binary SiO_2–SnO systems. Johnson *et al.* used Mössbauer spectroscopy for their work, while Bent *et al.* performed their study with neutron diffraction. In the work of Bent *et al.* the local surrounding of Sn^{2+} were found to exist as a $[Sn^{II}O_3]$ triangular pyramid. A model of a possible configuration is presented in Figure 1.7.

The study of Johnson *et al.* [30] investigated binary SiO_2–SnO glasses and tin doped float glass. A solubility of Sn^{2+} in SiO_2 up to 70 mol% was observed in binary glasses. By contrast a low solubility of Sn^{4+} in SiO_2 due to its proposed octahedral coordination was reported. The quadrupole splittings observed for Sn^{2+} were found to be much higher than for amorphous or crystalline SnO, this was interpreted to be due to a distortion within the structure. Additionally, a decrease in the Sn^{2+} isomer shift with increasing SnO content is reported. The Debye temperatures were determined to be 364 K for Sn^{4+}, and 206 K for Sn^{2+}.

The influence of alkali metals on the local surrounding of Sn in silicate glasses can be investigated by the study of ternary SiO_2–M_2O–SnO glasses with M = Li, Na, K, Rb. Such experimentation was carried out by Johnson *et al.* [31] and Holland *et al.* [32]. Johnson *et al.* utilised both Mössbauer spectroscopy and neutron diffraction. They used the model of a three coordinated Sn^{2+} atom with additional M^+ ions for charge compensation. The larger the modifier ion, the more compact the polyhedron became around the tin. A model for the local surrounding of the Sn^{2+} ions as proposed by Johnson *et al.* is given in Figure 1.8.

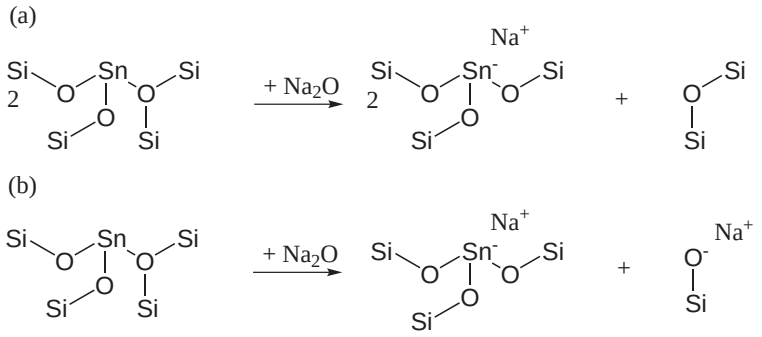

Figure 1.8: Models for the structure of stannosilicate glasses in the neighbourhood of the tin atoms for bonding (a) and non-bonding (b) oxygens [31].

Holland *et al.* [32] worked with ^{29}Si and ^{119}Sn Nuclear Magnetic Resonance (NMR) and ^{119}Sn Mössbauer spectroscopy. The local surrounding was presumed to be a distorted [$Sn^{II}O_3$] polyhedron with the additional M^+ ions for charge compensation, where the O–Sn–O angle depend on the radius of the M^+ ion. The presence of the M^+ counterion in the [$Sn^{IV}O_4$] and [$Sn^{IV}O_6$] polyhedra was assumed for local charge balancing. The occurrence of M^+ stabilises Sn^{4+} in the glass matrix.

The effect of Sr atoms on the structure of stannosilicate glasses was examined by Johnson *et al* [33]. They found Sn^{2+} forming [$Sn^{II}O_3$] trigonal pyramids. As the Sn–Sn distance is too big for edge sharing polyhedra, a connection through one oxygen atom only is assumed. A suggested reaction scheme for the incorporation of tin and strontium in a silicate network is shown in Figure 1.9.

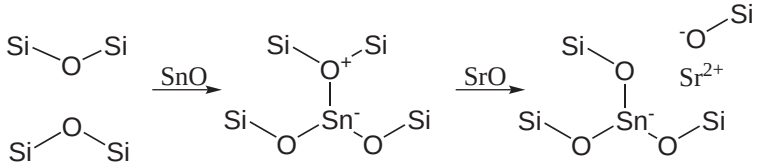

Figure 1.9: Incorporation of strontium in tin silicate glasses [33].

Besides alkaline and alkaline earth oxides, Al_2O_3 is also a widely used component in silicate glasses. For this reason Benne *et al.* [34] examined Na_2O–Al_2O_3–SiO_2 melts. The effect of alumina on the Sn^{2+}/Sn^{4+} redox equilibrium and the incorporation of tin were in the focus of the study. The Sn^{2+} and Sn^{4+} fractions calculated by Mössbauer spectroscopy were in good agreement with the values obtained from the square wave voltammetry. The Sn^{4+} and Sn^{2+} doublets were asymmetric, and therefore average isomer shift (IS) and quadrupole splitting (QS) values could be determined. An increase of the alkali concentration was associated with a stabilisation of the Sn^{4+} ions, whereas an increase in alumina concentrations was related to the destabilisation of Sn^{4+}. A direct influence of the alumina and the alkali concentration on the isomer shift and

quadrupole splitting of the Sn^{4+} ion was found. An octahedral environment with two additional Na^+ ions was presumed. As the alumina concentration is increased, coordinations of Sn^{4+} with an increasing number of non-bridging oxygen ions are favoured. The increase of the alumina concentration has no significant influence on the isomer shift of the Sn^{2+} ion, but on its quadrupole splitting. The increasing quadrupole splitting of the Sn^{2+} ion is related to an increase in the asymmetry of the local surrounding. A fourfold coordination of the Sn^{2+} ion is presumed. Here the Sn^{2+} ion is located at the apex of a square pyramid. These results correlate well with th findings of Benne *et al.* [23]. Potential shift in the square wave voltammograms can also be used to investigate the bonding and the interaction of the different glass components. This lead to the following conception [16]. In the peralkaline range, where the concentration of Na_2O is higher than the concentration of Al_2O_3 all aluminum atoms are surrounded by four oxygen atoms and form a tetrahedra. The charge equalisation of the tetrahedra is achieved by coordination to Na^+ ions. The supernumerous Na^+ ions stabilise the $[Sn^{IV}O_6]$ octahedra. In the peraluminous range the concentration of Na_2O is smaller than the concentration of Al_2O_3 and Na^+ions are no longer available to compensate the charge of the $[Sn^{IV}O_6]$ octahedra. Also the charge of the $[AlO_4]$ tetrahedra can not be compensated, resulting in the formation of octahedral or triclusters. These species are also cationic and may stabilise the $[Sn^{IV}O_6]$ octahedra. In glasses containing alkaline earths but alkaline metals analogous phenomena are observed [24]. Similar analysis was performed by McKeown *et al* [35] and Ellison *et al* [36]. They concentrated on the coordination of Sn^{4+} and on the effects of Al and alkali ions as well. The local surrounding of several silicate glasses were investigated by McKeown *et al* [35] with extended x-ray absorption fine structure analysis (EXAFS). In this study the Sn^{4+} ions were octahedraly coordinated in most of the glasses. In a float glass an octahedral and a tetrahedral surrounding were determined. In samples with a Sn concentration higher than about 1 wt% Sn-Sn distances indicating corner- or edge-sharing octahedra were asserted. On a series of SiO_2–Al_2O_3–K_2O–SnO_2 glasses the influences of K and Al and their ratio to the coordination of Sn^{4+} were studied. Ellison *et al* [36] worked on the same problem in 1998 and found the following rule: Sn is mostly six-coordinated for K_2O/Al_2O_3 molar ratios less than one. In these cases the SnO_2 solubility is relatively low and constant. If the K_2O/Al_2O_3 molar ratios exceeds one, an increase in the SnO_2 solubility is observed. Here the Sn and K content can be linked. This additional Sn^{4+} in the glass would likely be four-coordinated within K_4SnO_4 clusters. McKeown *et al* found predominantly $[Sn^{IV}O_6]$ environments, although some $[Sn^{IV}O_4]$ may be present in the SiO_2–Al_2O_3–K_2O–SnO_2 glasses.

Besides direct investigations of the structure, indirect examinations of the physical properties also offer a potential way to understand the role of Sn^{2+} and Sn^{4+} in silicate glasses. Such a study was undertaken by Krohn *et al.* [37], with the study of the effect

of tin-oxide on the physical properties of Na_2O-CaO-SiO_2 glass. They found that Sn^{4+} is more strongly bound in the glass structure than Sn^{2+}. So the network in a glass containing Sn^{4+} is more connected compared to a glass containing Sn^{2+}.

Johnson *et al.* [38] published a review devoted to the role of iron and tin in silicate glasses. Their work established the behaviour of Fe^{2+} as a network modifier occupying octahedral sites. Fe^{3+} was found to be a network former occupying tetrahedral sites. The lines in the ^{119}Sn Mössbauer spectra are always broad, thus the fitting was performed with a distribution of quadrupole doublets and the isomer shift and quadrupole splitting data were quoted as averages. Sn^{2+} was believed to be four or less coordinated and a Debye temperature of 180 K was determined. Sn^{4+} is considered to be sixfold coordinated with a Debye temperature of 220 K. Sn^{2+} was assessed to act as a conditional glass former in silicate glasses. Sn^{4+} was regarded as network modifier, which destroys the matrix. Additionally, depth-depended measurement at float glasses were described and a diffusion and reaction model was presented.

Investigation into the diffusivity and the incorporation of tin has been conducted by numerous groups. Again Mössbauer spectroscopy has proved to be a successful technique for obtaining information about the oxidation state of tin in float glasses. It has been shown that the majority of tin in industrially produced soda-lime-silica glasses was Sn^{2+} [39] and the take-up of tin to be higher at the edges of the float bath, than in the centre. A depth profile was obtained by removing substance from the bottom surface of the samples. It was discovered, that Sn^{2+} content is six or seven times that of Sn^{4+} in the first μm. A qualitative model to explain the tin hump in industrially produced samples was developed by Heide *et al.* [40]. This was done by measuring the concentration profiles of Sn and Fe and the Sn^{2+}/Sn^{4+} ratio by depth-profiling analysis techniques and conversion electron Mössbauer spectroscopy. The interaction between iron and tin was used to explain the tin anomalies. Another qualitative reaction diffusion mechanism has been introduced by Hayashi *et al.* [41]. Again the interaction between $Sn^{2+} \leftrightarrow Sn^{4+}$ and $Fe^{2+} \leftrightarrow Fe^{3+}$ plays an important role. Underlying depth profiles were obtained using Secondary Ion Mass Spectrometry (SIMS). Takeda *et al.* [42] found a tin enriched surface layer with SIMS of $^{18}O_2/N_2$ treated soda-lime-silica float glasses. With TEM analysis nanometer SnO_2 particles were clearly observed in the tin enriched layer. Additionally it was confirmed, that the mobile Sn species is the Sn^{2+}. Ehrt *et al.* [43] showed that effective reduction of Sn^{4+} to Sn^{2+} in alkalifree alumosilicate glasses is only possible at temperatures above 1700^{o}C. At 1800^{o}C after 1 h about 50% of the tin was Sn^{2+} and at 1900^{o}C only Sn^{2+} was present. The determination of diffusion coefficients in melts can be done by square wave voltammetry. Increasing alkali concentration in $Na_2O/CaO/Al_2O_3/SiO_2$ melts caused decreasing diffusion coefficients and increasing Al_2O_3 concentration leaded to an increase [21]. Increasing Na_2O concentration in Na_2O/SiO_2 and $Na_2O/CaO/SiO_2$

melts leaded at the same temperature to an increasing diffusion coefficient. At the same viscosity it caused a decrease [44]. This is due to a stronger incorporation of Sn^{4+} in the silicate network.

In summary, the coordination number of Sn^{4+} is presumed to be four or six. Sn^{2+} is supposed to be threefold coordinated with Sn^{2+} locating at the apex of a trigonal pyramid. Sn^{4+} is network forming whereas Sn^{2+} is network modifying. Alkali ions are directly bound to the Sn^{2+} polyhedra and affect their geometry. However, the mentioned analysis has been performed with only one doublet for each species, or with a distribution of many doublets for each species in Mössbauer spectra. With one only doublet for each oxidation state the asymmetric form of the lines can not be accurately described. A broad distribution of lines describes the asymmetric lines well, but it disagrees with the model of structural units [45]. A good quality analysis is performed with a defined number of lines for each oxidation state, where these lines correspond to a defined structural element in the glass.

The aim of this study is to develop a detailed model on the local surrounding of tin in silicate glasses. For this purpose, ^{119}Sn Mössbauer spectroscopic analysis is combined with theoretical investigations of the electron density at the nucleus and the electric field gradient in Sn clusters. Additionally, Extended X-ray Absorption Fine Structure (EXAFS) measurements are performed. The Mössbauer relative intensities of the Sn^{2+} and the Sn^{4+} lines are proportional to their contents. Thus redox and diffusion phenomena of the different tin species were clarified. In the course of this study, several tempering experiments were accomplished and industrially important process parameters such as the oxygen partial pressure (pO_2) in the atmosphere, the duration of tempering or the cooling process were varied. Finally, a novel diffusion-reaction model is developed.

2 Experimental and calculational details

2.1 Preparation of the model glass

The samples were prepared in a two-step process. In the first step, a mixture of SiO_2, Al_2O_3, B_2O_3, $CaCO_3$ and SnO_2 with compositions as shown in Table 2.1 was placed in a Pt-crucible and heated. Three mixtures with a SnO_2 content of 0.1, 0.3 and 0.5 wt% were used.

Table 2.1: Initial composition of the components of laboratory samples.

	M1	M3	M5
SiO_2 / wt%	62.19	62.02	61.94
Al_2O_3 / wt%	16.05	16.02	15.98
B_2O_3 / wt%	8.02	8.01	7.99
$CaCO_3$ / wt%	13.64	13.61	13.59
SnO_2 / wt%	0.1	0.3	0.5

The heating procedure is shown in Table 2.2 . The samples were initially heated to 1450 ℃ with 150 K/h for 1 h to melt. Then the fining procedure was applied and the melt was heated with a rate of 150 K/h to 1580 ℃ for 3 h. When the furnace reached 1580 ℃ an air injector was lowered into the Pt-crucible to reside a few mm above the crucible bottom. Consequently air bubbles ran through the melt and affected stirring of the mixture. In the next step the melt was cooled at a rate of 150 K/h to 1500 ℃ for 1 h and the injector was removed. For conditioning the melt was cooled at 150 K/h to 1450 ℃ over a duration of 3 h. Allowing time for all the remaining air cavities to rise and escape. The melt was then allowed to cool to room temperature. The glasses prepared in this manner were used for further experiments depending on the process parameters: oxygen partial pressure (pO_2), temperature (T), and time (t).

Table 2.2: Heating procedure for laboratory prepared samples.

step	Heating rate	End temperature	Duration
Melting	150 K/h	$\rightarrow$ 1450 ^{o}C	1 h
Fining	150 K/h	$\rightarrow$ 1580 ^{o}C	3 h
Bubbling	150 K/h	$\rightarrow$ 1500 ^{o}C	1 h
Conditioning	150 K/h	$\rightarrow$ 1450 ^{o}C	3 h
Cooling	150 K/h	$\rightarrow$ 25 ^{o}C	

2.2 Mössbauer spectroscopy

The ^{119}Sn-nucleus was used for performing Mössbauer measurements in transmission geometry, employing a $Ca^{119m}SnO_3$ Mössbauer source with resonance energy 23.88 keV. The glasses were measured as 1.5 mm to 2 mm thick discs with a diameter of 22 mm. A Pd-foil filter with characteristic absorption of 24.35 keV was used to suppress the background 25.04 keV radiation [8]. The experiments were performed with a spectrometer with a flow-gas cryostat using liquid N_2. Analysis of the spectra was performed with the EFFINO software package [46].

The spectra were analysed in a two-step process. Firstly they were summed in groups of 12 to 15 spectra with each experiment forming a group. The spectra of each group were evaluated parallel with the same hyperfine parameters. As good quality analysis requires four doublets each group consequently provided four isomer shift values and four quadrupole splitting values. They are presented in Table 2.3.

Table 2.3: Hyperfine parameters of all analysed groups of spectra.

group	IS/ mm/s	QS/ mm/s	IS/ mm/s	QS/ mm/s	IS/ mm/s	QS/ mm/s	IS/ mm/s	QS/ mm/s
1: Chapter 3.2	-0.155	0.335	-0.086	0.892	2.955	2.105	3.399	2.046
2: Chapter 3.5	-0.136	0.318	-0.094	1.105	3.055	2.133	3.643	1.981
3: Chapter 3.3	-0.129	0.473	-0.068	1.254	3.172	2.047	3.969	1.663
4: Chapter 3.4	-0.152	0.356	-0.095	0.836	3.046	2.068	3.458	2.025
5: Chapter 3.5	-0.129	0.537	-0.056	1.396	3.149	2.041	3.771	1.834
6: Chapter 3.6	-0.16	0.44	-0.09	0.76	3.26	1.90	3.14	2.21
7: Chapter 3.3	-0.128	0.478	-0.059	1.158	2.963	1.949	3.423	1.886

In the second step the average of the hyperfine parameters from Table 2.3 was taken. Every group was oncemore analysed with the obtained four doublets, an example for an analysed spectrum is presented in Figure 2.1. The green and the yellow doublets at 0 mm/s correspond to Sn^{4+} the blue and the red doublets at 3-4 mm/s correspond to Sn^{2+}. The relative intensity of the Sn^{4+} line with the large quadrupole splitting (yellow line) is smaller than the relative intensity of the Sn^{4+} line with the small quadrupole splitting (green line). The main difference between the two Sn^{2+} lines is the isomer shift. The relative intensity of the Sn^{2+} line at 3 mm/s (blue line] is higher than the relative intensity of the Sn^{2+} line at 3.6 mm/s. As the hyperfine parameter are the same for all analysed spectra, differences between the spectra are always reflected in changes of the relative intensities of the four doublets.

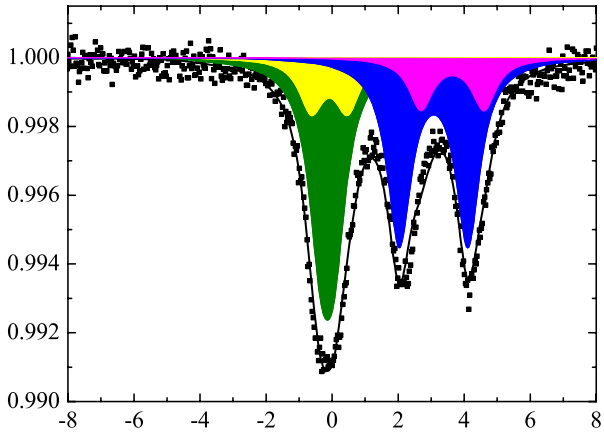

Figure 2.1: ^{119}Sn Mössbauer spectrum of a model glass.

2.3 EXAFS

Extended x-ray absorption fine structure spectroscopy (EXAFS) is widely used for the structural investigation into non-periodic materials and statistically disordered systems. Because of the $1/R^2$ and the $e^{-R/\lambda}$ dependency of the EXAFS oscillations $\chi(k)$, where R is the distance to the neighbouring atom and λ is the mean free path, EXAFS is a local probe and only a view shells around the probe atom contribute. Thus, with EXAFS it is possible to determine the nearest neighbour distances and the coordination number of the neighbours in crystalline and amorphous materials [47, 48, 49, 50, 51].

Besides Sn, the glass samples contain the elements Al, B, Ca, Si, and O. Therefore, EXAFS investigations at the tin L-edges were not suitable because contributions from other elements like calcium were leading to an overlap of fine structure oscillations and could therefore not be used easily for structural investigations. The Sn K-edge at 29.2 keV was used as it was free of influences from other elements. EXAFS data was collected at the XAS beam line of the ANKA in Karlsruhe. Transition, fluorescence and reference spectra were gathered simultaneously for each sample. At least three data sets were collected for each sample. For most samples six spectra were collected. They were merged together to produce one spectrum for analysis. The analysis was performed with the ifeffit software package [52].

An indication for the quality of an EXAFS spectrum is the edge step $\Delta\mu_0$, which is a function of the concentration of the measured atom [48, 49, 50, 51]. As the Sn concentrations in the glasses are small the edge steps are also small, some values of which are given in Table 2.4. Thus it is not possible to use the transmission data for further analysis and the fluorescence spectra were taken into account instead.

Table 2.4: Edge steps of original glass samples.

c(Sn) / wt% SnO_2	$\Delta\mu_0$
0.1	0,023
0.3	0,046
0.5	0,100

The k^2 weighted $\chi(k)$ data, the Fourier transformed and the reverse Fourier transformed data of the original glass samples are presented in Figure 2.2.

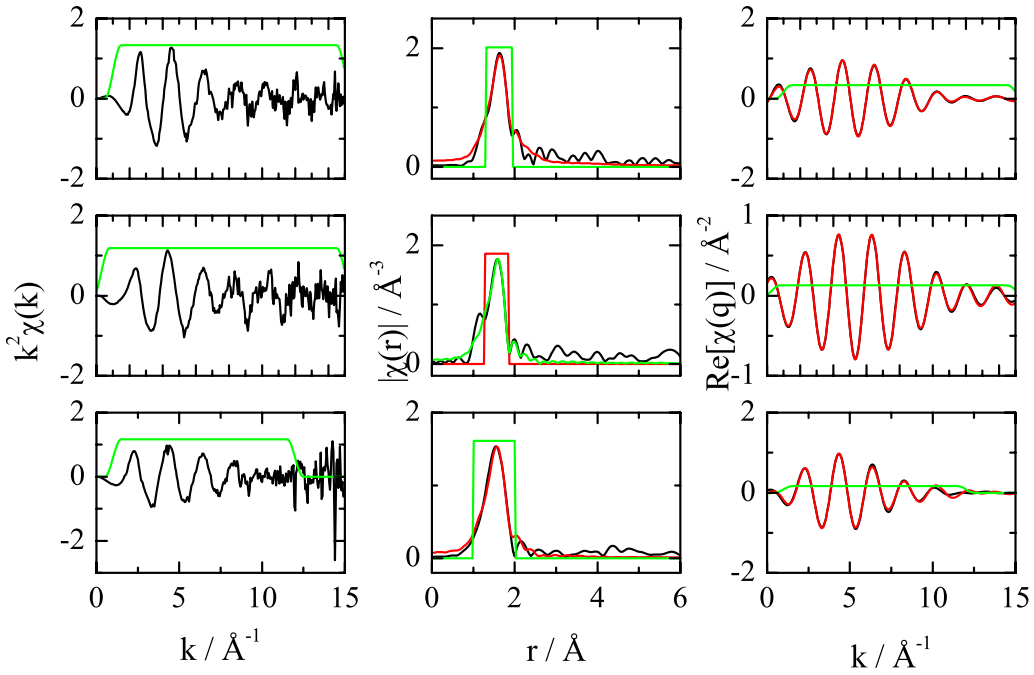

Figure 2.2: Shown are the $k^2\chi$ the Fourier transforms and the back transforms of the original glass samples. Data is always in black, the fit is in red and the Hanning window is plotted in green. The spectra in the first line belongs the sample with 0.1 wt% SnO_2, the spectra in the middle line to the sample with 0.3 wt% SnO_2 and the last line belong to the sample with 0.5 wt% SnO_2.

After the removal of the background the isolated EXAFS is k^2 weighted. This data is presented in the first column of Figure 2.2. A Hanning window determines the upper and the lower limits of the data. It is always defined as big as possible. So the upper limit in the lower graph in the first column of Figure 2.2 is set to 12 $Å^{-1}$. In the other two graphs the whole range up to 15 $Å^{-1}$ is taken into account. Then a Fourier transformation is performed into the r-space and the $|\chi(r)|$ data are plotted against the distance r in the second column of Figure 2.2. These graphs give a first

impression of the environment of the Sn atoms in the glass samples. In all three graphs a large peak at about 1.8 Å, due the Sn–O nearest neighbours is observed. At larger distances only small features are visible. The first peak is cut with a Hanning window for performing the backward Fourier transformation. The resulting graphs are shown in the last column of Figure 2.2. A first nearest neighbour Sn–O environment is used to fit the data. This fit data is presented in red lines in Figure 2.2. The same procedure is performed with all other EXAFS data.

2.4 Theoretical investigation

For defining and optimising the structure calculations were performed using the Materials Studio 4.1 program package from Accelrys [53]. The basic silicate structures were calculated using the Materials Studio Visualizer environment. Subsequently the Amorphous Cell module within the Materials Studio software package was used to build a cell containing silicate and counter ions as necessary. Afterward the geometry of this composite was optimised with the Forcite force field-package (ultra fine convergence criteria Energy change $\Delta E \leq 2.0 \cdot 10^{-5}\ \frac{kcal}{mol}$, force change $\Delta F \leq 0.0001\ \frac{kcal}{mol A^o}$ and displacement $\Delta r \leq 1.0 \cdot 10^{-5}$ Å per step, COMPASS force field [54], Ewald-summation).

For calculating the electron densities and the electric field gradients at the nucleus the WIEN2k software package was used [55]. The self-consistent electronic structure calculations were carried out using the scalar-relativistic full potential linearised augmented plane wave method (FLAPW) as provided by WIEN2k. The exchange-correlation functional was taken within the generalised gradient approximation (GGA) in the parameterisation of Perdew *et al* [56]. For obtaining values most near to the nucleus the $R0$ - parameter is set to 10^{-8} Bohr; the smallest possible value. The energy convergence criterion and the charge convergence criterion were set to 10^{-4} Ry.

2.5 Diffusion

For the determination of the diffusion coefficients the Comsol Multiphysics 3.4 software package was used. Three different models were developed for the analysis. These will be explained in Chapter 5.3.

3 Results and discussion of the Mössbauer and EXAFS data

3.1 Introduction

During the float process many parameters determine the properties of the final product. Various reactions at the tin-glass and at the glass-atmosphere interface have to be regarded. SnO_2 can be added purposefully as refining agent as in display glasses and not just as a result of the diffusion of Sn^{2+} from the bath into the ribbon. Furthermore evaporation at the atmosphere-glass boundary also plays a decisive role in affecting the Sn concentration. Mössbauer and EXAFS spectroscopy allows for the investigation into the local environments of the tin atoms, furthermore Mössbauer spectroscopy maybe used to measure the oxidation states of the tin atoms. The expected modifications of the coordination and the oxidation statse of the tin atoms are small and also the total tin content in the samples is extremely small. To investigate these changes in detail a methodical approach is needed. Therefore the relevant parameters such as the oxygen partial pressure of the atmosphere, the duration of the heat treatment and the tin concentration in the samples were systematically varied. An overview of the experiments is shown in Figure 3.1, where each point represents a single one experiment.

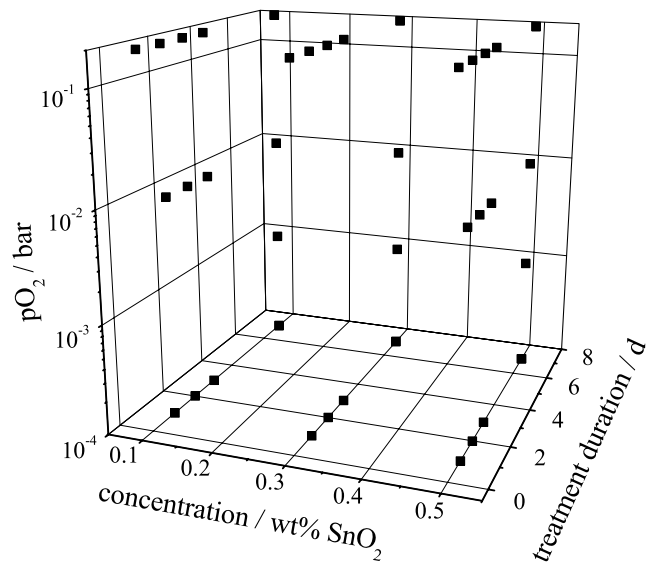

Figure 3.1: Overview of experiments

In experiments conducted on the laboratory scale it was also possible to diversify the cooling rates. This influences the environments of the tin atoms in the glasses and is also a topic of interest within this chapter.

For the investigation of diffusion processes it is necessary to perform time or depth dependent measurements [39, 41] of the oxidation state of the atom under investigation. The low tin concentration makes it difficult to determine the oxidation state of the tin, but Mössbauer spectroscopy has proved to be a successful technique for obtaining this information. In this chapter depth profiles of the Sn^{2+}/Sn^{4+} ratio after treatment in reducing atmosphere in varying probing depths are determined. Therefore a step by step polishing and measuring procedure was performed.

The alkaline and alkaline earth metals are known to behave as network modifying atoms that influence the network in the glasses. The physical properties such as the glass temperature T_g maybe modified by varying alkaline or alkaline earth meatl concentrations. The influence of these metal species on the environments and the oxidation states of the Sn-atoms is still a subject of interest. An idea of the interaction of Sr^{2+} on the Sn^{2+} environment is given by Johnson *et al.* [33] as illustrated in Figure 1.9. Whether this phenomenon maybe transferred to the effect of Ca^{2+} on the Sn^{2+} and the Sn^{4+} environment was investigated, and is discussed in due course in this chapter. In the course of this study, Ca^{2+} is added to the model glass and the mixture is re-melted and the local environment of the tin atoms were monitored with ^{119}Sn Mössbauer spectroscopy.

3.2 Influences of varying oxygen partial pressure on the chemistry of tin in silicate glasses

Sample preparation

All experiments with variable pO_2 were performed in a Linn High Term, HT 1300 furnace. In order to apply different atmospheres air, N_2 and N_2-air-mixtures were passed through the furnace during the heating process. To allow for control over the pO_2 in the atmosphere, a ZrO_2-sensor was placed inside the furnace, positioned not more than 5 cm above the samples. Before the experiments in flowing gas mixtures were conducted, the correct ratio of N_2 to air flow had to be adjusted. For this reason, the furnace was heated first to 1400 ^{o}C without a sample. In the hot furnace the flow of the two gases was then regulated. When the desired pO_2 value was achieved and remained constant, the furnace was cooled under continuous gas flow.

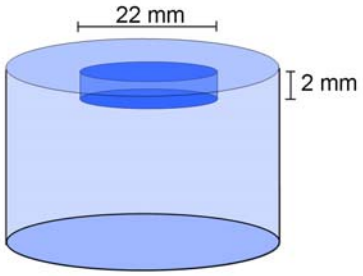

Figure 3.2: Mössbauer sample (dark blue) and bulk material (light blue).

About 20 to 30 mg of the prepared glasses with 0.1, 0.3 and 0.5 wt% SnO_2 in Pt-crucibles were placed into the cold furnace. The samples were tempered in flowing N_2 and in air for 7 d. The heating and the cooling procedures were performed at a rate of 300 K/h. In the case of the Mössbauer samples the surface that was in direct contact with the applied atmosphere is included (see Figure 3.2).

Results and Discussion

Figure 3.3 shows the ^{119}Sn Mössbauer spectra of the glasses with three different tin contents prepared in four different atmospheres. In the right column are the samples with 0.1 wt% SnO_2 in the model glass, in the middle the ones with 0.3 wt% SnO_2 and on the left the glasses with 0.5 wt% SnO_2.

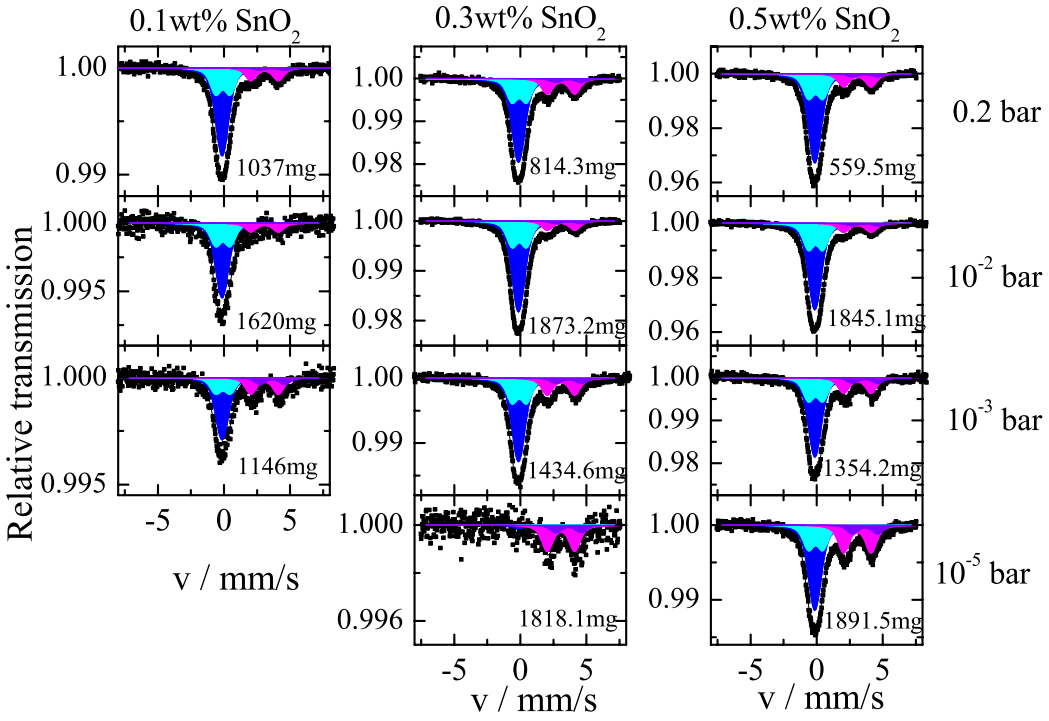

Figure 3.3: ^{119}Sn Mössbauer spectra at 80 K measured in transmission geometry of the samples tempered in atmospheres with varying oxygen partial pressure (1^{st} row: pO_2 = 0.2 bar; 2^{nd} row: $pO_2 = 10^{-2}$ bar 3^{rd} row: $pO_2 = 10^{-3}$ bar and 4^{th} row = 10^{-5} bar). The sample masses are given in the spectra.

In the rows of Figure 3.3 the spectra of the basic material and the heat treated samples are shown. It is clearly visible, that a decrease in the oxygen partial pressure pO_2 during thermal treatment leads to an increase of the Sn^{2+}/Sn^{4+}-ratio. Hence, a reduction of the tin due to the reductive atmosphere takes place. If the melt and the atmosphere are in equilibrium, thermodynamics enables to find the relationship between the oxygen partial pressure and the Sn^{2+}/Sn^{4+} ratio. As the tempering duration was 7 d, it maybe assumed that the equilibrium was reached. The definition of the Gibbs free energy (Equation 1.4) and the definition of the equilibrium constant K (Equation 1.3) of Equation 1.1 are combined to draw a formula connecting oxygen partial pressure and the Sn^{2+}/Sn^{4+} ratio:

$$\frac{[Sn^{2+}]}{[Sn^{4+}]} = exp\left\{\frac{-\Delta H}{RT} + \frac{\Delta S}{R}\right\}\frac{1}{\sqrt{pO_2}} \tag{3.1}$$

So plotting the logarithm of the Sn^{2+}/Sn^{4+} ratio of the measured samples against the logarithm of the oxygen partial pressure during the heat treatment should give a straight line. This is seen in Figure 3.4.

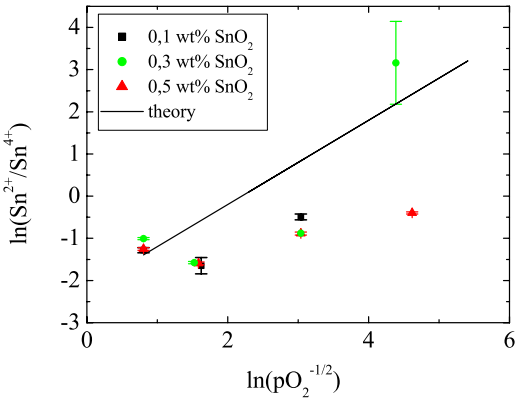

Figure 3.4: Logarithm of the Sn^{2+}/Sn^{4+} ratio against the logarithm of the oxygen partial pressure. The black line represents the theoretical values. The black squares are the measured values of the samples with 0.1 wt% SnO_2 in the starting material, green dots the ones with 0.3 wt% SnO_2 and red triangles with 0.5 wt% SnO_2.

The black line in Figure 3.4 corresponds to Equation 3.1, where the ΔH and ΔS values were known from literature (see Table 9). Measured data was taken from the Mössbauer experiment. The partial subspectra of Sn^{4+} and Sn^{2+} are normalised by the corresponding recoil-free fractions. They are calculated by using Equation 4.2 and the Debye temperatures from Table 4.2. It can be seen that the behaviour of the tempered samples does not follow the theoretical line. This is a consequence of the decrease of the total tin content, which can already be recognised by comparing the relative intensities in the Mössbauer spectra of Figure 3.3. Consequently, reduction occurs in tandem with evaporation during the tempering procedure and the equilibrium of Equation 1.1 can be written as:

$$SnO_2 \rightleftharpoons SnO \uparrow + \frac{1}{2}O_2 \uparrow \tag{3.2}$$

To conclude, it is not possible to describe the data with equilibrium thermodynamics. Additionally, the samples include the surface that was in direct contact to the applied atmosphere. Thus, surface effects caused by the cooling procedure cannot be excluded here.

Table 3.1: First shell Sn-O fitting results of original glass samples.

c(Sn) / wt% SnO_2	r / Å	CN
0.1	2.04	4.23
0.3	2.03	3.48
0.5	2.04	3.84

With EXAFS analysis of the model glasses Sn–O distances r and coordination numbers CN are determined. They are presented in Table 3.1. The obtained Sn–O distances are between 2.03 Å and 2.04 Å, which is very close to the value of crystalline SnO_2 (2.04 Å). That confirms the low Sn^{2+}/Sn^{4+} ratio in the model glasses. The coordination number is about four for all three samples.

3.3 Influences of varying treatment duration in reducing atmospheres on the chemistry of tin in silicate glasses

Sample preparation

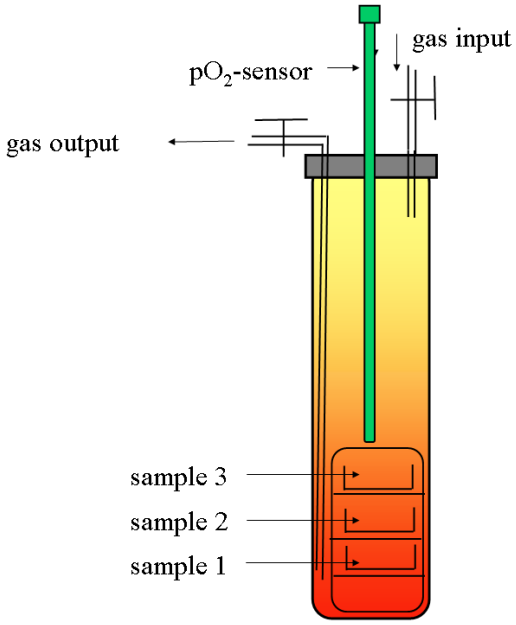

Figure 3.5: Assembly for the experiments with varying thermo treatment duration.

The experiments with varying time were conducted using a Kendro Laboratory Products BL 1801 furnace. To perform the experiments, a special setup as shown in Figure 3.5 was employed. Three Pt-crucibles were filled with 20-30 mg of the prepared glasses and positioned in a sample holder. The crucible containing glass with 0.5 wt% SnO_2 was placed at the lowest position. The one with 0.3 wt% SnO_2 was placed above the first and the one with 0.1 wt% SnO_2 was placed above the second one. The filled sample holder was sunk into a big Al_2O_3 tube which was closed with a flange. The gas inlet and the gas outlet together with the pO_2 sensor based on ZrO_2 passed through the flange. The gas inlet ended directly under the bottom of the flange. Contrarily, the gas outlet ended at the bottom of the big Al_2O_3-tube under the bottom crucible containing glass with 0.5 wt% SnO_2. As a result, the gas was warmed up in the upper region of the tube and the atmosphere was the most homogeneous in the lower part. Two valves, one at the gas flow line and one at the gas return line, and a bubble counter were added to allow for control over the gas flow. Before the experiments in flowing gas mixtures were conducted, the ratio of N_2 / O_2 flow had to be adjusted. For this purpose, the furnace was heated to 1400 ^{o}C without a sample. In the hot furnace the flow of the two gases was adjusted. When the desired pO_2 value was achieved and remained constant,

the furnace was cooled under continuous gas flow. Each set of samples was heated for 1 d, 2 d, 3 d, and 7 d at 1400 ^{o}C. All heating and cooling procedures were performed at a rate of 300 K/h.

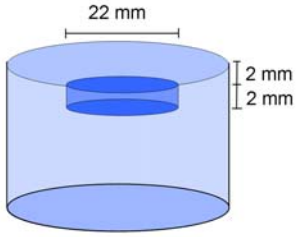

Figure 3.6: Mössbauer sample and bulk material.

The samples from that series are prepared with a depth of 2 mm under the atmosphere side. Consequently, the surface which was in direct contact to the applied atmosphere is not included in the samples (see Figure 3.6).

Results and Discussion

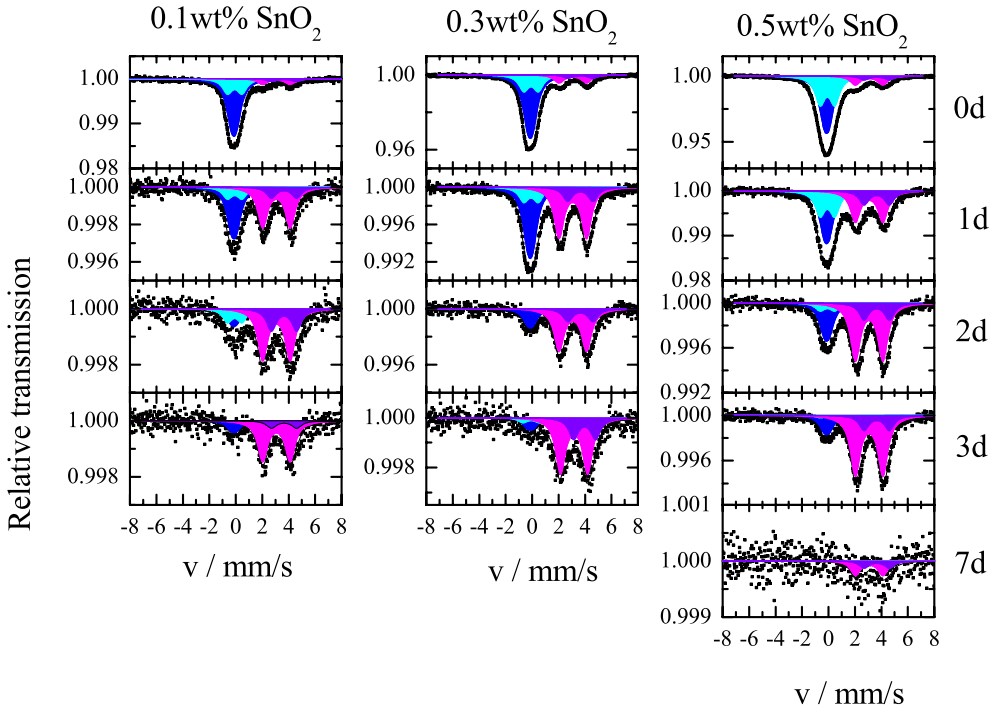

.

Figure 3.7: ^{119}Sn Mössbauer spectra recorded at 80 K in transmission geometry of the samples treated in N_2-atmosphere within 0 d (1^{st} row), 1 d (2^{nd} row), 2 d (3^{rd} row), 3 d (4^{th} row) and 7 d (5^{th} row).

In figure 3.7 the Mössbauer spectra of the samples tempered at 1400^{o}C for 1 d, 2 d 3 d, and 7 d in a N_2-atmosphere are shown. The three basic materials are plotted in columns, the tempering duration is presented in lines. It can already be seen in Figure 3.7, that the total tin content decreases during the heat treatment. A graph displaying the tin concentrations against the treatment duration is shown in Figure 3.8.

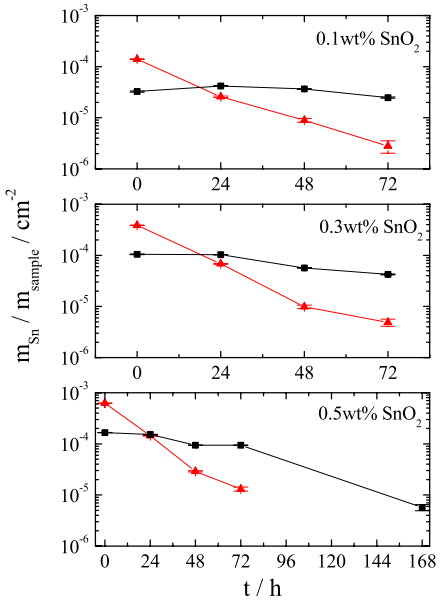

Figure 3.8: Concentration of Sn^{2+} and Sn^{4+} in N_2 treated samples against time of treatment. Black squares and line correspond to Sn^{2+}, red triangles and line correspond to Sn^{4+}.

Sn^{2+} and Sn^{4+} concentrations are corrected as described above. The obtained data was normalised by dividing them by the sample mass. For the samples with 0.1 wt% SnO_2 the Sn^{2+} content increases in the first 24 hours. In all other cases the amount of Sn^{2+} steadily decreases. The Sn^{4+} content decreases for all cases shown in Figure 3.8. The largest loss is always in the first 24 h. After 24 h treatment approximately 50% of the total tin content is evaporated. For glasses with 0.3 and 0.5 wt% SnO_2 the evaporation rate is equal to or lower than the rate of reduction. For the series with 0.1 wt% SnO_2, the Sn^{2+}-concentration increases after 24 h, so the evaporation rate is smaller than the reduction rate. After 24 h it is lower in the 0.1 wt% SnO_2 samples also.

With EXAFS analysis of the glass with 0.5 wt% SnO_2 after different treatment durations Sn–O distances r and coordination numbers CN are determined. They are presented in Table 3.2. The calculated Sn–O distances are between 2.04 Å and 2.09 Å. The distance r increases over the duration of treatment. As r in crystalline SnO

(2.22 Å) is much higher than in crystalline SnO_2 (2.04 Å), that also confirms the increasing Sn^{2+}/Sn^{4+} ratio. Parallel to this the coordination number n decreases with increasing treatment duration. That points on a lower coordination number for Sn^{2+} than for Sn^{4+}.

Table 3.2: First shell Sn-O fitting results of glasses with 0.5 wt% SnO_2 treated for 1 d and 3 d in N_2.

t / d	r / Å	CN
0	2.04	3.84
1	2.06	3.27
3	2.09	2.84

In Figure 3.9 the Mössbauer spectra of the samples tempered at 1400°C for 1 d, 2 d and 3 d in a N_2 / O_2 - atmosphere with a pO_2 of $1 \cdot 10^{-2}$ bar are shown. The two basic materials are plotted in columns and the tempering procedure is presented in lines.

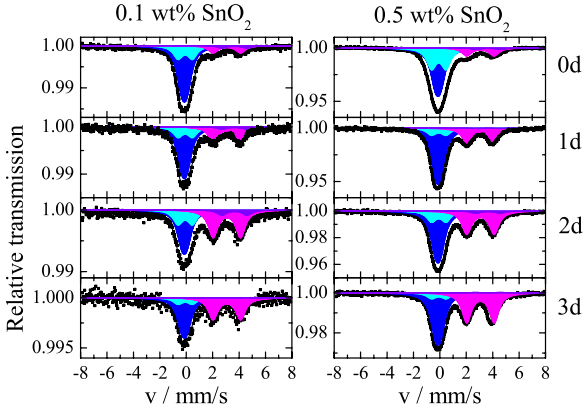

Figure 3.9: ^{119}Sn Mössbauer spectra at 80 K in transmission geometry of the samples treated in an N_2 - O_2 mixture with 10^{-2} bar for 0 d (1^{st} row), 1 d (2^{nd} row), 2 d (3^{rd} row) and 3 d (4^{th} row).

Again with increasing treatment duration the Sn^{2+}/Sn^{4+} ratio increases, but not as pronounced as in the N_2 tempered samples. A graph displaying the tin concentrations against the treatment duration is shown in Figure 3.10.

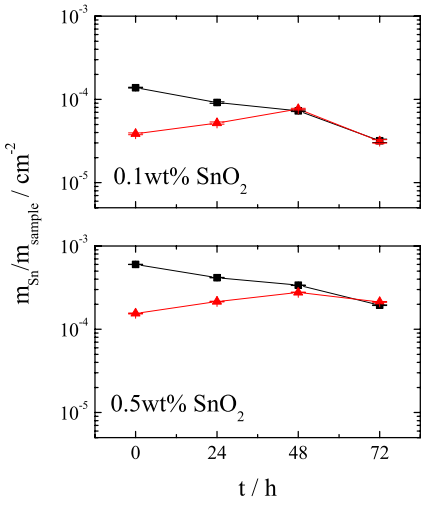

Figure 3.10: Concentration of Sn^{2+} and Sn^{4+} in N_2 - O_2 mixture treated samples against time of treatment. Black squares and line correspond to Sn^{2+}, red triangles and line correspond to Sn^{4+}.

The tin concentrations are obtained as explained above. In both cases the starting material has a Sn^{4+} content that is smaller than the Sn^{2+} content. With longer treatment duration the Sn^{4+} content increases and the Sn^{2+} content decreases. The total loss of tin is much smaller than in the N_2 treated samples. Only above 72 h treatment time about 50% of the total tin is evaporated. The Sn^{2+}/Sn^{4+} ratio for the sample with 0.1 wt% SnO_2 is 0.99 after 72 h of thermal treatment and for the run with 0.5 wt% SnO_2 it is 1.097 $\pm$ 0.006. The theoretical value based on Equation 3.1 is 0.989, very near to the measured data. Consequently the influence of the evaporation of Sn^{2+} affects the Sn^{2+}/Sn^{4+} ratio little less in a reducing atmosphere, if the surface side is excluded from measurements.

3.4 Investigation on the Sn^{2+}/Sn^{4+} ratio in different probing depths after treatment in N_2 atmosphere

Sample preparation

The samples were prepared in the assembly explained in Chapter 3.3. The thermal treatment in N_2 atmosphere was performed for 1 d, 2 d and 3 d. Samples approximately 4 mm in thickness, including the surface region were prepared and transmission Mössbauer spectra were measured.

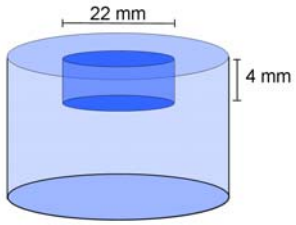

Figure 3.11: Mössbauer sample and bulk material.

After each measurement about 0.5 mm of the samples were removed from the side which was not in contact to the applied atmosphere. Then a further measurement was taken. This procedure was repeated until the sample had a thicknesses of about 0.5 to 1 mm. The sample thicknesses after each polishing step is as presented in Figure 3.12.

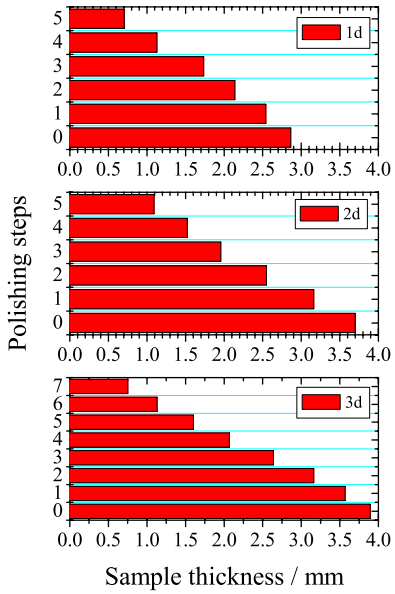

Figure 3.12: Thickness of the samples treated for 1 d, 2 d and 3 d in N_2 atmosphere after each polishing step.

Results and Discussion

After each polishing step the samples were measured in transmission Mössbauer spectroscopy. All spectra are presented in Figure 3.13.

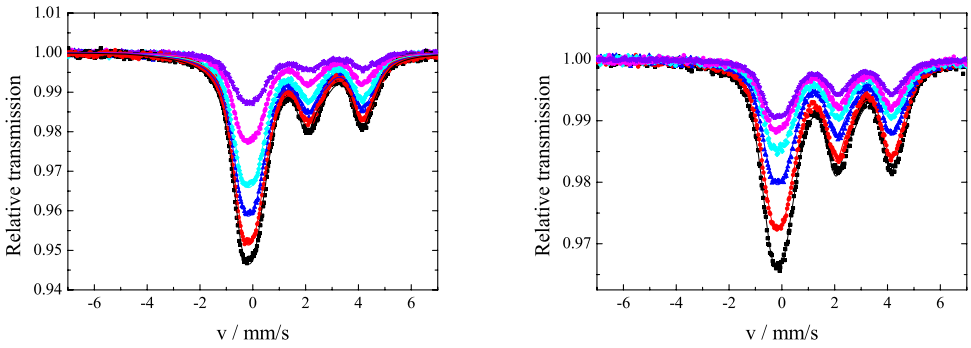

(a) 1 day

(b) 2 days

(c) 3 days

Figure 3.13: ^{119}Sn Mössbauer spectra of the samples treated for 1 d, 2 d and 3 d in N_2 atmosphere and after each polishing step.

The polishing steps always correspond to a removal of about 0.5 mm. It can clearly be seen, that an increase in the treatment duration leads to an overall reduction of the sample. This effect is especially pronounced in the 3 d treated sample. Here the Sn^{2+}/Sn^{4+} ratio increases clearly with increasing number of polishing steps. It can thus be concluded, that the sample has undergone a greater degree of reduction at the surface boundary. The Sn^{2+}/Sn^{4+} ratio is again determined by the Mössbauer results and taking the recoil free fraction into account. In Figure 3.14 this ratio is plotted against the thickness of the samples.

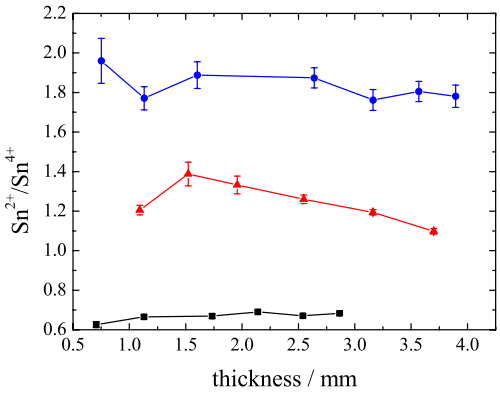

Figure 3.14: Sn^{2+}/Sn^{4+} ratio in samples treated for 1 d (black squares), 2 d (red triangles) and 3 d (blue dots) in N_2 atmosphere.

The 1 d treated sample shows the smallest Sn^{2+}/Sn^{4+} ratio and no change within the studied thickness range. Only below 1.3 mm a small decrease of Sn^{2+} is visible. This is suggestive that surface evaporation of Sn^{2+} is occurring. The Sn^{2+}/Sn^{4+} ratio in the 2 d treated sample steadily increases between 4 mm and 1.5 mm as expected for a N_2 treated sample. When the sample thickness is smaller than 1.5 mm the Sn^{2+}/Sn^{4+} ratio decreases again. That can also be explained by evaporation of Sn^{2+} at the surface. The 3 d treated sample is the most reduced one due to the prolonged exposure to the reductive atmosphere. A small reduction with increasing surface content in the samples is visible. As the total tin content and therewith the effect is smallest here the error of measurement is largest.

3.5 Influences of varying treatment duration in oxygen atmosphere on the chemistry of tin in silicate glasses

Sample preparation

The slow cooled samples were prepared as explained in Chapter 3.3, but the applied gas was always O_2. All heating and cooling rates were 300 K/h. The samples were treated for 1 d, 2 d, 3 d and 7 d.

The fast cooled samples were prepared as follows. About 20 mg of the three glass mixtures were placed in a Pt-crucible. The three samples were placed next to each other in an induction coil (EMA, TPU 100-25-20-1-03). The temperature was measured with a thermocouple. The samples were heated for 1 d, 2 d, and 3 d to 1400 ^{o}C under ambient atmosphere. The heating process was performed with a rate of 300 K/h.

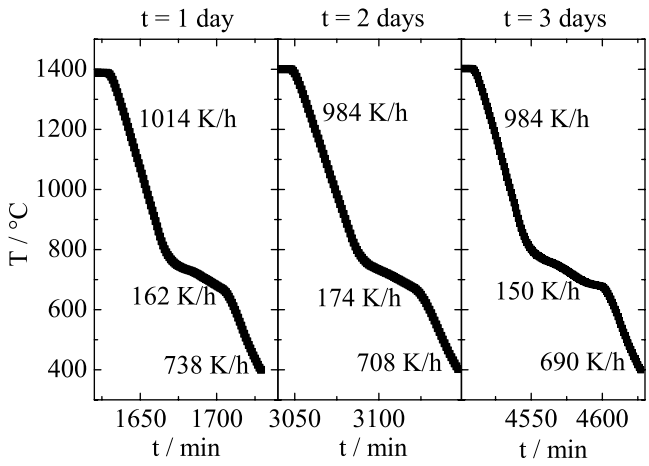

Figure 3.15: Temperatures and cooling rates of the fast cooling processes.

The cooling process was performed in a three-step process. During the first step it was cooled from 1400 ^{o}C to 730 ^{o}C at 1200 K/h, after from 730 ^{o}C to 670 ^{o}C at 180 K/h and finally from 670 ^{o}C to room temperature with 1200 K/h. The measured temperature profiles and the cooling rates were monitored with a thermocouple and are shown in Figure 3.15. The samples from that series were taken from the depth of 2 mm below the side being in contact with atmosphere.

Results and Discussion

In Figure 3.16 the Mössbauer spectra of the samples treated in oxygen atmosphere at 1400 ^{o}C for 1 d, 2 d 3 d, and 7 d with subsequent slow cooling are shown. The spectra of the three basic materials are plotted in columns, the tempering duration is indicated in lines.

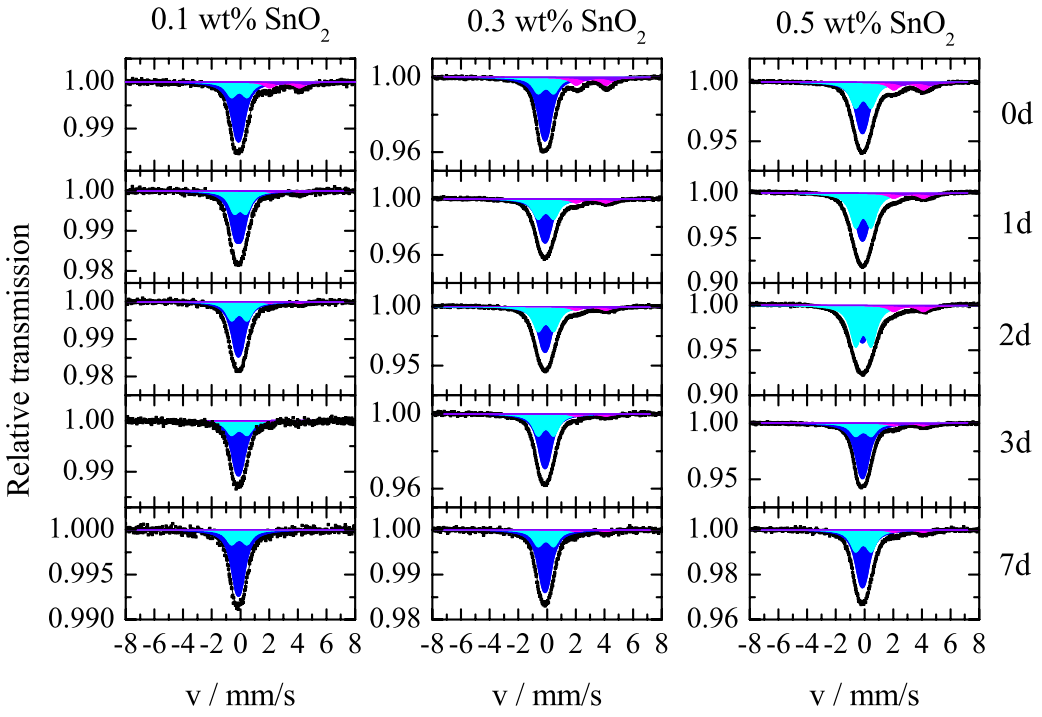

Figure 3.16: ^{119}Sn Mössbauer spectra measured at 80 K in transmission geometry of the samples treated in O_2-atmosphere for 0 d (1^{st} row), 1 d (2^{nd} row), 2 d (3^{rd} row), 3 d (4^{th} row) and 7 d (5^{th} row)

As a consequence of the oxidising atmosphere there is no noticeable change visible in the Sn^{2+}/Sn^{4+}-ratio in all samples visible in the graphs of Figure 3.16. The remarkable thing here is the line broadening of the Sn^{4+} line after 24 h and 48 h of temperature treatment. The samples with 0.5 wt% SnO_2 in the basic material shows the largest broadening. In the fitting procedure this leads to an increase of the relative intensity of the Sn^{4+} line with the larger quadrupole splitting (cyan doublet in Figure 3.16). A graph displaying the tin concentrations against the treatment duration is shown in Figure 3.17.

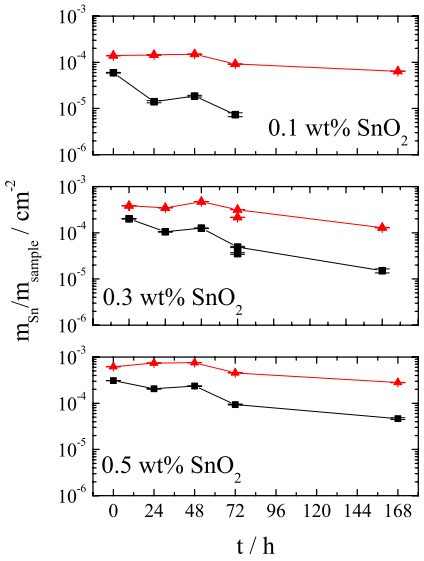

Figure 3.17: Concentration of Sn^{2+} and Sn^{4+} in O_2 treated samples against time of treatment. Black squares and line correspond to Sn^{2+}, red triangles and line correspond to Sn^{4+}.

The progress of the Sn^{2+} and Sn^{4+} curves can only be explained if oxidation and evaporation processes are taken into account. During the first 48 h the Sn^{4+} content increases due to oxidation and the Sn^{2+} content decreases due to evaporation. Concomitantly, the amount of the Sn^{4+} with the asymmetric spectrum increases. Between 48 h and 72 h of treatment the Sn^{2+} and the Sn^{4+} contents decrease, although still an oxidising atmosphere is applied. The amount of the more asymmetric Sn^{4+} component decreases in that time. In the time intervall between 72 h and 168 h the Sn^{2+} and the Sn^{4+} contents decrease while the amount of the more asymmetric Sn^{4+} component stays constant. With XRD analysis no crystalline phase was detected. But as the total tin content in these samples is about 0.5 wt% SnO_2, one could not expect to detect a crystalline SnO_2 phase.

Table 3.3: First shell Sn-O fitting results of glasses with 0.5 wt% SnO_2 treated for 1 d, 2 d and 3 d in O_2.

t / d	r / Å	CN
0	2.04	3.84
1	2.01	4.01
2	2.02	3.86
3	2.05	3.79

The EXAFS results of samples containing 0.5 wt% SnO_2 treated in O_2 atmosphere for varying duration are presented in Table 3.3. The model glass and the sample treated for 3 d show an Sn–O distance close to crystalline SnO_2. That is in agreement with the low Sn^{2+}/Sn^{4+} ratio in these samples. Additionally it underlines that these samples are alike. The Sn–O distances in the samples treated for 1 d and 2 d, which show the broadening of the Sn^{4+} line are smaller and close to the distance in brannockite (2.01 Å [57]). Here the Sn^{4+} atoms are in an octahedral O environment and the O atoms belong to $[SiO_4]$ tetrahedra.

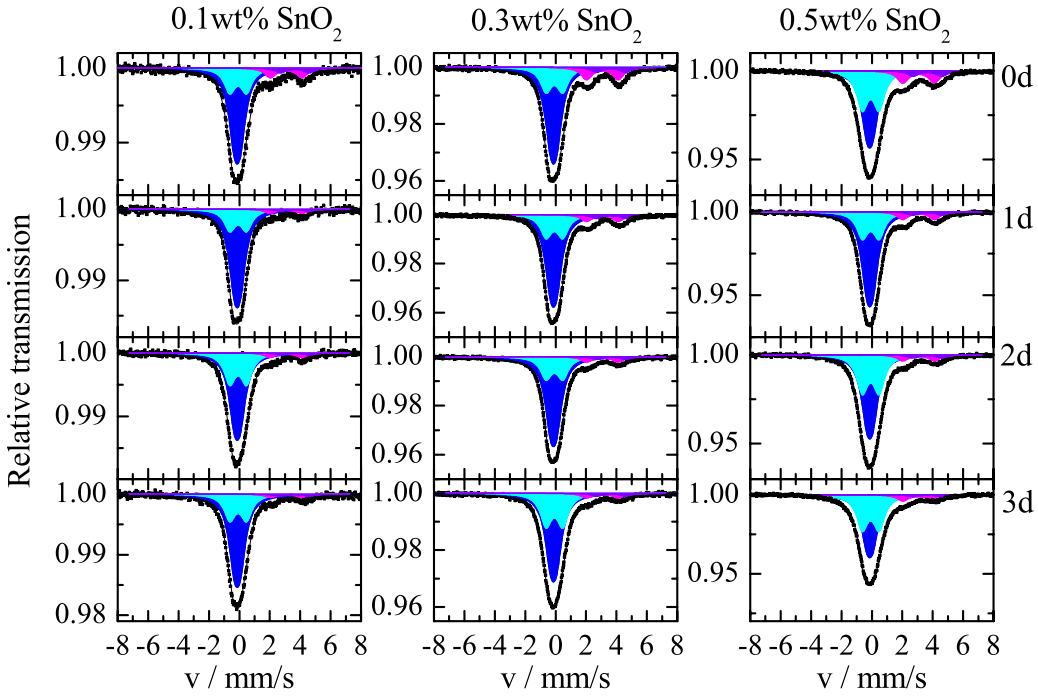

Figure 3.18: ^{119}Sn Mössbauer spectra measured at 80 K in transmission geometry of the samples treated in air for 0 d (1^{st} row), 1 d (2^{nd} row), 2 d (3^{rd} row) and 3 d (4^{th} row) with subsequent fast cooling.

In Figure 3.18 the Mössbauer spectra of the samples treated in air at 1400 ^{o}C for 1 d, 2 d and 3 d with subsequent fast cooling are shown. The three basic materials are plotted in columns, the tempering duration is presented in lines. A broadening of the Sn^{4+} line similar to the observation presented in Figure 3.16 is found here. However, in this experiment the feature is less pronounced. An increase and decrease of the broadening with increasing tempering duration is not visible here. A graph displaying the tin concentrations against the treatment duration in shown in Figure 3.19.

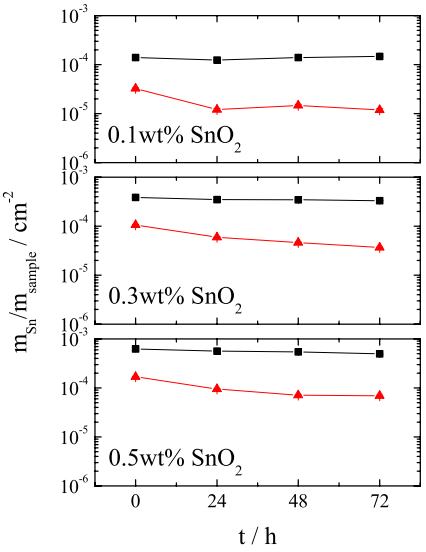

Figure 3.19: Concentration of Sn^{2+} and Sn^{4+} in air treated fast cooled samples against treatment duration. Black squares and line correspond to Sn^{2+}, red triangles and line correspond to Sn^{4+}.

In the samples with 0.3 wt% SnO_2 and 0.5 wt% SnO_2 the Sn^{2+} and the Sn^{4+} ratio slowly and constantly decreases. That means the samples are not undergoing oxidation despite being exposed to an oxidising atmosphere. In the samples are not containing 0.1 wt% SnO_2 the Sn^{2+} content slowly and constantly decreases, while the Sn^{4+} content stays constant. As a consequence oxidation of these samples occur during the first 72 h of heat treatment.

3.6 Study of the addition of CaO to the model glass

Sample preparation

CaO was added as $CaCO_3$. During the heating process it decomposes to CaO and CO_2 which is lost to the atmosphere.

Three glass mixtures of 50 g each were placed in a Pt-crucible. Afterwards, 5, 10 and 15 wt% $CaCO_3$ were added to every sample mixture. Three crucibles were placed adjacent to each other in a furnace (Ceram Aix). The heating procedure as explained in Chapter 2.1 was repeated. The melt was stirred by the evaporation of the CO_2 bubbles. Therefore, no gas injector was required.

The cooled samples were afterwards ground to coarse-grained powder. A fraction with a particle diameter between one and two millimetres was separated and about 1 g of it was loaded into Mössbauer sample holders.

Results and Discussion

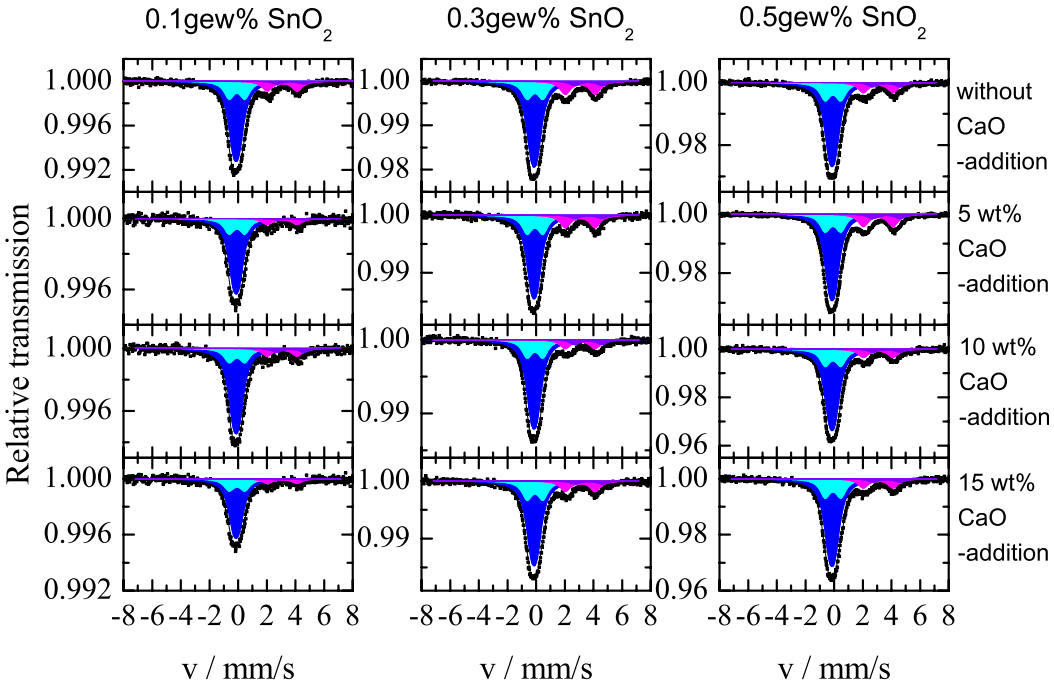

Figure 3.20: ^{119}Sn Mössbauer spectra measured at 80 K in transmission geometry of the samples annealed with CaO addition.

To investigate the influence of Ca^{2+}, samples doped with Ca^{2+} were prepared. If the CaO reacts with the tin in the glass matrix as suggested in Figure 1.9 for Sr^{2+} there

will be a characteristic change in the Mössbauer spectra. Every oxidation state is described with two doublets in the Mössbauer spectra. They correspond to different environments of tin atoms of the same oxidation state. If Sr^{2+} interacts with the tin atoms the local environment will change and a change in the relative intensities of the two Sn^{2+} doublets will be seen. Figure 3.20 shows the ^{119}Sn Mössbauer spectra.

The fraction of the $Sn^{2+}(1)$ species normalised by the total Sn^{2+} amount and the fraction of the $Sn^{4+}(1)$ species normalized by the total Sn^{4+} amount the is plotted against the CaO addition in wt% in Figure 3.21. The fractions of the Sn species are obtained from the Mössbauer analysis. Hyperfine parameter for the four tin species can be found in Table 4.1.

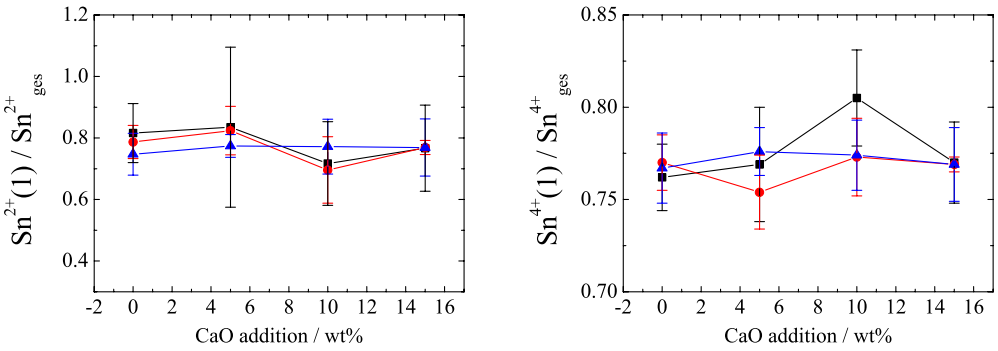

(a) (b)

Figure 3.21: The above graph details the mass of the $Sn^{2+}(1)$ divided by the total Sn^{2+} mass (a) and the mass of the $Sn^{4+}(1)$ divided by the total Sn^{4+} mass (b) against the CaO addition in wt%. The blue triangles correspond to the samples with 0.5 wt% SnO_2 after preparation, the red dots correspond to the samples with 0.3 wt% SnO_2 and the black squares to the samples with 0.1 wt% SnO_2.

There is no trend visible for both valence states and so the reaction as presumed in Figure 1.9 does not run analogously as with Ca. In conclusion, the difference between the two species of one oxidation state is not caused by a coordination to Ca^{2+} of one of them.

3.7 Summary

Thermal treatment in reducing atmospheres leads to a reduction of Sn^{4+} to Sn^{2+} in the samples. That means the pO_2 of the applied atmosphere influences the pO_2 of the glass. But they are not equivalent after treatment for 7 d and thus the Sn^{2+}/Sn^{4+} ratio does not correspond to the applied pO_2. The difference in the Sn^{2+}/Sn^{4+} ratio is associated with evaporation phenomena during thermal treatment. This is noticeable as the atmosphere side is included in these samples. Additionally influences caused by the cooling process may amplify the shift of the Sn^{2+}/Sn^{4+} ratio in the samples of Chapter 3.2. EXAFS analysis of the model glasses gives Sn–O distances similar to the ones of crystalline SnO_2.

In N_2 atmosphere a large evaporation effect appears simultaneously to the reduction of the sample and about 50 % of the total tin evaporates in the first 24 h. In less reducing atmospheres the evaporation rate is much smaller. It takes about 72 h until about 50 % of the tin is evaporated. The Sn^{2+}/Sn^{4+} ratio after 72 h of thermal treatment in an atmosphere with a pO_2 of $1 \cdot 10^{-2}$ bar is very close to the theoretical value in equilibrium. Additionally due to the preparation procedure of the samples, the role of the surface is excluded. Due to the higher Sn^{2+}/Sn^{4+} ratio a longer Sn–O bond is found in the reduced samples with EXAFS. It has been also found that the coordination number decreases with increasing Sn^{2+} content.

Depth profiles of samples treated for 1 d, 2 d and 3 d were measured using ^{119}Sn Mössbauer spectroscopy. An increase of the Sn^{2+}/Sn^{4+} ratio with decreasing sample thickness is detected for the 2 d and the 3 d treated samples. For thicknesses smaller than 1.5 mm a decrease of the Sn^{2+}/Sn^{4+} ratio probably due to evaporation of Sn^{2+} is detected for the shortly treated samples.

The cooling process plays an important role for the samples treated in oxidising atmospheres. A cooling rate of 300 K/h causes a broadening of the Sn^{4+} line in the samples treated for 2 d and 3 d. This effect is directly proportional to the total tin content. The Sn–O distance in these samples is about 2.01 Å, what is close to the value characteristic for brannockite. In the fast cooled samples these effects are not observable. A decrease in the total tin content is seen due to the treatment.

To study the influences of Ca^{2+} on the local environment of the Sn atoms the model glass is prepared with varying Ca^{2+} contents. A change in the relative intensities of the four tin species is not detected. Presumably, the influence of Ca^{2+} is not equivalent to the effect of Sr^{2+} and a reaction as predicted for Sr^{2+} can not be confirmed here.

4 Coordination and bonding of tin in silicate glasses

4.1 Introduction

In the previous chapter hyperfine parameters of tin atoms in many glasses were determined. Additionally, an EXAFS analysis was presented. Here this data is used to formulate an idea of the local environment of the Sn atoms in the glass matrix. Therefore the obtained hyperfine parameters are compared to hyperfine parameter of model systems. Using this data models of the possible Sn environments are postulated. Calculations of the electron density and the electric field gradient at the tin nuclei are used to determine the local surroundings of tin atoms in real glasses.

4.2 Mössbauer spectroscopy

The Mössbauer spectra of all studied samples are shown in Figures 3.3, 3.7, 3.16, 3.18, and 3.20. Sn^{4+} and Sn^{2+} with isomer shifts of about 0 mm/s and 3 mm/s are present in each spectrum. The Mössbauer resonance lines of the Sn^{4+} and Sn^{2+} species are asymmetric. Therefore, the corresponding Mössbauer spectra can not be described with one doublet only. Each asymmetric doublet is presented as a sum of two doublets and these doublets are used to fit every spectrum. For this reason the analysis of the spectrum can be associated with a selected model of the structure. The discrepancies between the spectra are implicated in the analysis through different relative intensities of the four Mössbauer lines. The obtained set of hyperfine parameters is shown in Table 4.1.

Table 4.1: Average hyperfine parameter of all analysed spectra.

	IS/ mm/s	QS/ mm/s
$Sn^{IV}(1)$	-0.140	0.404
$Sn^{IV}(2)$	-0.080	1.097
$Sn^{II}(1)$	3.075	2.079
$Sn^{II}(2)$	3.648	1.910

The two Sn^{4+} subspectra display an isomer shift of about -0.1 mm/s and show a quadrupole splitting of $\approx$ 0.4 mm/s and $\approx$ 1 mm/s, respectively (see Table 4.1). This suggests that there exists one more symmetric and one less symmetric surrounding of the Sn^{4+} atoms. They are close to the hyperfine parameters of SnO_2 (IS = 0 mm/s,

QS = 0.6 mm/s) or $CaSnO_3$ (IS = 0 mm/s, QS = 0 mm/s) where the tin atoms are in an octahedral environment. For the two Sn^{2+} lines both the isomer shift and the quadrupole splitting data are surprisingly large as it is shown in Table 4.1. Only the tin(II) carboxylates show quadrupole splittings of that range. In this compound the tin atom occupies the apex of a distorted trigonal pyramid and one Sn-O-bond is longer than the other two. The same coordination was confermed by neutron scattering experiments [29, 31].

For complete structural analysis the Debye temperatures Θ_D of the four tin species were determined. They are connected with the recoil-free fraction f of Mössbauer nuclei. In the harmonic approximation f is given by:

$$f = exp\left(-\kappa^2 \left\langle x^2 \right\rangle\right) \tag{4.1}$$

where κ is the wavenumber of the resonant γ-ray and $\left\langle x^2 \right\rangle$ is the mean square displacement of the atom from its equilibrium position. In the Debye model f is related to Θ_D and the nuclear recoil energy E_R by the Equation:

$$f = exp\left[\frac{-6E_R}{k\Theta_D}\left\{\frac{1}{4} + \left(\frac{T}{\Theta_D}\right)^2 \int_0^{\Theta_D/T} \frac{x}{e^x - 1} dx\right\}\right] = exp\left[-2W\right]. \tag{4.2}$$

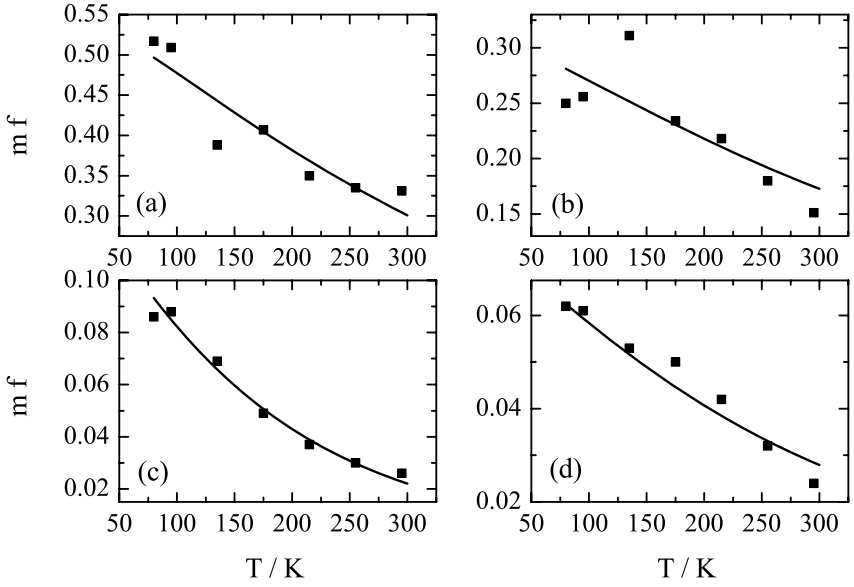

Figure 4.1: The product of the recoil-free fraction and the mass of the absorbing atoms is plotted against the temperature of the measurement. (a) corresponds to [Sn^{4+}(1)], (b) to [Sn^{4+}(2)], (c) to [Sn^{2+}(1)] and (d) to [Sn^{2+}(2)]. The dots show the experimental data, the line gives the theoretical curve following from Equation 4.2.

The product of the recoil-free fraction f and the mass of the absorbing atoms m is the result of the Mössbauer analysis. This value is used for the determination of the Debye temperature following Equation 4.2. A graph displaying this analysis is shown in Figure 4.1 The Debye temperature is a function of the Debye frequency. As this gives a maximum condition of vibration it is a measure of the strength of the atomic binding for equal masses of the surrounding atoms. It may be different for different oxidation states and surroundings. Out of the fitting procedure the mass of the absorbing atom divided by the area of the absorber in mg/cm^2 multiplied by the recoil free fraction is obtained for each included side. Plotting these values as a function of the temperature (see Figure 4.1) and fitting them with Equation 4.2 the Debye temperature and the constant proportional factor are determined. Table 4.2 shows the experimentally determined Debye temperatures.

Table 4.2: Experimental Debye temperatures obtained by the analysis presented in Figure 4.1.

	Θ_D / K
$Sn^{4+}(1)$	270
$Sn^{4+}(2)$	274
$Sn^{2+}(1)$	163
$Sn^{2+}(2)$	216

The values for both Sn^{4+} species are close. That indicates an equivalent bonding strength in the glass matrix. That is not the case for Sn^{2+}. Here the two differing Debye temperatures indicate different bonding strength in the network. In conclusion, one Sn^{2+} site has a bonding and the other a non-bonding character. That means one acts as a network former while the other is more network modifying.

4.3 Theoretical Investigations

Examples of the interpretation of Mössbauer hyperfine parameters based on calculated electron densities and electric field gradients are already known in the literature. These calculations were done with the LMTO software package [58, 59, 60]. Structural data and hyperfine parameters of the well known model materials are measured or taken from literature [61, 62, 60]. The structures of the model materials were geometry optimised using the WIEN2k package [55].

The isomer shift can be expressed as a function of the electron density at the nucleus:

$$IS = \beta\Delta\left\langle r^2\right\rangle\left[\rho_a(0) - \rho_s(0))\right] \tag{4.3}$$

where

$\rho_a(0)$	: electron density at the nuclei of the absorber
$\rho_s(0)$	: electron density at the nuclei of the source
$\Delta\left\langle r^2\right\rangle$	: change in the mean-square radius of the nuclei due to the Mössbauer transition
β	: numerical constant for a given isotope

By plotting the calculated electron densities against the measured isomer shift data a linear correlation should be observed, if the data were obtained with the same source material. The data and the linear fit are plotted in Figure 4.2.

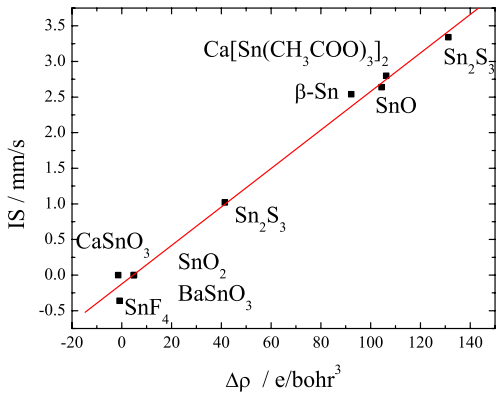

Figure 4.2: The calculated electron densities compared to experimental isomer shifts relative to $CaSnO_3$ (black points). 680180 e/bohr^3 is subtracted from the calculated electron density [61, 62, 60]. A linear fit is plotted in red.

The Mössbauer quadrupole splitting Δ is a result of the interaction between the nuclear quadrupole moment Q and the electric field gradient (EFG):

$$\Delta = \frac{1}{2} eQV_{ZZ} \left(1 + \frac{1}{3}\eta^2\right)^{\frac{1}{2}} \tag{4.4}$$

with

V_{ZZ} : diagonal term of the diagonalised EFG tensor
η : $\frac{V_{XX}-V_{YY}}{V_{ZZ}}$ - asymmetry parameter

where V_{XX} and V_{YY} are diagonal terms of the EFG tensor.

In Figure 4.3 the electric field gradients including the asymmetry parameter correction $\tilde{V}_{ZZ} = |V_{ZZ}| \left(1 + \frac{1}{3}\eta^2\right)^{\frac{1}{2}}$ are compared to experimental quadrupole splittings.

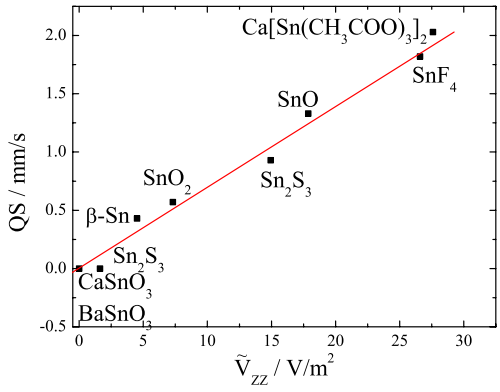

Figure 4.3: The calculated electric field gradients including the asymmetry parameter correction compared to experimental quadrupole splittings (black points) [61, 62, 60]. A linear fit is plotted in red.

A linear dependency is obvious from both graphs and it is possible to determine the quadrupole splitting and the isomer shift of Mössbauer nuclei of calculated substances. For Sn^{4+} a tetrahedral and an octahedral coordination in glasses is presumed. For charge balance in the octahedral case two bonding oxygen atoms which connect two $[SiO_4]$ tetrahedra are inserted in *trans*-position. Consequently, the octahedra around the Sn^{4+} atoms is distorted. For the Sn^{2+} ion, a SnO-like fourfold coordinated structure and a trigonal $[SnO_3]$ pyramid were assumed. The structures are geometry optimised with the Materials Studio 4.1 program package and are shown in Figure 4.4.

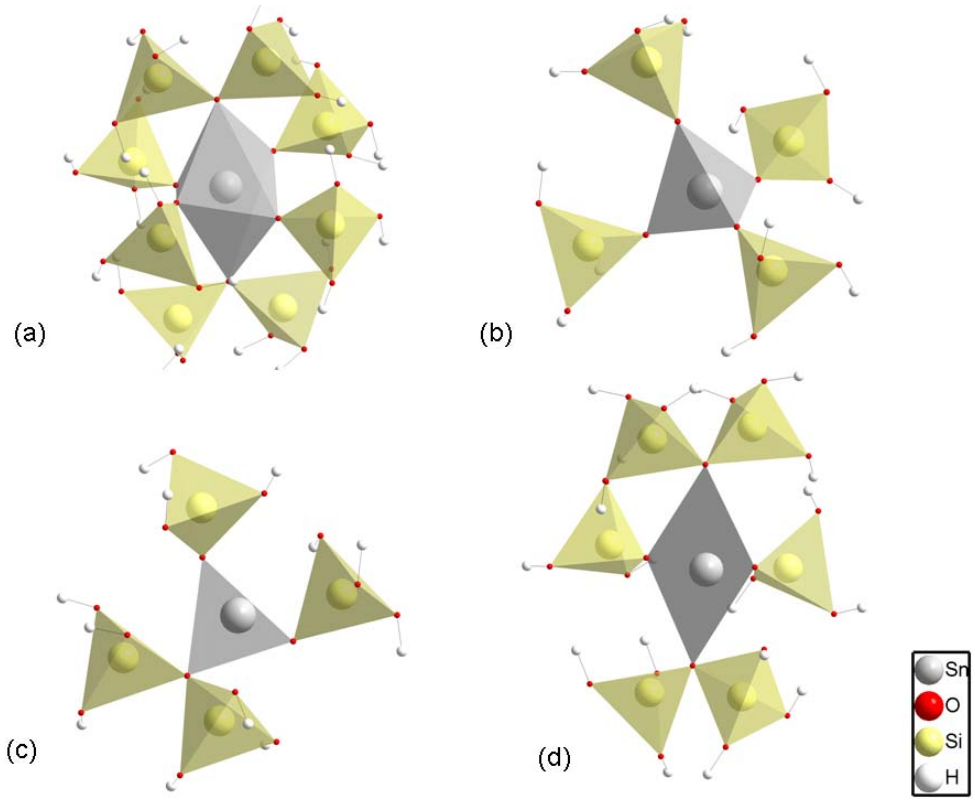

Figure 4.4: Proposed coordination polyhedra: (a) sixfold coordinated Sn^{4+}; (b) fourfold coordinated Sn^{4+}; (c) threefold coordinated Sn^{2+} and (d) fourfold coordinated Sn^{2+}

The octahedral Sn^{4+} coordination (Figure 4.4 (a)) and the fourfold coordinated Sn^{2+} environment (Figure 4.4 (d)) became extremely distorted during the geometry optimisation. The structures (b) and (c) from Figure 4.4 remained conserved in their initial environment.

The calculated hyperfine parameters of tin atoms for the four Sn polyhedra are shown in Table 4.3.

Table 4.3: Calculated hyperfine parameters of tin atoms of the four presumed model polyhedra shown in Figure 4.4.

	IS/ mm/s	QS/ mm/s
$Sn^{IV}O_6$ (a)	-0.17	2.70
$Sn^{IV}O_4$ (b)	-0.29	0.30
$Sn^{II}O_3$ (c)	2.39	1.80
$Sn^{II}O_4$ (d)	2.85	3.19

The distortion in structures (a) and (d) causes a very high quadrupole splitting. The quadrupole splittings of environments (b) and (c) are in the same range as the

experimental ones (see Table 4.1). The isomer shift of structure (a)(see Figure 4.4 and Table 4.3) is about 0.3 mm/s smaller than the isomer shift for the experimental [Sn^{IV}(1)] (see Table 4.1) environment. The shift of structure (c) (see Figure 4.4 and Table 4.3) is about 0.6 mm/s smaller than the experimental shift for the [Sn^{II}(1)] environment in Table 4.1.

4.4 Summary

Sn^{2+}

The trigonal [SnO_3] pyramid is the only coordination that causes a quadrupole splitting of about 2 mm/s. The theoretical investigations also agreed with these results. It was shown that the addition of Ca^+ ions has no influence on the coordination of the Sn^{2+} ions (see Figure 3.21). Consequently, the differences between the two Sn^{2+} coordinations have to be due to coordinations to other elements. As can be seen in Figure 2.1 that can only be Al or B. In Figure 4.5 the two possible coordinations are shown.

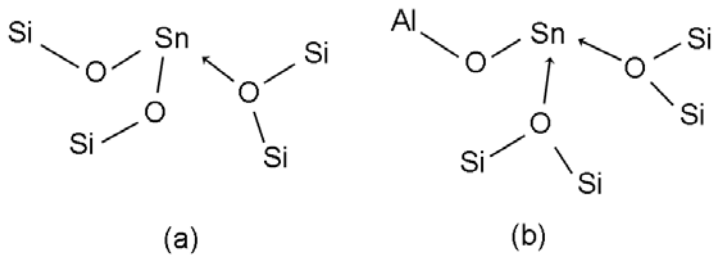

Figure 4.5: Shown are the presumed coordinations for Sn^{2+} ions.

As can be seen, the two polyhedra have different numbers of bonding and non-bonding oxygen atoms. In configuration (a) two O atoms are bonding and connect a Si atom and a Sn atom, and act to balance the charge of the Sn^{2+} atoms. The third O atom is bound to two Si tetrahedra and thus balancing the charge. It acts as a non-bonding oxygen. In the Figure 4.5 (b) two of the three O atoms are non-bonding and only the O connecting the Sn and the Al polyhedron is bonding. This is due to the different number of valence electrons of Al and Si. The smaller number of bonding O atoms makes the Sn atom in configuration (b) more mobile, this also presumes the different Debye temperatures of configuration (a) and (b).

Sn^{4+}

The most probable coordination case for the symmetric Sn^{4+} environment is the four-fold coordinated. A coordination number of about four is confirmed by EXAFS analysis

and only the fourfold coordinated case results in probable theoretical hyperfine parameters. Treatment in oxidising atmospheres with a subsequent slow cooling process caused a broadening of the Sn^{4+} Mössbauer resonance line. That resulted in a high relative fraction of the asymmetric Sn^{4+} environment. With EXAFS analysis Sn–O distances equivalent to values found in the mineral Brannockite were determined. Consequently, the asymmetric Sn^{4+} environment probably corresponds to a sixfold coordination.

5 Diffusion and reaction model

5.1 Introduction

Glass melts can dissolve Sn and O, whereas their equilibrium concentrations are defined by the composition of the melt, the temperature and the activities of Sn and O. Changes of the tin and oxygen content in the glasses at constant temperature T and pressure p are caused by changes of the Sn and O_2 activities at the interfaces. For oxygen these boundary conditions are described by changes of the oxygen partial pressure pO_2 of the neighboring phase. The chemistry of tin can be specified by the activity of liquid Sn, the activity of a solid phase such as Cassiterit or the partial pressure of SnO(g). Inside the melt the changes of the Sn and O chemistry are determined by diffusive transport phenomena. They are described by the according transport equations. The aim of the chapter is to express independent fluxes and forces and afterwards to connect them with the transport coefficients and the measurable microscopic properties of the chemical species. Therefore the linear transport theory of the non-equilibrium thermodynamics [63, 64] is used.

Mössbauer spectroscopy makes a determination of the relative, oxidation state specific concentration of tin in silicate glasses possible. In Chapter 3 the experiments are introduced and the relative concentrations after thermal treatment are determined. These values will be used in this paragraph to create a reaction-diffusion model and finally to calculate diffusion coefficients for the Sn^{2+} and the Sn^{4+} atoms.

5.2 Theoretical background

Balance equation and independent quantities

In the aforementioned experiments concentration profiles and the loss of the Sn species for different diffusion times are determined. It was not possible to describe this type of diffusion phenomena with the classical approaches [65]. A reason for that is that the specific chemical interactions are not taken into account here. For the simulations initial and boundary conditions, correct fluxes and corresponding diffusion coefficients need to be defined. Therefore first the number of independent parameters is determined as it causes the number of minimal necessary fluxes and balance equations. The entropy-production σ combines the fluxes J and the forces X of the independent components k (see Equation 5.1). Glasses are build of an immobile network former and a mobile network modifier. So in addition to Sn and O_2 an oxide $MO_{q/2}$ as the third component and a network oxide $RO_{z/2}$ as a fourth are needed as a minimal set of compounds for

a complete description.

$$\sigma \cdot T = \sum_k J_k \cdot X_k \qquad k = 1..4 \tag{5.1}$$

with the components k: k = Sn, O_2, $MO_{q/2}$, $RO_{z/2}$
The component fluxes are a function of the concentrations c_k:

$$_\omega J_k = c_k \cdot (v_k - \omega_{ref}) \qquad k = 1..4$$

with ω_{ref} as the velocity of the frame of reference.
Therewith the entropy-production becomes:

$$\sigma \cdot T = \sum_k J_k \cdot X_k \qquad k = 1..3$$

In the linear region the fluxes and the forces are connected:

$$J_k = \sum_j L_{kj} X_j \qquad k, j = 1..3$$

and L_{kj} are the transport coefficients. With the Onsager relation $L_{kj} = L_{jk} = 0$ for k $\neq$ j cross-effects are neglected and the fluxes become:

$$J_k = L_k X_k$$

With the phenomenological diffusion coefficients $D_k = L_k \cdot RT/c_k$ the forces $X_k = -\nabla\mu_k = -RT/c_k \cdot \sum_j \mu_{kj} \cdot \nabla c_j$ and the thermodynamic factors $\mu_{kj} = \frac{\partial \mu_k}{\partial c_j}|_{c_{l\neq j}}$ with $\mu_{kM} = \mu_{Mk} = 0$
the diffusion equation can be simplified:

$$J_k = -\sum_j D_{kj} \cdot \mu_{kj} \cdot \nabla c_j = -\tilde{D}_{kk} \cdot \nabla c_k - \tilde{D}_{kl} \cdot \nabla c_l \tag{5.2}$$

The $\tilde{D}_{kl}$ are the chemical diffusion coefficients. The Onsager relation for the L_{jk} can not automatically be applied to the D-matrix. That means the approximation $L_{kj} = 0$ does not necessarily cause a diagonalisation of the D-matrix.

Integration reactions and elementary diffusion phenomena

For understanding the reaction mechanism more precisely a microscopic picture of the melt is needed. There is at least one network builder (= R–O_n) and one network modifier (= $MO_{q/2}$). The cations (R) are immobile ($D_R \approx 0$). The O atoms can be bonding (BO), non-bonding (NBO) or free (O^{2-}) and are existent in a chemical equilibrium.

$$BO + O^{2-} \leftrightarrows 2NBO$$

The bonding oxygen atoms are also immobile ($D_{BO} \approx 0$). That means for the corresponding transport coefficients:

$$L_{O-ion} = L_{BO} + L_{NBO} + L_{O^{2-}} \approx L_{NBO} + L_{O^{2-}}$$

With the assumption that $c_{NBO} \gg c_{O^{2-}}$ the diffusion coefficient can be written as:

$$D_{O-ion} = \frac{RT}{c_{O^{2-}} + c_{NBO}} \cdot (L_{NBO} + L_{O^{2-}}) \approx D_{NBO} + \frac{c_{O^{2-}}}{c_{NBO}} D_{O^{2-}} \tag{5.3}$$

In a ternary system the two independent fluxes and forces need to be defined. The system is simplified by neglecting the mobility of the O anions. The left mobile elements are Sn^{2+}, Sn^{4+} and M^{q+} and the electronic elements. A transport via interstices of the network is assumed to be dominating. The four flux equations are:

$$j_i = -\sum L_{ij} \nabla \eta_j \qquad\qquad i = Sn_K^{4+}, Sn_K^{2+}, M^{q+}, h$$

All correlation effects are neglected ($L_{ij} = \delta_{ij} \cdot L_i$) and the potential gradients of the four electrochemical potentials are given as:

$$\nabla \eta_i = \nabla \mu_i + z_i F \nabla \phi$$

where $\nabla \mu_i$ are the chemical potential gradients and $\nabla \phi$ is the electrical potential gradient. The condition of electroneutrality eliminates the electrical potential gradient $\nabla \phi$. The four fluxes are rather involved. The chemical potentials of the charged species can be summed up so that only three forces ($\nabla \mu_{SnO}, \nabla \mu_{M_qO}, \nabla \mu_O$) are left. They are connected via the Gibbs-Duhem-relation:

$$0 = c_{SnO} \nabla \mu_{SnO} + c_{M_qO} \nabla \mu_{M_qO} + c_O \nabla \mu_O$$

The gradient of the network component ($\nabla \mu_{RO_2}$) is neglected because it is abound and the force $\nabla \mu_{M_qO}$ is eliminated. Then the fluxes are obtained as a function of the components SnO and O, which are essential for the experiment. The remaining three fluxes can be summed up to:

$$J_{Sn} = j_{Sn^{2+}} + j_{Sn^{4+}} = j_{Sn_K^{2+}} + j_{Sn_K^{4+}} + \frac{1}{2} j_h$$

The two remaining independent forces are replaced by adequate concentration gradients. The transformation:

$$\begin{aligned}\nabla\mu_{SnO} &= \mu_{SnO,SnO}\nabla c_{SnO} + \mu_{SnO,O}\nabla c_O \\ \nabla\mu_O &= \mu_{O,SnO}\nabla c_{SnO} + \mu_{O,O}\nabla c_O\end{aligned}$$

leads with the thermodynamic factors $\mu_{ij} = d\mu_i/dc_j$:

$$\mu_{SnO,SnO} = \frac{RT}{c_{SnO}}; \quad \mu_{SnO,O} = 0; \quad \mu_{O,SnO} = -\frac{RT}{c_{SnO}}; \quad \mu_{O,O} = \frac{RT}{c_{SnO_2}}$$

to the diffusion coefficients of the ternary diffusion problem:

$$\begin{aligned}
D_{SnO,SnO} &= 2\frac{D_{Sn_K^{2+}}(2D_{M^{q+}}c_{Sn_K^{2+}} + 8D_{Sn_K^{4+}}c_{Sn_K^{4+}} + 2D_{M^{q+}}c_{M^{q+}} + L_h)}{4D_{Sn_K^{2+}}c_{Sn_K^{2+}} + 16D_{Sn_K^{4+}}c_{Sn_K^{4+}} + 4D_{M^{q+}}c_{M^{q+}} + L_h} \\
D_{SnO,O} &= -\frac{D_{Sn_K^{2+}}c_{Sn_K^{2+}}(-4D_{M^{q+}}c_{Sn_K^{4+}} + 8D_{Sn_K^{4+}}c_{Sn_K^{4+}} + L_h)}{(4D_{Sn_K^{2+}}c_{Sn_K^{2+}} + 16D_{Sn_K^{4+}}c_{Sn^{4+}} + 4D_{M^{q+}}c_{M^{q+}} + L_h)c_{Sn_K^{4+}}} \\
D_{O,SnO} &= -\frac{-8D_{Sn_K^{4+}}c_{Sn_K^{4+}}D_{M^{q+}}c_{Sn_K^{2+}} + 8D_{Sn_K^{2+}}c_{Sn_K^{2+}}D_{Sn_K^{4+}}c_{Sn_K^{4+}}}{(4D_{Sn_K^{2+}}c_{Sn_K^{2+}} + 16D_{Sn_K^{4+}}c_{Sn_K^{4+}} + 4D_{M^{q+}}c_{M^{q+}} + L_h)c_{Sn_K^{2+}}} + \\
&\quad \frac{+2D_{Sn_K^{4+}}c_{Sn_K^{4+}}L_h - L_hD_{M^{q+}}c_{Sn_K^{4+}} + 2D_{Sn_K^{2+}}c_{Sn_K^{2+}}L_h + D_{M^{q+}}c_{M^{q+}}L_h}{(4D_{Sn_K^{2+}}c_{Sn_K^{2+}} + 16D_{Sn_K^{4+}}c_{Sn_K^{4+}} + 4D_{M^{q+}}c_{M^{q+}} + L_h)c_{Sn_K^{2+}}} \\
D_{O,O} &= \frac{8D_{Sn_K^{4+}}c^2_{Sn_K^{4+}}D_{M^{q+}} + 4D_{Sn_K^{2+}}c_{Sn_K^{2+}}D_{Sn_K^{4+}}c_{Sn_K^{4+}} + 4D_{Sn_K^{4+}}c_{Sn_K^{4+}}D_{M^{q+}}c_{M^{q+}}}{(4D_{Sn_K^{2+}}c_{Sn_K^{2+}} + 16D_{Sn_K^{4+}}c_{Sn_K^{4+}} + 4D_{M^{q+}}c_{M^{q+}} + L_h)c_{Sn_K^{4+}}} \cdot \\
&\quad \frac{+D_{Sn_K^{4+}}c_{Sn_K^{4+}}L_h + L_hD_{M^{q+}}c_{Sn_K^{4+}} + D_{Sn_K^{2+}}c_{Sn_K^{2+}}L_h + D_{M^{q+}}c_{M^{q+}}}{(4D_{Sn_K^{2+}}c_{Sn_K^{2+}} + 16D_{Sn_K^{4+}}c_{Sn_K^{4+}} + 4D_{M^{q+}}c_{M^{q+}} + L_h)c_{Sn_K^{4+}}}
\end{aligned} \tag{5.4}$$

For the used model glass it can be said that $c_{M^{q+}} = c_M(\approx 15\ \text{mol\%}) \gg c_{Sn}(\approx 0.2\ \text{mol\%}) = c_{Sn^{2+}} + c_{Sn^{4+}}$. Therewith the complex equations become simplified with assuming $L_{M^{q+}} \gg L_{Sn^{2+}} + L_{Sn^{4+}} * L_h$.

$$
\begin{aligned}
D_{SnO,SnO} &= \frac{(c_{Sn^{2+}} + c_{M^{q+}})D_{Sn^{2+}}}{c_{M^{q+}}} \approx D_{Sn^{2+}} \\
D_{SnO,O} &= \frac{D_{Sn^{2+}} c_{Sn^{2+}}}{c_{M^{q+}}} < D_{Sn^{2+}}/100 \approx 0 \\
D_{O,SnO} &= \frac{1}{4}\frac{(c_{Sn^{2+}} - c_{M^{q+}})L_h}{c_{Sn^{2+}} c_{M^{q+}}} \approx -\frac{1}{4}\frac{L_h \cdot RT}{c_{Sn^{2+}}} = -D_{O,O} \cdot \frac{c_{Sn^{4+}}}{c_{Sn^{2+}}} \\
D_{O,O} &= \frac{1}{4}\frac{(c_{Sn^{4+}} + c_{M^{q+}})L_h}{c_{Sn^{4+}} c_{M^{q+}}} \approx \frac{1}{4}\frac{L_h \cdot RT}{c_{Sn^{4+}}}
\end{aligned} \tag{5.5}
$$

5.3 Numerical simulation of concentration "profiles"

The aforementioned experiments can be described as follows. The initial tin concentration in a homogeneous piece of glass is c^o and splits into the species concentrations c_2^o and c_4^o. They conform to the mass active law:

$$K(T) = \frac{c_2^o}{c_4^o}\sqrt{p_{o2}^o} \tag{5.6}$$

according to the temperature T of the experiment and according to the initially homogeneous p_{o2}^o of the sample. First a one-dimensional geometry is considered. The concentration c_2 and c_4 are functions of the time t and a direction ξ: $c_2(\xi,t)$ and $c_4(\xi,t)$. They conform to the diffusion equations:

$$
\begin{aligned}
\dot{c_2} &= \nabla(\tilde{D}_{22}\nabla c_2 + \tilde{D}_{24}\nabla c_4) \\
\dot{c_4} &= \nabla(\tilde{D}_{42}\nabla c_2 + \tilde{D}_{44}\nabla c_4)
\end{aligned} \tag{5.7}
$$

where the chemical diffusion coefficients $\tilde{D}_{kl}$ are local functions of the species concentrations $c_2(\xi,t)$, $c_4(\xi,t)$ and of a set of microscopic mobilities, only.

In one dimension there are two boundaries, with the following boundary conditions. The system is closed at one point $\xi = \xi_2$:

$$j_2 = 0|_{\xi=\xi_2}; \qquad j_4 = 0|_{\xi=\xi_2} \tag{5.8}$$

This corresponds to the closed crucible. At the atmosphere-glass interface ($\xi = \xi_1$) the atmosphere is determined by an oxygen partial pressure p_{o2}^g. The assumption of an equilibrium condition for the oxygen $p_{o2}^g = p_{o2}(\xi = \xi_1)$ causes a local coupling condition for the tin species:

$$\frac{c_2(\xi = \xi_1)}{c_4(\xi = \xi_1)} = \frac{K(T)}{p^g_{o2}}$$

and the first boundary condition follows as:

$$c_4(\xi = \xi_1) = c_2(\xi = \xi_1)\frac{\sqrt{p^g_{o2}}}{K(T)} \tag{5.9}$$

The second boundary condition should describe the mass transfer of tin from the gas to the atmosphere due to evaporation. According to Langmuir, the evaporation rate basically depends on the vapour pressure of the dissolved species:

$$j_i = \frac{\dot{n}_i}{A} = \frac{p_i(T)}{\sqrt{2\pi M_i RT}}$$

As the vapour pressure of pure SnO ($p^o_{SnO}(1400\ ℃) = 8.3 \cdot 10^{-2}$ bar) is larger than the one for SnO_2 a mass transfer only of SnO can be considered. The activity coefficient γ of the diluted SnO in the glass matrix at 1400 ℃ is 0.41. The mole fraction of SnO in the glass is defined as $x_{SnO} = x_{Sn} \cdot x_2$ with $x^o_{Sn} = 0.2 \cdot 10^{-2}$ mol Sn / mol glass the initial activity a^o_{SnO} is:

$$a^o_{SnO} = \gamma_{SnO} \cdot x^o_{SnO} = \gamma_{SnO} \cdot x^o_{Sn} \cdot x_2 = 0.82 \cdot 10^{-3} \cdot x_2$$

Therewith the vapour pressure:

$$p^o_{SnO}(glass) = p^o_{SnO} \cdot a^o_{SnO} \approx 7 \cdot 10^{-5} bar \cdot x_2$$

and the evaporative flux are set to :

$$j^o_{SnO} = 5.4 \cdot 10^{-2}\ \frac{mol}{m^2 s} \cdot x_2$$

This equation serves as the second boundary condition in the form:

$$j_2|_{\xi=\xi_1} = k_c \cdot c_2 \tag{5.10}$$

With the molar mass (M = 64.53 $\frac{g}{mol}$) and the density (2.456 $\frac{g}{mL}$) k_c is equal to:

$$k_c = 1.4 \cdot 10^{-6}\ \frac{m}{s} \tag{5.11}$$

Fitting material parameter

There are five fitting constants: $\tilde{D}_{22}, \tilde{D}_{24}, \tilde{D}_{42}, \tilde{D}_{44}$ and k_c according to the diffusion equations 5.7 and the boundary conditions 5.8, 5.9 and 5.10. The diffusion model expresses the chemical diffusion coefficients $\tilde{D}_{kl}$ as unique functions of the elementary

mobilities of Sn^{2+} and Sn^{4+} such as f(D_2, D_4). Therefore the number of fitting parameters reduces to three: D_2, D_4 and k_c. The fitting procedure depends on the form of experimental results and the way of extracting information about the distribution of species in time and space. One sort of experiment analysis concentration profiles for given diffusion times. A second type of experiment compares the loss of Sn species in a specified volume for different diffusion times:

$$N_{Sn}(t) = V_{sample} \cdot \int_{\xi_1}^{\xi_2} c_{Sn} d\xi \cdot \frac{1}{\Delta\xi}$$

Both type of data are amenable to numerical simulations. So far the procedure for analysing one-dimensional diffusion experiments have been given. The method can easily be extended to two- or three-dimensional geometries with arbitrary boundary conditions. Details will be explained in the following sections.

5.4 Results and discussion

A one dimensional model was used and the total D-matrix following Equation 5.4 was determined. The model was compared to the Mössbauer data of the samples treated in N_2 atmosphere. The diffusion coefficient for Sn^{2+} and for Sn^{4+} as well as the mass transfer coefficient were varied until good agreement with the measured data was achieved. The determined values for the D - matrix are summarised in Table 5.1.

Table 5.1: D_{ij} data of the one-dimensional problem

	0 d N_2	3 d N_2
D_{22}	$5 \cdot 10^{-7}$ cm^2/s	$5 \cdot 10^{-7}$ cm^2/s
D_{24}	0 cm^2/s	0 cm^2/s
D_{42}	$1 \cdot 10^{-7}$ cm^2/s	$1 \cdot 10^{-11}$ cm^2/s
D_{44}	$5 \cdot 10^{-6}$ cm^2/s	$5 \cdot 10^{-6}$ cm^2/s

D_{24} is always approximately zero and can be neglected. The simplified definition of D_{42} is shown in Equation 5.5. It depends on the ratio of $c_{Sn^{4+}}/c_{Sn^{2+}}$ and is in the same order of magnitude than the diagonal elements for initial conditions . After three days treatment in reducing atmosphere becomes small compared to D_{22} and D_{44}. Taking the whole D-matrix into account did not improve the quality of the fitting results. For this reason both off diagonal elements were neglected. For further improvement of the model a two and a three dimensional geometry with two separated equations for Sn^{2+} and Sn^{4+} were tested. As no relevant differences were detected the two-dimensional problem was used for the analysis of all data sets. For considering a two-dimensional geometry the following scheme of settings is used.

Figure 5.1: Settings of the two dimensional diffusion problem.

The total hight of the glass in the Pt vessels after each experiment was about 1 cm so the total depth of the model is set to 1 cm. The thermal treatment samples were prepared as 2 mm thick discs from a depth of 2 mm. In analogy to this the area between 2 and 4 mm is the domain of diffusion (dark blue area of Figure 5.1). For all glass-vessel boundaries the system is closed (see Equation 5.8). For the glass-atmosphere interface the two boundary conditions following Equations 5.9 and 5.10 are applied.

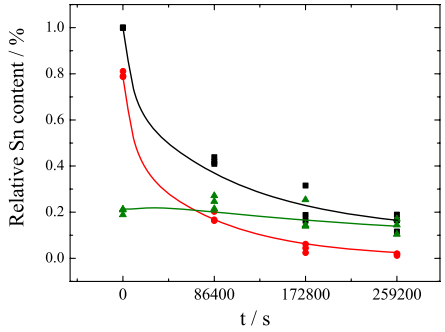

(a) $pO_2 = 10^{-4}$ bar

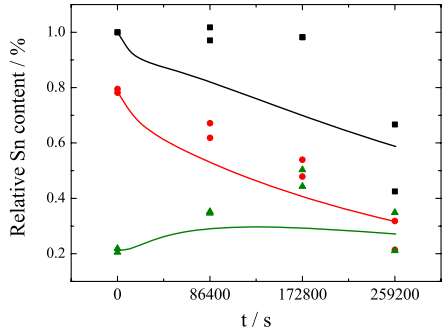

(b) $pO_2 = 10^{-2}$ bar

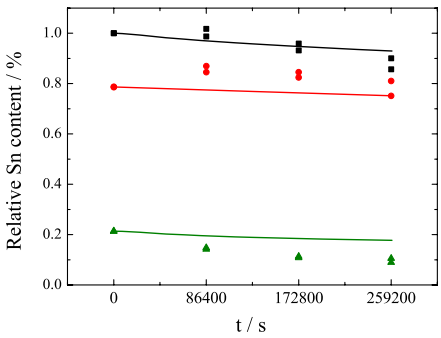

(c) $pO_2 = 0.2$ bar

Figure 5.2: Shown are the experimental data and the simulation of the relative Sn contents of samples treated in different atmospheres against time of thermal treatment. Red colour corresponds to Sn^{4+}, green to Sn^{2+} and black to the total tin content. The samples containing 0.1, 0.3 and 0.5 wt% SnO_2 are presented in the same graph.

For a correct comparison of measured data and simulated data the concentrations need to be defined similarly. Therefore, the total tin concentration in a model glass after preparation is set to 1 and the relative Sn^{2+} and Sn^{4+} contents become ≈ 0.2 and ≈ 0.8. The tin concentrations after 1 d, 2 d and 3 d of thermal treatment are referred to the values before the experiments. Measured data and simulations are presented in Figure 5.2.

The drawn through lines of Figure 5.2 correspond to simulations with diffusion coefficients $D_{Sn^{2+}}$ and $D_{Sn^{4+}}$ of $5 \cdot 10^{-7}$ cm^2/s and $5 \cdot 10^{-6}$ cm^2/s and k_c is set to $5 \cdot 10^{-8}$ m/s.

The time dependend analysis was complemented with a position dependend analysis. Here samples treated for 1 d, 2 d and 3 d in reducing atmosphere were measured with varying sample thicknesses (see Chapter 3.4). A comparison of this data to the model is presented in Figure 5.3.

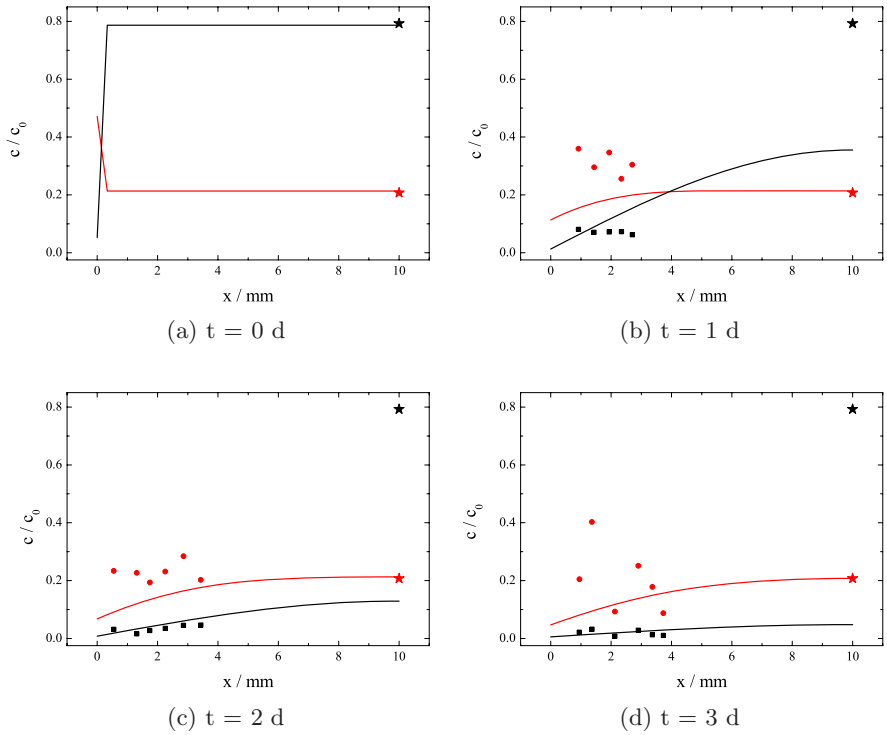

(a) t = 0 d (b) t = 1 d

(c) t = 2 d (d) t = 3 d

Figure 5.3: Experimental data (squares and dots) and the simulations (lines) of the relative Sn contents of samples treated in different atmospheres versus probing depth x. Red colour corresponds to Sn^{2+}, black to Sn^{4+}. The stars represent the data before the experiment. All samples contained 0.5 wt% SnO_2 after preparation.

In Figure 5.3a the initial conditions are shown. For the bulk material the Sn^{2+}/Sn^{4+} ratio is constant and determined by the pO_2 of the glass. At the surface the pO_2 of the employed gas reduces the sample. Figures 5.3b, 5.3c and 5.3d present the depth

dependend data and the model at t = 1 d, 2 d, and 3 d. Therefore, the difference of the Mössbauer relative intensities of two following polishing steps is divided by the difference of the two sample thicknesses and normalised by the original model glass values. This procedure enlarges the inaccuracy of the displayed quantity. Nevertheless, no disagreement between the model and the measured data could be found. It should be noticed, that after 1 d of thermal treatment a large amount of Sn^{4+} is already reduced. At the vessel bottom ($x = 10\ mm$) the Sn^{4+} content is not conform to the original value. That means thermal treatment for a shorter time and a preparation of the sample at a lower position would have better verified or falsified the model.

It is shown that all data could be simulated with the same diffusion coefficients and the same mass transfer coefficient. The values are shown in Table 5.2.

Table 5.2: Fitting results of the diffusion experiments.

D_2	$5 \cdot 10^{-7}$ cm^2/s
D_4	$5 \cdot 10^{-6}$ cm^2/s
k_c	$5 \cdot 10^{-8}$ m/s

The diffusion coefficients are in the expected order of magnitude compared to the literature data (see appendix). As Sn^{4+} has the larger Debye temperature and possesses more bonding oxygen atoms than Sn^{2+} the diffusion coefficient should be smaller than the one for Sn^{2+}. But the resulting diffusion coefficient for Sn^{4+} is larger than the one for Sn^{2+}. One possible explanation is taking electron hopping processes into account. The mass transfer coefficient k_c is smaller than the estimated value following Equation 5.11, but it is still in the same order of magnitude.

A graph displaying the reaction and diffusion processes is presented in figure 5.4. At the atmosphere-glass interface the oxygen partial pressure of the gas determines the Sn^{2+}/Sn^{4+} ratio in the melt. Additionally Sn^{2+} can evaporate as SnO as long as the atmosphere above the melt is not saturated with SnO. In the aforementioned experiments a small gas flow was applied and the evaporation was not inhibited. Inside the glass the Sn^{2+} ions are mobile, but the charge equalisation has to be respected. Therefore a diffusion of Ca^{+} ions in the opposite direction is displayed in the figure. Because of the high diffusion coefficient it can not be assumed that the Sn^{4+} ions move through the melt. Consequently electron hopping processes are used to transfer the charge.

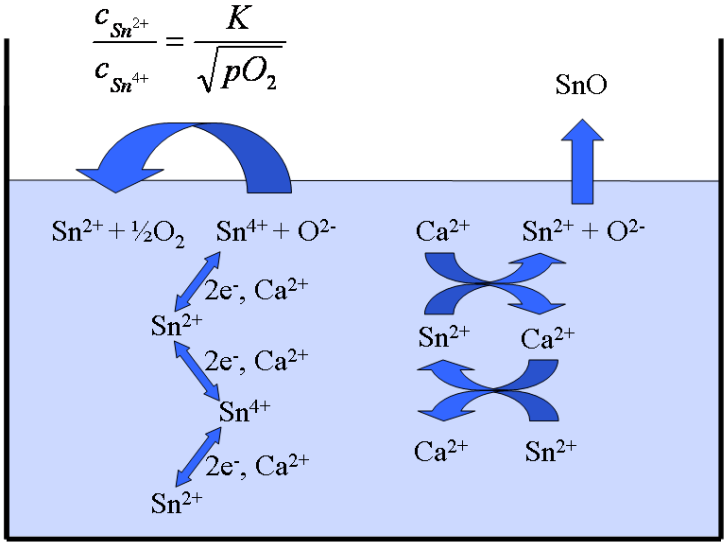

Figure 5.4: Reaction and diffusion model

5.5 Summary

A two-dimensional model with neglected off-diagonal elements of the D-matrix is successfully used to describe the Mössbauer relative intensities. The time and the position dependend measurements after treatment in reducing and oxidising atmospheres are used for this analysis. One set of fitting constants ($D2$, $D4$ and k_c) presented in table 5.2 is obtained. The diffusion coefficients are in the expected order of magnitude in comparison to the data from literature. But the explained procedure made a determination of oxidation state specific diffusion coefficients possible. In contrast to the expectations the presented diffusion coefficient for Sn^{4+} is larger than the one for Sn^{2+}. That can be explained by taking electron hopping processes into account. Then the Sn^{4+} ions can be immobile and the charge only is moving. As the Sn^{2+} ions are more mobile the determined diffusion coefficient can be explained by a movement of Sn^{2+} ions through the melt.

6 Glass and glass ceramics of a Li_2O-Al_2O_3-SiO_2 system

6.1 Introduction

The glass ceramics of the LAS-system (Li_2O - Al_2O_3 - SiO_2) became of a topic of special interest because of their high resistance to temperature differences and low coefficients of thermal expansion ($0.2 \cdot 10^{-6}$ K^{-1} measured from 20 ^oC to 700 ^oC) in the high-quartz solid solution phase [66]. This makes them ideal materials for commercial items such as cooktop panels. With further heat treatment the metastable high-quartz solid solution transforms into a keatit solid solution. These materials are the subject of interest due to their adjustable translucent and opaque appearance and colourability. The lower content of residual glass phase causes a higher fracture strength and the larger crystals (> 300 nm) leads to a translucent appearance. These qualities make the keatit based glass ceramic advantageous against the metastable high-quartz phase. However, the coefficient of thermal expansion increases in the keatit glass ceramics to $1 \cdot 10^{-6}$ K^{-1}, which makes them more susceptible to failure due to thermal shock.

In this work the structural differences of the glasses and glass ceramics of the LAS-system are under investigation. It is shown that ceramisation phenomena can be characterised by ^{119}Sn Mössbauer spectroscopy. The spectra of the glass and the glass ceramic systems are measured in transmission geometry at 80 K.

6.2 Experimental details

A glass with main components 8 mol% Li_2O, 14 mol% Al_2O_3, and 71 mol% Al_2O_3 is transformed to a Keatit solid solution. Therefore a heat treatment procedure is performed in three steps (see Table 6.1).

Table 6.1: Glass and glass ceramic samples and their preparation.

name	substance	treatment procedure
K0	glass	-
K1	after nucleation	30 min at 750 ^oC
K2	metastable high-quartz solid solution	30 min at 750 ^oC + 30 min at 890 ^oC
K3	Keatit solid solution	30 min at 750 ^oC + 30 min at 890 ^oC + 30 min at 1100 ^oC

For nucleation the glass is first heated for 30 min at 750 ^oC. Then it is heated at

890 ^oC for 30 min to build the metastable high-quartz solid solution and after another heat treatment for 30 min at 1100 ^oC the final keatit phase is formed.

The ^{119}Sn Mössbauer spectroscopy of the samples in the form of 2 mm thick discs with a diameter of 22 mm was performed at 80 K in transmission geometry. A $Ca^{119m}SnO_3$ Mössbauer source with resonance energy 23.88 keV was used. A Pd-foil filter with characteristic absorption of 24.35 keV was used to suppress the 25.04 keV radiation [8]. The experiments were performed with a spectrometer with a flow-gas cryostat using liquid N_2. The analysis of the spectra was carried out with the EFFINO software package [46]. Each set of spectra was treated parallel with the same set of hyperfine parameter.

6.3 Results and Discussion

The 80 K transmission Mössbauer spectra are presented in Figure 6.1.

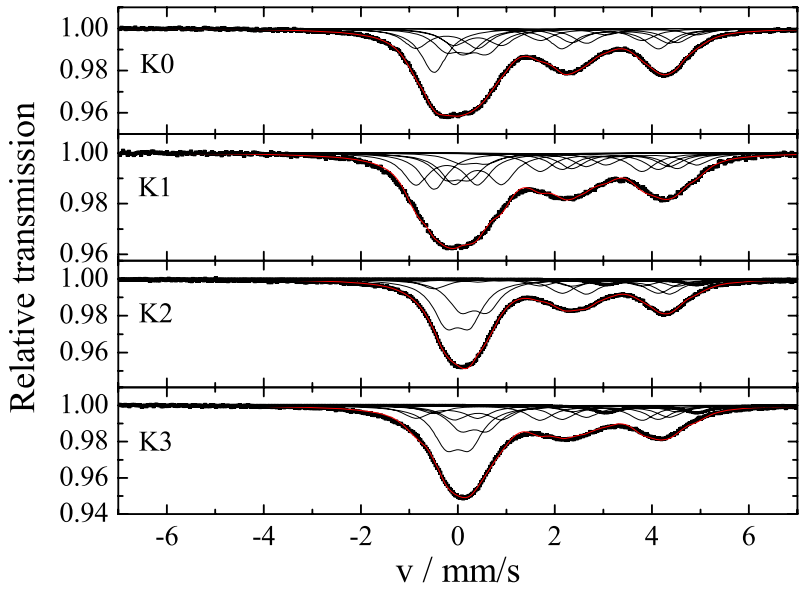

Figure 6.1: ^{119}Sn Mössbauer spectra of Li-containing samples measured at 80 K.

In the basic material the extremely broad lines are remarkable. This is especially pronounced at the Sn^{4+} site at about 0 mm/s. Both the Sn^{2+} and the Sn^{4+} resonance line have an asymmetric shape, which is a clear indication for a distribution of various environments of the Sn^{2+} and Sn^{4+} atoms. The spectrum of the material after nucleation looks similar, while the spectra of the ceramic materials differ from the ones of the basic material. The lines of the ceramic materials are much more narrow, what is especially seen at the Sn^{4+} site. It should be stressed, that the Keatit (K3)

spectrum does not display the most narrow Sn^{4+} line, but the high quartz spectrum (K2). Additionally, the Sn^{2+}/Sn^{4+} ratio decreases with increase of thermal treatment temperature, as can be seen in Figure 6.1. Hence, the tempering procedure leads to an oxidation of the sample.

All spectra were treated simultaneously during the fit. For the analysis a model with five sites at the Sn^{4+} and the Sn^{2+} was used. In other words, five environments for Sn^{4+} and five for Sn^{2+} were presumed. Sn^{4+} atoms are bond to four O atoms to achieve charge balance. As discussed above, a tetrahedral environment for Sn^{4+} is reasonable. The charges of the four O atoms on the tetrahedral edges are also balanced, this maybe achieved by bonding to Si atoms which form SiO_4-tetrahedra. Alternatively, as far as in this material a high number of Li atoms are present, the charge of O atoms can be compensated by bonding to Li atoms. Thus for the four Sn–O–bondings five configurations are possible (see Figure 6.2), they correspond to the five subspectra for Sn^{4+}. Similar for the Sn^{2+} also five different surroundings are presumed. If the Sn^{2+} is on top of a trigonal pyramid of three O atoms and one Sn atom, two O atoms need to be bonded to the Sn and one non-bonding, due to the charge equalisation. That makes four Sn-O-X-bondings and five clusters, which are shown in Figure 6.3.

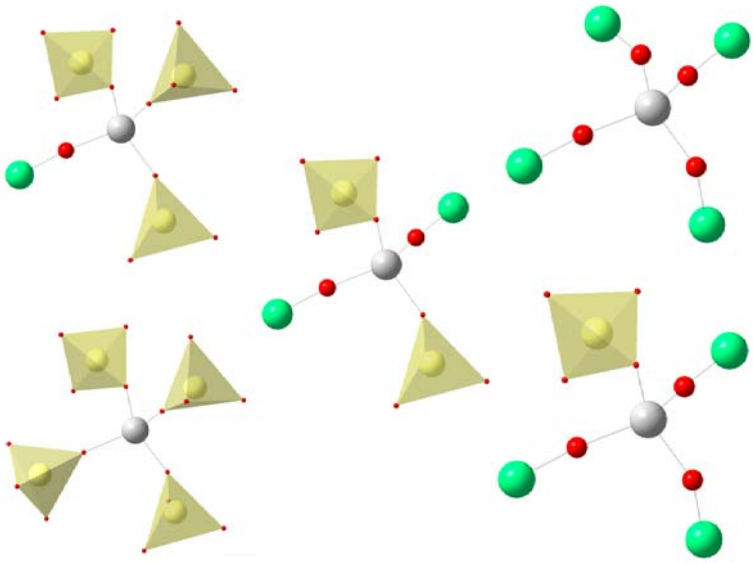

Figure 6.2: Possible configurations of Sn^{4+} environments. Grey balls correspond to Sn, red to O, yellow to Si and green to Ca.

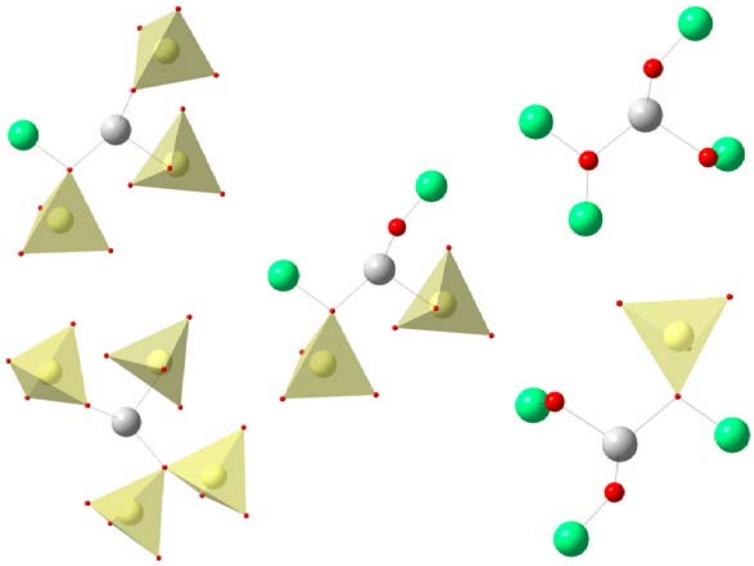

Figure 6.3: Possible configurations of Sn^{2+} environments. Grey balls correspond to Sn, red to O, yellow to Si and green to Ca.

The relative intensities of the ten lines are presented in Figure 6.4. The first five lines belong to Sn^{4+}, while the last five belong to Sn^{2+}.

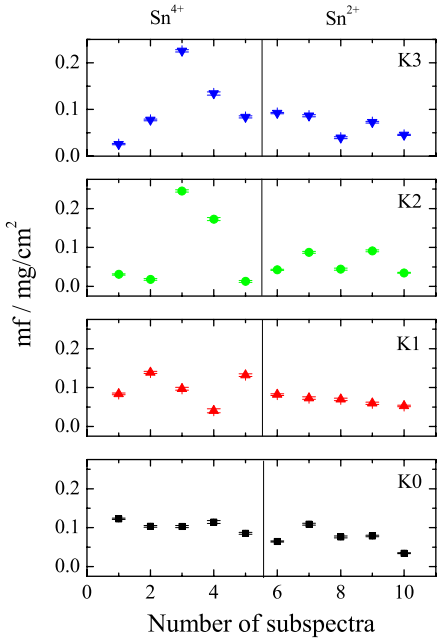

Figure 6.4: Relative intensities of the ten subspectra. Subspectra one to five belong to Sn^{4+}, whereas six to ten correspond to Sn^{2+}. The glass types are given in black squares, the material after nucleation is plotted in red triangles, the high quartz solid solution in green dots and the keatit solid solution in blue triangles.

For the original glass sample (K0) and the material after nucleation (K1), all lines for both sites show the same relative intensity. This means that the five proposed environments for each site are present equivalently. In the high quartz glass ceramic samples the relative intensities of two of the five Sn^{4+} lines are higher at the expense of the other three lines. In the keatit phase one main Sn^{4+} environment is present and three others are little populated. In the high quartz solid solution two environments are high populated and the other three can be neglected. That makes the keatit Sn^{4+} line more broad than the Sn^{4+} line of high quartz. At the Sn^{2+} sites these effects can not be seen so pronounced.

In Figure 6.5 the isomer shift and the quadrupole splitting are plotted for the ten subspectra. Lines one to five belong to Sn^{4+} and lines six to eleven belong to Sn^{2+}.

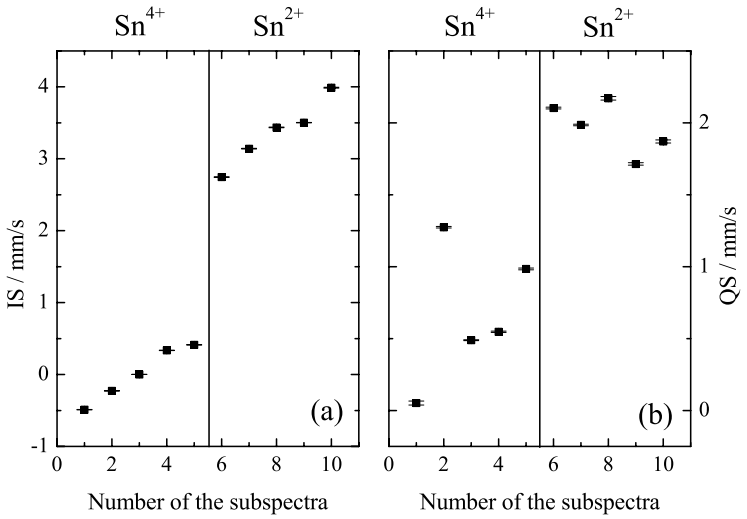

Figure 6.5: Isomer shift (a) and quadrupole splitting (b) for the ten subspectra.

The differences between the five clusters of each site is always the number of Sn–O–Si and Sn–O–Li bondings. It shifts form 4:0 to 0:4 as shown in Figures 6.2 and 6.3. As Li is an electro-positive element, it shifts electron density to its neighbours. That results in a shift of the electron density at the nucleus, which effects the isomer shift. This behaviour can clearly be seen in Figure 6.5, where the isomer shift increases linearly. Additionally, subspectrum number one can be attributed to the Sn^{4+}-cluster with four Sn–O–Si bonds and subspectrum number five to the one with four Sn–O–Li bonds. For Sn^{2+} an increase in electron signals increasing p-electron density. This has the effect of increasing the shielding of the s-electrons, which in turn leads to a decrease of electron density at the nucleus. So subspectrum number six can be allocated to the Sn^{2+} cluster with four Sn–O–Li bonds and sub spectrum number ten to the one with four Sn–O–Si bonds. The quadrupole splitting does not show the same linear behaviour as the isomer shift. It is a function of the electric field gradient and therefore is strongly influenced

by changes in the bond angles and bond lengths of the cluster. So a clear trend cannot be presumed and is also not observed as can be seen in Figure 6.5.

Average isomer shifts and quadrupole splittings for Sn^{4+} and Sn^{2+} in each sample are shown in Table 6.2.

Table 6.2: Average isomer shifts (left) and average quadrupole splittings (right) of the four samples.

	K0	K1	K2	K3		K0	K1	K2	K3
IS / mm/s	-0.02	-0.01	0.09	0.09	QS / mm/s	0.63	0.77	0.52	0.67
IS / mm/s	3.29	3.30	3.34	3.26	QS / mm/s	1.98	1.99	1.93	1.97

The behaviour of the isomer shift can be explained by a change in the lattice structure, which leads to different Debye-Waller-factors. The quadrupole splitting again shows no clear correlation. The average quadrupole splitting and the average isomer shift for the Sn^{2+} site is constant. There are two possible explanations for this fact. First, the local environment of the Sn^{2+} atoms remain unchanged during the transformations. Secondly, the hyperfine parameters of the Sn^{2+} sites are less sensitive to changes in the lattice and the local environment of the atom.

6.4 Summary

Structural changes during the transformation from a glass to a glass ceramic are clearly seen with ^{119}Sn Mössbauer spectroscopy. Hence, the Sn ions are present in ceramic and in the residual glass phase after the thermal treatment. Five environments for each oxidation state are used to describe the spectra. In the glassy sample the ten environments are represented in equal amounts. In the sample after nucleation no drastic changes in comparison to the glasses are seen. In the high quartz and in the keatit sample the relative intensities of the five Sn^{4+} lines are not equal any more, and some environments are preferential.

7 The structure and local surrounding of Fe in $Co_{2-x}Fe_{1+x}Si$

7.1 Introduction

Heusler compounds are known as promising candidates for spintronic applications [67]. Co_2FeSi in particular is well known for its high Curie temperature of 1100 K and its magnetic moment of 6 μ_B in $L2_1$ ordered samples [68]. Inomata *et al.* [69] investigated Co_2FeSi films on a MgO (001) substrate. Using a Co_2FeSi electrode with $L2_1$ structure, they obtained a TMR ratio of 60% at 5 K, significantly smaller than the expected value from half-metallic $L2_1$ ordered Co_2FeSi. Sakuraba *et al.* [70] achieved a decrease in the spin polarisation using Co_2MnSi, a compound with 29 valence electrons. They measured TMR ratios of 570% at 2 K and 67% at 300 K. Tezuka *et al.* [71] found high TMR ratios if using $Co_2FeAl_{0.5}Si_{0.5}$. They measured the TMR ratio of a magnetic tunnel junction consisting of $Co_2FeAl_{0.5}Si_{0.5}$/MgO/$Co_2FeAl_{0.5}Si_{0.5}$ and reported a maximum of 220% at room temperature and 390% at 5 K.

Compounds such as $Co_2Fe_{0.5}Mn_{0.5}Si$ or $Co_2FeAl_{0.5}Si_{0.5}$ with 29.5 valence electrons exhibit a magnetic moment of 5.5 μ_B and seem to be favourable in magneto resistive devices. Most Heusler compounds containing Al show $B2$ disorder [72, 73] due to the low hybridization strength. A possible candidate with 29.5 valence electrons and being free of Al is $Co_{1.5}Fe_{1.5}Si$ as it is isoelectronic to $Co_2FeAl_{0.5}Si_{0.5}$. However, a detailed analysis of the structure is needed to make sure, that the compound is well ordered.

The $T_2T'M$ intermetallics are not only found to crystallise in the $AlCu_2Mn$ structure type ($L2_1$)with O_h symmetry but also in the $CuHg_2Ti$ structure type (X). This formal $TT'TM$ type structure exhibits T_d symmetry and is expected to appear if going from Co_2FeSi to $CoFe_2Si$. It is worthwhile to note that the Co rich alloys with $Co_{2+x}Fe_{1-x}Si$ become hexagonal for $x > 0$ whereas the Fe_3Si end member of the series still has a face centred cubic (fcc) structure. The two structures, $L2_1$ and X, are hardly distinguishable by x-ray diffraction as both have the general fcc symmetry. In addition, the structural determination is aggravated if constituents on equivalent sites have almost the same scattering factors.

The $Co_yFe_{3-y}Si$ ($0 \leq y \leq 3$) system was previously studied by Niculescu *et al.* [74] using nuclear magnetic resonance (NMR), XRD, neutron diffraction, and magnetisation measurements. However, a high degree of disorder was reported for the composition range of $1.6 < y < 2.4$. Wurmehl *et al.* [75] have shown by means of NMR on quaternary Heusler compounds how the analysis of the hyperfine magnetic fields can help to understand the local structure of ordered and disordered systems. Alternatively, the hy-

perfine magnetic fields may also be determined by Mössbauer spectroscopy. Therefore, ^{57}Fe Mössbauer spectroscopy was performed in the present study to explain the local environment and hyperfine magnetic fields of the Fe atoms in $Co_{2-x}Fe_{1+x}Si$ ($0 < x < 1$).

7.2 Experimental details

The $Co_{2-x}Fe_{1+x}Si$ with x = 0.1, 0.2, 0.3, ..., 0.9 samples were prepared as described in the literature [76]. The crystalline structure was determined by x-ray powder diffraction (XRD) as explained in the literature [76] using excitation by Mo K_α radiation. ^{57}Fe Mössbauer spectroscopy at room temperature in transmission geometry was performed for all samples of the series. The XRD data are shown for a comparison with the Mössbauer results.

7.3 Results and Discussion

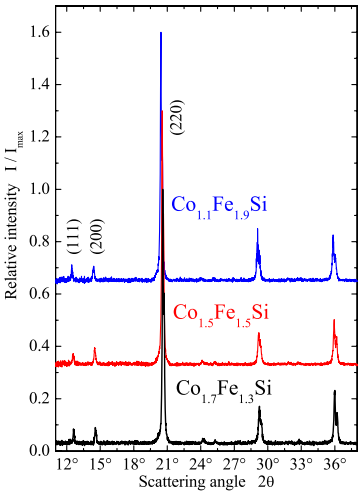

Figure 7.1: Powder diffraction of $Co_{2-x}Fe_{1+x}Si$. Shown are the powder pattern measured with Mo K_α at room temperature for selected compositions with $x = 0.2$, 0.5, and 0.9.

The powder diffraction data of samples with selected composition ($x = 0.2, 0.5$, and 0.9) are presented in Figure 7.1. The (111) and (200) reflections indicate the fcc structure. They are detected for all samples. No significant difference between the XRD patterns can be expected for the cases of the $AlCu_2Mn$ type ($L2_1$, space group no. 225: $Fm\bar{3}m$) or the $CuHg_2Ti$ type (X, space group no. 216: $F\bar{4}3m$) structures that are both fcc. This is due to the similar scattering factors of Co and Fe. Simulated powder diffraction patterns do not resolve any remarkable differences between the two structure types.

The main difference between the $L2_1$ and the X structure is the position of the atoms appearing twice, here Co or Fe. Co_2FeSi adopts the $L2_1$ structure where the two Co atoms occupy the 8c position with local T_d symmetry. The Fe and Si atoms are on the 4a and 4b positions with local O_h symmetry. The next nearest neighbourhood of the Fe atoms consists of eight Co atoms. $CoFe_2Si$ crystallines in the X structure and the Fe atoms occupy the 4a and the 4d positions. The positions of all four atoms have a local T_d symmetry. The next nearest neighbours of the Fe atoms on the 4a position are four Si atoms (4b) and four Fe atoms (4d). The next nearest neighbourhood of the Fe atoms on 4d consists of four Co atoms (4c) and four Fe atoms (4a). Therefore, methods for structural characterisation being sensitive on the local environment - like ^{57}Fe Mössbauer spectroscopy or NMR - are able to distinguish both structure types.

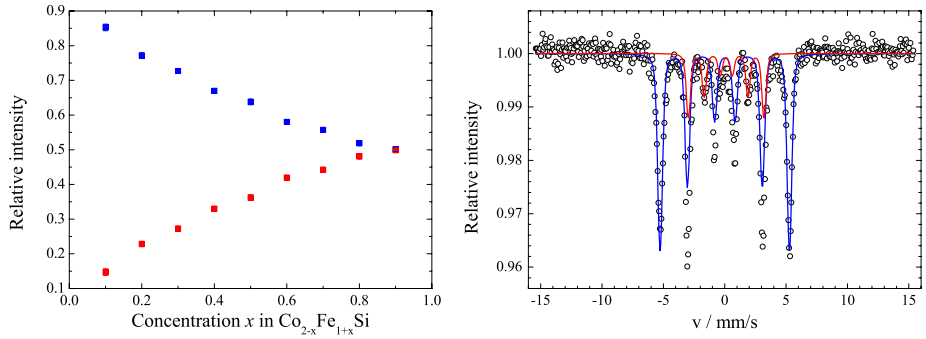

(a) (b)

Figure 7.2: ^{57}Fe Mössbauer spectroscopy of $Co_{2-x}Fe_{1+x}Si$. (a) shows are the relative intensities of the two hyperfine magnetic fields related to the sextets I (blue colour) and II. (red colour). (b) displays the ^{57}Fe Mössbauer spectrum of $Co_{1.8}Fe_{1.2}Si$.

The results from Mössbauer spectroscopy are presented in Figure 7.2. The spectrum of $Co_{1.8}Fe_{1.2}Si$ is shown in the Figure 7.2b. Two different sextets are clearly distinguishable indicating two different hyperfine magnetic fields. The two different hyperfine fields are expected from electronic structure calculations (not shown here) for iron in two different environments. For the two iron atoms in the X-structure, two hyperfine magnetic fields of 164.45 kOe and 271.17 kOe are obtained in calculations. As the lines are always narrow, the 12 lines become distinguishable. This hints on a high crystalline order of the samples. The local environment of the two different Fe sites is significantly different because of the different magnitude of the magnetic splitting. The relative intensities of the two sextets are plotted in Figure 7.2a. For $Co_{1.9}Fe_{1.1}Si$ the relative intensity of sextet I is about 90%. This means that about 90% of the Fe atoms occupy the same position. With increasing Fe content the relative intensities of the two lines converge. This is explained by the fact that the additional Fe atoms are placed on the position that was previously occupied by Co atoms. The sextet, for

which the relative intensity increases with increasing Fe content is the one with the smaller magnetic splitting. It belongs to the Fe atoms which replace Co atoms. The Fe atoms on the 4a position are responsible for the sextet with the larger magnetic splitting. Its relative intensity decreases with increasing Fe content, as the Co atoms on the former 8c position are replaced by Fe atoms and the total Fe content increases. In Co_2FeSi the Fe atoms are placed in a cube of eight Co atoms. As the additional Fe atoms replace the Co atoms, the next nearest environment of the Fe atoms shifts to a cube of four Co and four Fe atoms in $CoFe_2Si$. In both cases atoms with a high magnetic moment surround the central Fe atom and a large hyperfine magnetic field is expected. The next nearest environment of the Fe atoms which replace the Co atoms is a cube of four Fe and four Si atoms. The Si atoms do not carry a magnetic moment and a smaller hyperfine field is detected at the central Fe atom. This demonstrates that the difference in the hyperfine magnetic fields at iron can be explained by accounting only for the next nearest neighbourhood.

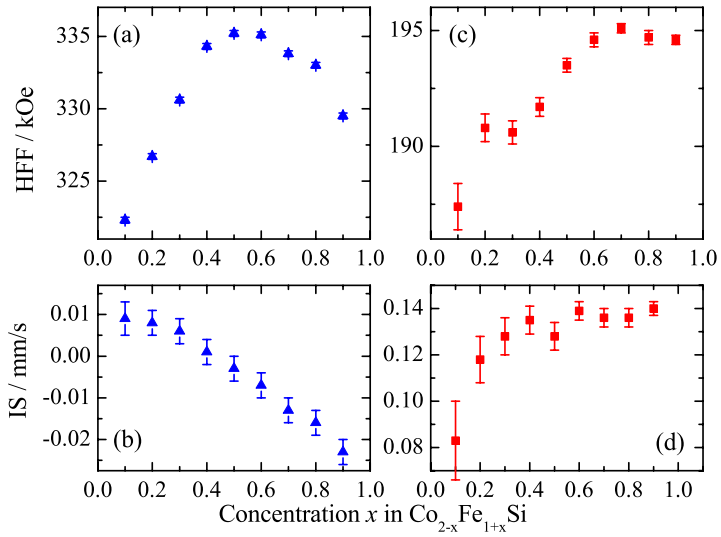

Figure 7.3: Hyperfine parameter of $Co_{2-x}Fe_{1+x}Si$. (a) and (b) show the hyperfine magnetic fields (HFF) and (c) and (d) the isomer shifts (IS) of the two sextets. (a, c) or (b, d) are for sextet I or II, respectively.

The hyperfine splitting and the isomer shifts (IS) are related to the two sextets shown in Figure 7.3. The next nearest neighbourhood of the Fe atoms at the 4a position consists of $(8-4x)$ Co atoms and $4x$ Fe atoms. With increasing Fe content the number of Co atoms decreases from eight to four while the number of Fe atoms increases from zero to four. These changes influence the hyperfine magnetic fields as is seen from Figure 7.3(a) where the hyperfine field (HFF) of sextet I is plotted as function of the additional Fe content x. The isomer shift depends on the electron density at the nucleus.

The concentration dependence of the isomer shift of the Fe atoms on the 4a position is plotted in Figure 7.3(b). As explained above, the environment of the Fe atoms is a cube consisting $(8-4x)$ Co atoms and $4x$ Fe atoms. Therefore, the number of additional Fe atoms in the sample changes the nearest neighbourhood of the Fe atoms directly. With increasing x the number of Fe atoms increases and the number of Co atoms decreases monotonously. As Co has one more valence electron and its electronegativity is higher than the one of Fe, the substitution of Co atoms by Fe atoms changes the electron density close to the central Fe nucleus. That explains the decrease of the isomer shift of sextet I with increasing electron density in Figure 7.3(b). Changes of the hyperfine magnetic field from nuclear magnetic resonance measurements were reported in [74]. They are explained by changes in the next nearest neighbourhood. The Fe atoms on 4d are responsible for sextet II. Their nearest environment remains unchanged while varying the Fe content $(1+x)$. It always consists of four Si and four Fe atoms. For low x, the relative intensity of sextet II is low, as there is only a small number of Fe atoms at the 4d position compared to 100% Fe atoms at the 4a position. That makes the detection of this sextet difficult for small x and increases the uncertainty of the measurement as is seen in the hyperfine magnetic field and the isomer shift of sextet II in Figure 7.3(c) and (d). For $0.2 < x < 1$, the isomer shift of sextet II stays constant within the uncertainty of the measurement. This is expected from the unchanged local environment of the atoms being responsible for sextet II. The hyperfine magnetic field describing sextet II increases with increasing Fe content for $0 < x < 0.5$ and stays constant for higher values of x. The difference of 5 kOe between the lowest and the highest hyperfine fields for $0 < x < 1$ is clearly smaller than the difference of about 15 kOe for sextet I. This also demonstrates the unchanged next and second nearest neighbourhood of those Fe atoms being responsible for sextet II. Changes appear only in the third nearest neighbourhood. The increase of the hyperfine field for $0 < x < 0.5$ is explained by the influences of higher shells. However, the use of Mössbauer spectroscopy made it possible to clearly distinguish between the two Fe sites. As the differences in the next nearest neighbourhood is significant, the difference in the hyperfine magnetic fields for the two Fe sites is large enough to detect two separated sextets in excellent agreement with theory.

7.4 Summary

The presented results clearly show that the combination of Mössbauer spectroscopy and XRD is a powerful tool to determine the structure of crystalline samples. In the solid solution series $Co_{2-x}Fe_{1+x}Si$ with $0 < x < 1$, the samples exhibit similar XRD pattern. Due to the similar scattering factors of Co and Fe the Cu_2MnAl and the $CuHg_2Ti$ structure types are hardly distinguishable. Mössbauer Spectroscopy as a local probe

gives direct access to the local environment of Mössbauer active atoms, and allows to distinguish between closely related structures. In this work, all spectra exhibit two sextets indicating the different environments of the Fe atoms. The changes of the relative intensities makes it possible to relate the two sextets to the definite positions of the crystal lattice. The Fe atom on the 4a position exhibit larger hyperfine fields compared to those on the 4d site. Changes of the hyperfine parameters and their shift with increasing Fe content are explained by differences in the local surrounding of the Fe atoms.

In summary it is shown that the solid solution series $Co_{2-x}Fe_{1+x}Si$ is highly ordered in the range of $0 < x < 1$ as a precondition to make it a promising candidate for spintronic applications.

8 Order and disorder phenomena in $Co_2Mn_{1-x}Fe_xAl$

8.1 Introduction

The study of materials with high spin polarisation is important for application in magnetoelectronic devices using tunnelling magneto-resistive junctions. Heusler compounds have been recognised as perspective materials for spintronics [67]. The Co_2 based Heusler compounds are of special interest for applications because they may possess half-metallic properties and Curie temperatures up to 1100 K [77]. Co_2MnAl is a candidate for half-metallic ferromagnetic behaviour. According to bandstructure calculations the minority spin density almost disappears at the Fermi energy of these compounds [78]. The main condition for half-metallic ferromagnetic behaviour is a regular crystal structure. Highly ordered Heusler alloys crystallise in the $L2_1$ structure type. Mössbauer spectroscopy is a very sensitive tool to study the local structure and hyperfine fields. In this study it is used for the analysis of order and disorder phenomena in $Co_2Mn_{1-x}Fe_xAl$.

8.2 Experimental

Solid solutions $Co_2Mn_{1x}Fe_xAl$ (x = 0, 0.1,, 1) were prepared as explained in the literature [76]. Structural characterisation was performed with powder x-ray diffraction (XRD) [76]. The local environment and hyperfine magnetic fields on the iron atoms were studied by ^{57}Fe Mössbauer spectroscopy in transmission geometry at room temperature using a ^{57}Co(Rh) source. The theoretical investigation was done by using the CPA method with an exchange correlation functional introduced by Vosco, Wilk and Nussair within the generalised gradient approximation [79, 80, 81]. The results are shown for a comparison with the Mössbauer data.

8.3 Results and Discussion

All samples exhibit the same structure as revealed in the powder pattern. All patterns show a main reflection at $2\Theta \approx 20°$ and a smaller at a lower scattering angle of $2\Theta \approx 14°$. For an $L2_1$ or DO_3 structure one would expect an additional super structure peak at $2\Theta \approx 12°$ whereas the reflection at $2\Theta \approx 14°$ would vanish in an alloy with $A2$ structure. Therefore, the pattern can be attributed to the $B2$ structure type. A clear indication as to what atoms are mixed in this CsCl-like structure can, however, not been given

due to the nearly equal scattering factors of Mn, Fe, and Co for Mo K_α radiation. From the Rietveld analysis, a mixture of Fe/Mn atoms with Al atoms seems to be most probable, even though small amounts of a remaining $L2_1$ like order or an additional $A2$ like disorder cannot be excluded. It should be mentioned that there are no impurities or other, foreign phases detected in the samples.

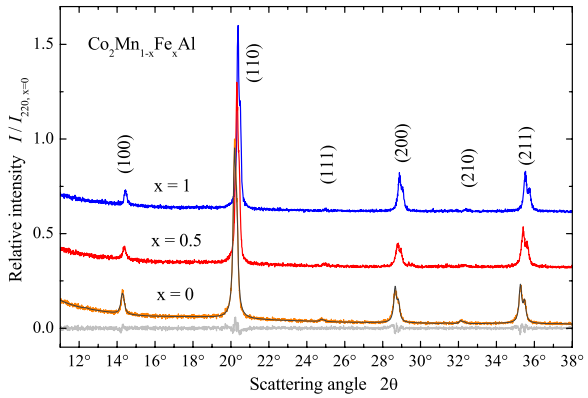

Figure 8.1: Powder XRD of $Co_2Mn_{1-x}Fe_xAl$. Shown are the powder pattern for $x = 0, 1/2$, and 1. The indexing of the reflections is for the $P\,m\overline{3}m$ symmetry of the $B2$ structure. For $x = 0$, the difference between experiment and fit is shown in addition. The intensities for $x = 1/2, 1$ are plotted with an offset.

In Figure 8.2, ^{57}Fe-Mössbauer spectra of the samples with x = 1 to x = 0.2 are shown.

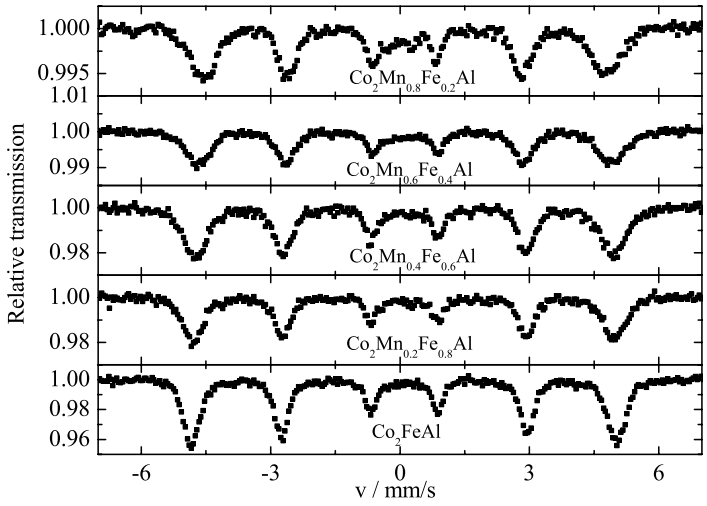

Figure 8.2: ^{57}Fe Mössbauer spectra of $Co_2Mn_{1-x}Fe_xAl$. The Fe content increases from $x = 0.2$ in (a) to $x = 1$. The spectra were taken at room temperature in transmission geometry.

They all exhibit the expected magnetic sextet. Remarkably is the line broadening of the sextet, which is a hint for a distribution of the hyperfine fields caused by different magnetic sites. The nearest and next nearest atoms from the Fe atoms in $L2_1$ ordered $Co_2Mn_{1-x}Fe_xAl$ are presented in Figure 8.3.

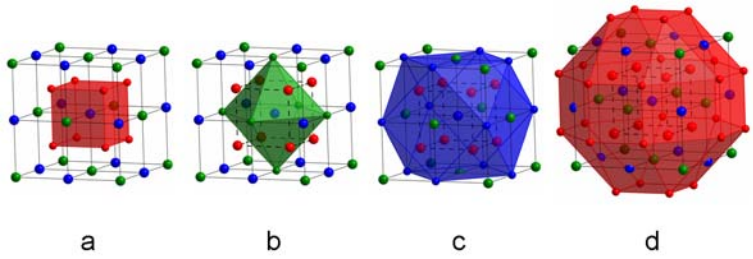

Figure 8.3: Coordination polyhedra of the Fe atoms in the $L2_1$ structure. (a) 1^{st} shell: cubus with 8 Co atoms, (b) 2^{nd} shell: octahedron with 6 Al atoms, (c) 3^{rd} shell: cuboctahedron with 12 $MnorFe$ atoms, (d) 4^{th} shell: rhombicube octahedron with 24 Co atoms.

In $B2$ and $L2_1$ structure type, the next nearest neighbours of any Fe atom are eight Co atoms. The second nearest neighbours are six atoms that form an octahedral environment. For $L2_1$ type these six atoms are Al atoms. For $B2$ type Al atoms can be replaced by magnetic atoms and form seven possible octahedral environments for the Fe atoms. As Al atoms can be replaced by Mn or by Fe atoms the number of possible second nearest neighbourhoods increases again. The number of possible configurations depends on the number of replaced Al atoms. Therefore, for the analysis of the Mössbauer spectra hyperfine magnetic fields $H(i)$ and linewidths $G(i)$ in the calculation model are defined as follows:

$$\begin{aligned} H(i) &= H_0 + i\Delta H \\ G(i) &= G_0 + i\Delta G \end{aligned} \tag{8.1}$$

where the amount of magnetic atoms i in the second nearest neighbourhood changes from 0 to 6. The spectra shown in Figure 8.2 are fitted with the theory explained above and the results are demonstrated in Table 8.1.

Table 8.1: Fitting results

Fe-content x	IS / mm/s	H/ kOe	Δ H/ kOe	G/ mm/s	Δ G/ mm/s
0.2	0.111(4)	288.8(1.5)	11.0(0.7)	0.8(0.8)	0.2(0.2)
0.3	0.115(4)	290.2(3.7)	13.0(1.8)	1.3(1.0)	0.2(0.2)
0.4	0.113(4)	292.7(2.2)	13.3(1.0)	0.9(1.0)	0.3(0.2)
0.5	0.109(4)	295.1(4.6)	12.8(1.5)	1.4(1.2)	0.3(0.3)
0.6	0.108(4)	298.6(2.1)	12.9(0.9)	1.1(1.9)	0.2(0.2)
0.7	0.103(4)	296.9(6.4)	9.2(1.4)	1.6(1.1)	0.1(0.2)
0.8	0.097(4)	297.1(3.9)	9.5(0.9)	1.7(1.1)	0.1(0.2)
0.9	0.100(3)	299.5(9.2)	6.0(1.7)	1.7(0.9)	0.1(0.2)
1	0.098(2)	298.3(10.0)	7.5(1.6)	1.6(1.7)	0.01(0.2)

Figure 8.4 shows the spectra of the samples with x = 0.2, 0.4, 0.6, 0.8 and 1 with the seven subspectra included. For samples with x = 0.2 - 0.5 an additional doublet appears. Here a small content of a second paramagnetic phase, which is not detected by XRD is found. The model provides a good fit to the spectra.

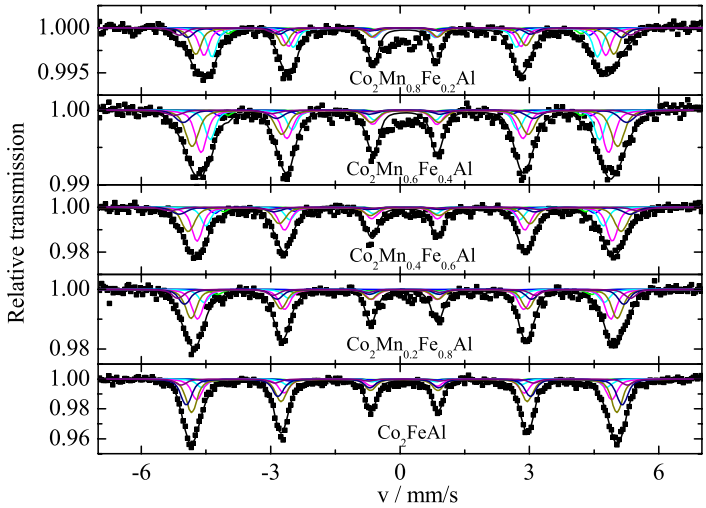

Figure 8.4: ^{57}Fe Mössbauer spectra of $Co_2Mn_{1-x}Fe_xAl$ with x = 0.2; 0.4, 0.6, 0.8, 1 with included subspectra.

Noticeably the subspectrum with maximum intensity is not in the middle in every spectrum, with increasing iron content it shifts to lines with higher hyperfine magnetic fields. This means, the most realized environment is not the octahedron with 3 Al and 3 Mn / Fe atoms, as it would be for the B2 case.

That maybe explained by a coexistence of the $L2_1$ and the $B2$ structure type in $Co_2Mn_{0.1}Fe_{0.9}Al$.

Figure 8.5 summarises the hyperfine parameters from the fit of the Mössbauer spec-

tra. Here the magnetic hyperfine splitting (centre line $H_c = H(i = 3)$), the distances between the magnetic lines (ΔH) and the Gaussian broadening (G and ΔG) as function of the iron concentration x are compared. Additionally, the mean hyperfine field of the distribution H_m is shown in Figure 8.5(a).

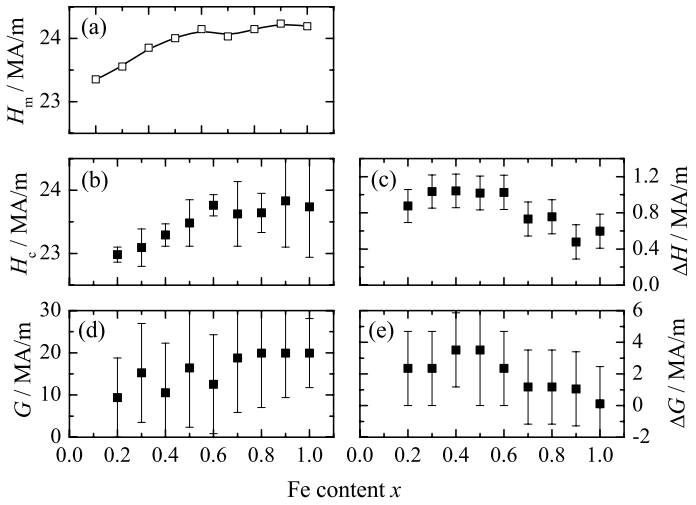

Figure 8.5: Hyperfine field parameter of the Mössbauer spectra of $Co_2Mn_{1-x}Fe_xAl$ as a function of the Fe concentration x. Displayed here are the centre line magnetic hyperfine field $H_c = H(i = 3)$ (b) , the distance between magnetic lines ΔH (c), the Gaussian broadening G (d), and the increase parameter of the Gaussian broadening ΔG (e). (a) shows, in addition, the mean hyperfine field H_m of the distributions.

Figures 8.5(b) and 8.5(c) summarise the hyperfine field of the central line ($H_c = H(i = 3)$) and the distance between to neighbouring lines (ΔH), respectively. The hyperfine field related to the centre line increases with increasing iron content. The slope changes at $x = 0.6$ and H_c is nearly constant at high iron concentration. The Gaussian broadening G of the magnetic lines is in the same order of magnitude as the splitting ΔH. It exhibits a slight, nearly linear increase with the iron concentration. The width of the hyperfine field distributions is, however governed by ΔH. The lower values of ΔH at high iron concentration results in the narrowing of the distributions with increasing iron concentration. The parameter ΔG decreases with x and vanishes in Co_2FeAl. This is as expected because no Mn attributed components of the hyperfine field appear at $x = 1$.

The mean hyperfine field (H_m) shown in Figures 8.5(a) should be comparable to the calculated hyperfine fields. It should be noted, however, that the calculated values are for a surrounding in an effective mean magnetic medium rather than for discrete local neighbourhoods. In the $L2_1$ case the calculated hyperfine field exhibits an overall increase with increasing iron content and is rather constantly close to $x = 0.5$. In

the $B2$ case it increases between 0 and $x = 0.7$ and decreases again for higher iron concentrations. The behaviour of the mean hyperfine field observed in the experiments is just in between these cases.

Besides the hyperfine field parameter, the spectra provide the isomer shift (δ). The values of the isomer shifts obtained from each spectrum are plotted in Figure 8.6(a) as a function of the Fe concentration x. It is obvious that the isomer shift decreases with increasing iron content. The isomer shift is related to the electron density $|\psi(0)|^2$ at the nucleus of the absorber atom (A) with respect to that of the source (S). In case of ^{57}Fe a lower isomer shift corresponds to a higher electron density at the nucleus because the nuclear factor ($R_e^2 - R_g^2 < 0$) is negative for iron atoms:

$$\delta \propto \left\{ |\psi(0)|_A^2 - |\psi(0)|_S^2 \right\} \left\{ R_e^2 - R_g^2 \right\}. \tag{8.2}$$

The increase of the electron density at the Fe nucleus is seen in Figure 8.6(b) where the calculated electron density is plotted as function of the iron concentration. The increasing trend is observed in all calculations independent of the exchange-correlation functional (LSDA or GGA) or structure ($B2$ or $L2_1$).

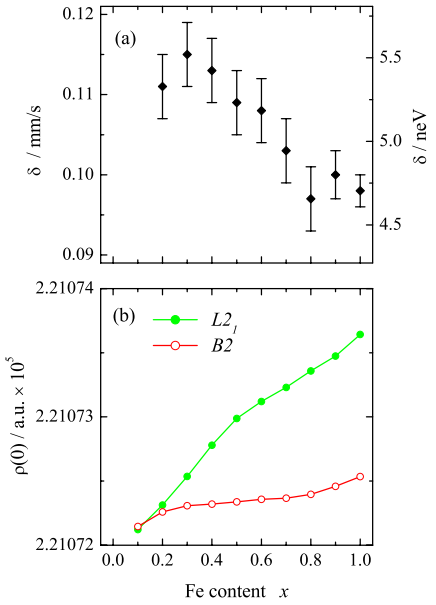

Figure 8.6: Isomer shift and calculated electron density at the Fe nucleus. (a) Shows the isomer shift δ and (b) compares the calculated electron density at the Fe nucleus for the $L2_1$ and $B2$ structures using LSDA calculations. (a.u. = atomic units, here: Bohr radius a_{0B}, $r_0 = 10^{-6} a_{0B}$.

The higher electron density at the Fe nucleus with increasing iron content is explained by the fact that the substitution of Mn by Fe results in electron doping. Fe has one d

electron more than Mn, but both have the same electronegativity. If a single Mn atom is substituted by Fe, the Mn atoms in the surrounding attract part of the Fe electrons resulting in a lower electron density at the Fe probe atom. As the Fe content increases, more Fe sites with Fe in the surrounding appear resulting in an increase of the electron density at the probe Fe atoms and thus in the observed decrease of the isomer shift.

8.4 Summary

All $Co_2Mn_{1-x}Fe_xAl$ with x = 0, 0.1, 0.2, , 1 reveal a cubic structure in XRD measurements. Differences between $B2$ and $L2_1$ are hardly distinguishable here. That is due to the nearly equal scattering factors of Mn, Fe, and Co for Mo K_α radiation. ^{57}Fe Mössbauer spectra show a typical magnetic sextet with broad lines. The broadening of the lines indicates a distribution of magnetic environments at the Fe atoms in the second coordination sphere. The analysis is performed using a model of seven magnetic environments, arising from the $B2$ disorder in a $L2_1$ structure type. The relative intensities of the seven hyperfine magnetic fields are explained by the appearance of a mixture of $B2$ and $L2_1$ structure in samples with $x > 0.8$. The behaviour of the isomer shift and hyperfine magnetic field with increasing iron content is qualitatively explained by band structure calculations based on the CPA method [79, 80, 81].

9 Summary and outlook

Summary

Mössbauer spectroscopy has proved to be an invaluable tool for the determination of oxidation states and for the analysis of local ordering phenomena of Mössbauer active atoms. As it is a local probe translational symmetry is of no importance and crystalline as well as amorphous materials may be investigated. In such crystalline materials it can be used in conjunction with x-ray diffraction. The combination of local and global probing enables the study of ordering effects in statistically occupied positions in a well ordered matrix. This technique was utilised in this work to investigate the local surrounding of Fe atoms in the two series of Heusler compounds $Co_{2-x}Fe_{1+x}Si$ and $Co_2Mn_{1-x}Fe_xAl$. For the $Co_2Mn_{1-x}Fe_xAl$ series a $L2_1$ ordered phase in the overall $B2$ ordered samples was detected. A change from the $AlCu_2Mn$ to the $CuHg_2Ti$ structure type for the $Co_{2-x}Fe_{1+x}Si$ samples was found.

The transformation of a glass to a ceramic material was studied with ^{119}Sn Mössbauer spectroscopy. The higher ordering in ceramics was found to be attended by decreasing Mössbauer linewidths. Hence, the modifications of the Sn environments display clearly the transformation of the whole material.

When the local environment of infrequently occurring atoms in an amorphous matrix is the subject of interest, local probing methods are the most reliable methods available. In the work presented here, ^{119}Sn Mössbauer spectroscopy was used to determine the oxidation state, the local surrounding and the relative intensities of the tin atoms in a silicate matrix. Thermal treatment experiments were performed with glasses containing 0.1 wt% SnO_2 to 0.5 wt% SnO_2. At the same time process determining parameters such as the oxygen partial pressure, the temperature, the treatment duration and the cooling procedure were varied. These parameters determine the final product in the industrial glass manufacture with the float process. In the float chamber temperatures up to 1200 °C and oxygen partial pressures of about $1{\cdot}10^{-12}$ bar appear. Under these conditions various reduction and diffusion processes can take place, particularly at the tin-melt and at the melt-atmosphere boundary. This causes defects at the glass surfaces which may ruin the final product. However, such damage to the matrix originates from very slight modifications of the coordination and the oxidation state of the tin atoms. To investigate these fine changes in detail the relevant parameters were varied systematically in a methodic approach.

For a good quality analysis of the Mössbauer spectra a structural model for the tin species in the glass matrix is required. As the tip of the Mössbauer lines are always asymmetric, at least two lines for each oxidation state are necessary. These

correspond to two different environments for the Sn^{2+} and the Sn^{4+} atoms in the glass matrix. It is assumed that the changes in the relative intensities of the lines are based on varying concentrations of the same structural units. Consequently, all measured spectra are fitted simultaneously with the same set of hyperfine parameters. The local environment of the tin atoms was investigated by comparing these parameters with hyperfine parameters of model substances. For Sn^{2+} a trigonal $[SnO_3]$ pyramid is the only possible mode of coordination, which explains the large quadrupole splitting. Bonding to Ca^{2+} was excluded as the origin of the difference between the two Sn^{2+} coordinations. A varying number of bonding and non-bonding oxygen atoms have to be due to coordinations to Al or B (see Figure 9.1c and 9.1d). The coordination number of the Sn^{4+} ions in the glass matrix could not be definitely determined. The symmetric Sn^{4+} line is postulated to corresponds to a tetrahedral (see Figure 9.1b) and the asymmetric to an octahedral (see Figure 9.1a) environment.

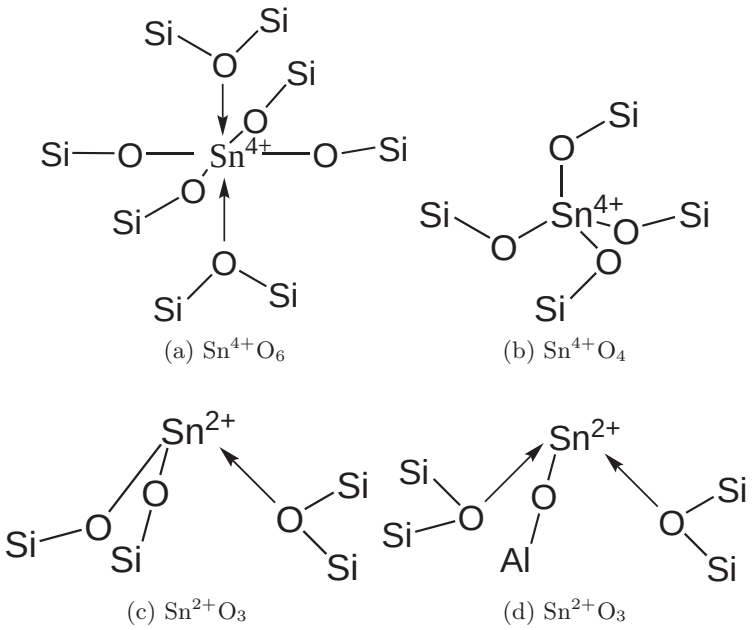

(a) $Sn^{4+}O_6$ (b) $Sn^{4+}O_4$

(c) $Sn^{2+}O_3$ (d) $Sn^{2+}O_3$

Figure 9.1: Presumed Sn coordinations.

The described experiments are finally used to develop a reaction and diffusion model. A two dimensional model is successfully used to describe the Mössbauer relative intensities. All gained data was fitted to the same set of diffusion and transfer coefficients, as shown in Table 9.1.

The expected order of magnitude of these diffusion coefficients are in agreement with the literature values (see Appendix). In contrast to expectations the presented diffusion coefficient for Sn^{4+} was found to be larger than for Sn^{2+}. This in turn can be rationalised by taking the electron hopping processes into account. The mass trans-

fer coefficient k_c is smaller than the estimated value, but still in the same order of magnitude.

Table 9.1: Fitting results of the diffusion experiments.

D_2	$5 \cdot 10^{-7}$ cm^2/s
D_4	$5 \cdot 10^{-6}$ cm^2/s
k_c	$5 \cdot 10^{-8}$ m/s

A graph displaying the reaction and diffusion processes is presented in Figure 9.2. At the atmosphere-glass interface the oxygen partial pressure of the gas determines the Sn^{2+}/Sn^{4+} ratio in the melt. Additionally Sn^{2+} can evaporate as SnO as long as the atmosphere above the melt is not saturated with SnO. Inside the glass the Sn^{2+} ions can be considered as mobile, but charge equalisation has to be respected, therefore a diffusion of Ca^{2+} ions in the opposite direction is assumed to be taking place, as displayed in Figure 9.2. Because of the high diffusion coefficient it can not be assumed that the Sn^{4+} ions move through the melt, therefore, electron hopping processes are used to transfer the charge, as in Figure 9.2.

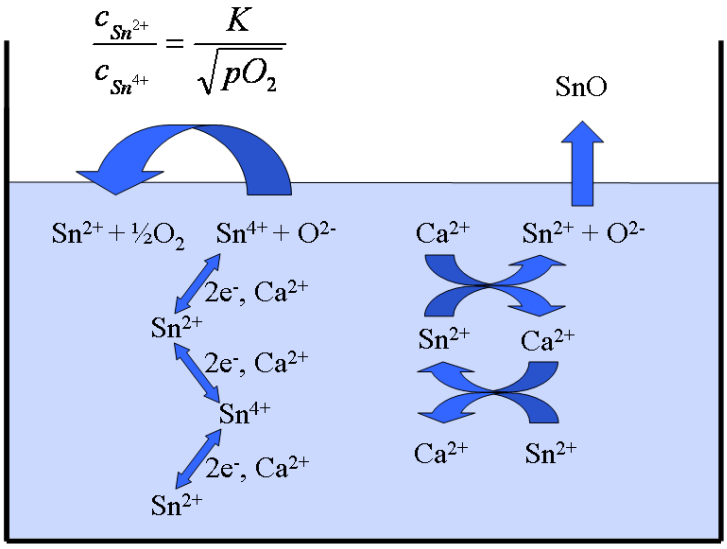

Figure 9.2: Reaction and diffusion model

Outlook

Wherever local ordering phenomena on materials containing Mössbauer active atoms are the subject of interest Mössbauer spectroscopy has been shown to be an extremely powerfull tool. The possibility to perform oxidation state selective investigations makes the method even more attractive. As translational symmetry is not a prerequisite amorphous materials and glasses nay also be investigated.

In this work a structural model for the tin environments in a special designed model glass was described, whereby Mössbauer relative intensities were used to generate a reaction and diffusion model. This allowed for the assignment of the Sn^{2+} and Sn^{4+} coefficients. Thus it is shown that an examination of the chemistry of tin in silicate glasses with Mössbauer spectroscopy is possible. This knowledge may be further expanded upon in the future to support the development of new glasses or to study questions in connection with the float process. Additionally. ceramisation processes were successfully examined with Mössbauer spectroscopy, thus here is opening another interesting field of research where Mössbauer spectroscopy may contribute.

The nearest and next nearest environments of the tin atoms in silicate glasses may additionally be investigated with the NMR method. Here many atoms in the model glass can be studied and the connectivity may be clarified with two-dimensional measurements. To improve of the reaction and diffusion model an increase of the number of data points is necessary. Diffusion experiments in more reducing atmospheres for shorter treatment time come closer to the float conditions. Additional variations of the probing depth may also help to increase the accuracy of the determined diffusion coefficients.

In this thesis we have successfully demonstrated the multifaceted applicability of Mössbauer spectroscopy. It has been thereby shown that this technique will prove to be an invaluable tool in future investigations into ordering effects of inorganic materials.

List of Publications

- The structure and local surrounding of Fe in $Co_{2-x}Fe_{1+x}Si$
  Verena Jung, Benjamin Balke, Gerhard H. Fecher and Claudia Felser
  Appl. Phys. Lett. 93, 042507 (2008)

- Mössbauer spectroscopy of $Co_2Mn_{1-x}Fe_xAl$
  Verena Jung, Benjamin Balke, Gerhard H. Fecher, Vadim Ksenofontov and Claudia Felser
  Hyperfine Interactions 184, 15-21 (2008)

- Tin in silicate glasses: structure, thermodynamics and kinetics
  Verena Jung, Vadim Ksenofontov, Maria-Louisa Aigner, Thomas Pfeiffer, Dirk Sprenger and Claudia Felser
  Hyperfine Interactions 183, 215-220 (2008)

- Electronic structure, magnetic properties, and order-disorder phenomena in $Co_2Mn_{1-x}Fe_xAl$
  Verena Jung, Gerhard H. Fecher, Benjamin Balke, Vadim Ksenofontov and Claudia Felser
  J. Phys. D.: Appl. Phys. accepted

Thermodynamic data

composition	Δ H / kJ/mol	Δ S J/K mol
SiO_2-Al_2O_3-B_2O_3-Na_2O-K_2O-MgO-CaO-BaO [17]	174	80
SiO_2-B_2O_3-Na_2O-K_2O [17]	145	53
SiO_2-Al_2O_3-B_2O_3-Na_2O-MgO [17]	177	79
SiO_2-B_2O_3-Li_2O-Na_2O-MgO-La_2O_3-ZrO_2 [18]	194	109
85 SiO_2 - 15 Na_2O [19]	232	107
80 SiO_2 - 20 Na_2O [21]	226	105
74 SiO_2 - 26 Na_2O [19]	238	111
67 SiO_2 - 33 Na_2O [22]	216	99
80 SiO_2 - 10 Na_2O - 10 CaO [19]	196	91
74 SiO_2 - 16 Na_2O - 10 CaO [19]	214	99
70 SiO_2 - 20 Na_2O - 10 CaO [19]	208	95
64 SiO_2 - 26 Na_2O - 10 CaO [19]	212	95
74 SiO_2 - 16 Li_2O - 10 CaO [20]	204	95
74 SiO_2 - 16 Na_2O - 10 CaO [20]	214	99
74 SiO_2 - 16 K_2O - 10 CaO [20]	268	131
74 SiO_2 - 16 Na_2O - 10 MgO [20]	208	97
80 SiO_2 - 0 Al_2O_3 - 10 Na_2O - 10 CaO [23]	196	91
75 SiO_2 - 5 Al_2O_3 - 10 Na_2O - 10 CaO [23]	200	93
65 SiO_2 - 15 Al_2O_3 - 10 Na_2O - 10 CaO [23]	156	81
55 SiO_2 - 25 Al_2O_3 - 10 Na_2O - 10 CaO [23]	68	35
74 SiO_2 - 0 Al_2O_3 - 16 Na_2O - 10 CaO [23]	214	99
69 SiO_2 - 5 Al_2O_3 - 16 Na_2O - 10 CaO [23]	204	97
64 SiO_2 - 10 Al_2O_3 - 16 Na_2O - 10 CaO [23]	196	93
59 SiO_2 - 15 Al_2O_3 - 16 Na_2O - 10 CaO [23]	178	87
49 SiO_2 - 25 Al_2O_3 - 16 Na_2O - 10 CaO [23]	160	77
70 SiO_2 - 10 Al_2O_3 - 10 CaO - 10 BaO [24]	169	83
65 SiO_2 - 15 Al_2O_3 - 10 CaO - 10 BaO [24]	169	83
SiO_2-Al_2O_3-Li_2O-Na_2O-K_2O-MgO-CaO-ZnO-V_2O_3-TiO_2-ZrO_2 [25]	146	94
SiO_2-Al_2O_3-B_2O_3-P_2O_3-Li_2O-Na_2O-K_2O-BaO-TiO_2-ZrO_2 [25]	142	71
SiO_2-Al_2O_3-P_2O_3-Li_2O-Na_2O-K_2O-MgO-ZnO-TiO_2-ZrO_2 [25]	146	71
SiO_2-Al_2O_3-B_2O_3-MgO-CaO-BaO [25]	150	70
SiO_2-Al_2O_3-B_2O_3-MgO-CaO-BaO [25]	156	74
SiO_2-Al_2O_3-B_2O_3-Li_2O-Na_2O-K_2O-ZnO-TiO_2[25]	180	85
8.5 Na_2O - 15 Al_2O_3- 76.5 SiO_2 [16]	101	63
11 Na_2O - 15 Al_2O_3- 74 SiO_2 [16]	85	59
16 Na_2O - 15 Al_2O_3- 69 SiO_2 [16]	93	51

composition	atom	T / ^oC	D / cm^2/s
8.5 Na_2O - 15 Al_2O_3- 76.5 SiO_2 [16]	Sn	1500	$3.55 \cdot 10^{-7}$
11 Na_2O - 15 Al_2O_3- 74 SiO_2 [16]	Sn	1500	$3.02 \cdot 10^{-7}$
16 Na_2O - 15 Al_2O_3- 69 SiO_2 [16]	Sn	1500	$3.24 \cdot 10^{-7}$
15 Na_2O - 85 SiO_2 [22]	Sn^{2+}	1300	$1.4 \cdot 10^{-8}$
SiO_2-Al_2O_3-B_2O_3-MgO-CaO-BaO [25]	Sn + Fe	1400	$7.57 \cdot 10^{-7}$
SiO_2-Al_2O_3-B_2O_3-MgO-CaO-BaO [25]	Sn^{2+}/Sn^{4+}	1400	$2.83 \cdot 10^{-8}$
74 SiO_2 - 16 Na_2O - 10 CaO [82]	Sn^{4+}	1000	$1.2 \cdot 10^{-7}$

Parameters used in the WIEN2k calculations

The following parameter are used for the Wien2k calculations of one example structure. All others are set equivilantly.

space group	1 (P1)
R0(Sn)	0.00000001
number of plane waves	7.00
GMAX	25
number of k-points	1
muffin tin radius for Sn	2.4
muffin tin radius for O	1.2
muffin tin radius for Si	1.9
muffin tin radius for H	0.65
lattice constant	17.557068

atom number	atom	position
1	Sn	X=0.52572000 Y=0.39401000 Z=0.44105000
2	O	X=0.39970000 Y=0.29248000 Z=0.58588000
3	Si	X=0.50818000 Y=0.28616000 Z=0.73233000
4	O	X=0.64984000 Y=0.20696000 Z=0.38789000
5	Si	X=0.77421000 Y=0.29854000 Z=0.28245000
6	O	X=0.40650000 Y=0.42964000 Z=0.27080000
7	Si	X=0.41971000 Y=0.63813000 Z=0.24915000
8	O	X=0.41692000 Y=0.21530000 Z=0.87693000
9	O	X=0.57446000 Y=0.47795000 Z=0.76766000
10	O	X=0.64687000 Y=0.15525000 Z=0.70254000
11	O	X=0.90625000 Y=0.16056000 Z=0.24702000
12	O	X=0.84526000 Y=0.46577000 Z=0.36622000
13	O	X=0.69885000 Y=0.35911000 Z=0.12638000
14	O	X=0.35280000 Y=0.73698000 Z=0.39384000
15	O	X=0.32612000 Y=0.69769000 Z=0.10288000
16	O	X=0.59275000 Y=0.69458000 Z=0.22948000
17	H	X=0.37751000 Y=0.10958000 Z=0.83908000
18	H	X=0.62137000 Y=0.45694000 Z=0.86123000
19	H	X=0.60006000 Y=0.06458000 Z=0.64767000
20	H	X=0.93086000 Y=0.12388000 Z=0.34541000
21	H	X=0.85253000 Y=0.54407000 Z=0.28428000
22	H	X=0.66494000 Y=0.25080000 Z=0.08833000
23	H	X=0.36574000 Y=0.85451000 Z=0.36426000
24	H	X=0.24247000 Y=0.62200000 Z=0.10932000
25	H	X=0.60807000 Y=0.66273000 Z=0.12778000
26	Si	X=0.24084000 Y=0.40509000 Z=0.61401000
27	O	X=0.27953000 Y=0.60236000 Z=0.67615000
28	O	X=0.14685000 Y=0.41927000 Z=0.45530000
29	O	X=0.13594000 Y=0.30336000 Z=0.73846000
30	H	X=0.18443000 Y=0.65458000 Z=0.69323000
31	H	X=0.06304000 Y=0.49103000 Z=0.47800000
32	H	X=0.12150000 Y=0.19024000 Z=0.69768000

List of Figures

List of Tables

Bibliography

[1] R.H. Doremus. *Glass Science*. Wiley-Interscience, 1973.

[2] H. Scholze. *Glas Natur, Struktur und Eigenschaften*. Springer Verlag, Berlin, 1977.

[3] A. Pilkington. *Proc. Roy. Soc. Lond. A*, 314:1–25, 1969.

[4] http://de.wikipedia.org/wiki/Glas.

[5] A. Pilkington. *The Glass Industry*, pages 80–81, 100–102, 1963.

[6] A. Pilkington. *Glass Technology*, 12:76–83, 1971.

[7] T. Pfeiffer. *Floatbarkeit von Gläsern*. Schott AG, 2006.

[8] N. N. Greenwood and T.C. Gibb. *Mössbauer Spectroscopy*. 1971.

[9] F.E. Wagner and A. Kyek. *Hyperfine Interactions*, 154:5–33, 2004.

[10] M. Faraday. *Phil. Trans. Roy. Soc.*, 49, 1830.

[11] M. Faraday. *Phil. Mag.*, 14:512, 1857.

[12] W. Vogel. *Glaschemie*. Deutscher Verlag für Grundstoffindustrie, Berlin, 1979.

[13] W.H. Zachariasen. *Journal of the American Chemical Society*, 54:3841–3852, 1932.

[14] B.E. Warren and co workers. *J. Am. Ceram. Soc.*, 17:249, 1934.

[15] A.C. Hannon, B. Vessal, and J.M. Parker. *J. Non-Cryst. Solids*, 150:97–102, 1992.

[16] H. Schirmer and Rüssel. C. *J. Non-Cryst. Solids*, 354:889–895, 2008.

[17] A Matthai, D Ehrt, and C Rüssel. *Glass Science and Technology-Glastechnische Berichte*, 73(2):33–38, 2000.

[18] O. Claussen and C. Rüssel. *J. Non-Cryst. Solids*, 209(3):292–298, 1997.

[19] D. Benne, C. Rüssel, O. Lehmann, M. Menzel, D. Niemeier, and K.D. Becker. *J. Non-Cryst. Solids*, 318(1-2):202–212, 2003.

[20] D Benne and C Rüssel. *Glass Science and Technology*, 76(3):130–135, 2003.

[21] D. Benne and Rüssel. *J. Non-Cryst. Solids*, 351:1283–1288, 2005.

[22] G von der Gonna and C Rüssel. *J. Non-Cryst. Solids*, 272(2-3):131–138, 200.

[23] D. Benne, C. Rüssel, M. Menzel, D. Niemeier, and K.D. Becker. *J. Non-Cryst. Solids*, 345-346:203–207, 2004.

[24] G von der Gönna and C Rüssel. *J. Non-Cryst. Solids*, 288(1-3):175–183, 2001.

[25] FTM-2. *Schott AG.*

[26] H. Dannheim, H.J. Oel, and G. Tomandl. *Glastechn. Ber.*, 49:170–175, 1976.

[27] G. Principi, A. Maddalena, A. Gupta, F. Geotti-Bianchini, S. Hreglich, and M. Verità. *Nuclear Instruments and Methods in Physics Research B*, 76:215–217, 1993.

[28] T. Nishida. *J. Non-Cryst. Solids*, 177:257–268, 1994.

[29] J.F. Bent, A.C. Hannon, D. Holland, and M.M.A. Karim. *J. Non-Cryst. Solids*, 232-234:300–308, 1998.

[30] J.A. Johnson, C.E. Johnson, K.F.E. Williams, D. Holland, and M.M Karim. *Hyperfine Interactions*, 95:41–51, 1995.

[31] J.A. Johnson, C.E. Johnson, D. Holland, A. Sears, J.F. Bent, P.G. Appleyard, M.F. Thomas, and A.C. Hannon. *J. Phys.: Condens. Matter*, 12:213–230, 2000.

[32] D. Holland, A.P. Howes, R. Dupree, J.A. Johnson, and C.E. Johnson. *J. Phys.: Condens. Matter*, 15:2457–2472, 2003.

[33] J.A. Johnson, J. Urquidi, D. Holland, C.E. Johnson, and P.G. Appleyard. *J. Non-Cryst. Solids*, 353:4084–4092, 2007.

[34] D. Benne, C. Rüssel, M. Menzel, and K.D. Becker. *J. Non-Cryst. Solids*, 337(3):232–240, 2004.

[35] D.A. McKeown, A.C. Buechele, H. Gan, and L. Pegg. *J. Non-Cryst. Solids*, 352:3142–3151, 2008.

[36] A.J.G. Ellison, P.C. Hess, and G.C. Naski. *J. Am. Ceram. Soc.*, 81:3215, 1998.

[37] M.H. Krohn, J.R. Hellmann, B. Mahieu, and C.G. Pantano. *J. Non-Cryst. Solids*, 351:455–465, 2005.

[38] J.A. Johnson and C.E. Johnson. *J. Phys.: Condens. Matter*, 17:382–412, 2005.

[39] K.F.E. William, C.E. Johnson, J. Greengrass, B.P. Tilley, D. Gelder, and J.A. Johnson. *J. Non-Cryst. Solids*, 211:164–172, 1997.

[40] G. Heide, C. Müller-Fildebrandt, D. Moseler, G.H. Frischat, W. Meisel, A. Maldener, A. Zouine-Thimm, and F. Rauch. *Glastech. Ber. Glass Sci.Technol.*, 73:321–330, 2000.

[41] Y. Hayashi, K. Matsumoto, and M. Kudo. *J. Non-Cryst. Solids*, 282:188–196, 2001.

[42] S. Takeda, R. Akiyama, and H. Hosono. *J. Non-Cryst. Solids*, 281:1–5, 2001.

[43] D. Ehrt. *Phys. Chem. Glasses: Eur. J. Glass Sci. Technol. B*, 49:68–72, 2008.

[44] D. Benne and Rüssel. *Phys. Chem. Glasses: Eur. J. Glass Sci. Technol. B*, 49:160–165, 2008.

[45] Dirk Sprenger. *Spektroskopische Untersuchungen und Berechnungen zur Struktur anorganischer Gläser*. PhD thesis, Johannes Gutenberg-Universität in Mainz, 1996.

[46] H. Spiering, L. Deak, and L. Bottyan. *Hyperfine Interactions*, 125:197, 2000.

[47] B.K. Teo. *EXAFS: Basic Principles and Data Analysis*. Springer, Berlin, 1986.

[48] Matthew Newville. Fundamentals of xafs. *http://xafs.org/tutorials*.

[49] Shelly D. Kelly. Introduction to exafs data analysis. *http://xafs.org/tutorials*.

[50] Matthew Newville. Xafs: X-ray absorption fine-structure. *http://xafs.org/tutorials*.

[51] Hauke Esemann. *Röntgenabsorptions- und Ferninfrarotspektroskopie als kationensensitive Methode zur Untersuchung siliciumreicher Zeolithe*. PhD thesis, Universität Hamburg, 1997.

[52] M. Newville. *J. Synch. Rad.*, 8:322–324, 2001.

[53] Materials Studio 4.1. *Accelrys Inc.; San Diego*, 2006.

[54] H. Sun. *J. Phys. Chem. B*, 102:7338–7364, 1998.

[55] P. Blaha, K. Schwarz, G.K.H. Madsen, D. Kvasnicka, and J. Luitz. *Wien2k, An augmented plain wave + local orbitals program for calculating crystal properties*. Techn. Universität Wien, 2001.

[56] J. P. Perdew, K. Burke, and M. Ernerhof. *Phys. Rev. Lett.*, 77:3865, 1996.

[57] T. Armbruster and R. Oberhänsli. *Am. Mineral.*, 73:595–600, 1988.

[58] P.E. Lippens. *Physical Review B*, 60:4576–4586, 1999.

[59] P.E. Lippens, J. Olivier-Fourcade, and J.C. Jumas. *Hyperfine Interactions*, 126:137–141, 2000.

[60] A. Svane, N. E. Christensen, C. O. Rodriguez, and M. Methfessel. *Physical Review B*, 55:12572 – 12577, 1997.

[61] J. D. Donaldson and A. Jelen. *Journal of the Chemical Society A*, pages 1448–1450, 1968.

[62] J. C. Dewan, J. Silver, J. D. Donaldson, and M. J. K. Thomas. *J.C.S. Dalton*, pages 12319–2322, 1977.

[63] R. Haase. *Transportvorgänge*. Darmstadt, 1973.

[64] S.R. de Groot and P. Mazur. *Non-Equilibrium Thermodynamics*. Amsterdam, 1962.

[65] J. Crank. *The mathematics of diffusion*. 1975.

[66] C. Roos, O. Becker, and F. Siebers. *J Mater Sci*, 42:50–58, 2007.

[67] C. Felser, G.H. Fecher, and B. Balke. *Angewandte Chemie International Edition*, 46:668–699, 2007.

[68] S. Wurmehl, G. H. Fecher, H. C. Kandpal, V. Ksenofontov, C. Felser, H.-J. Lin, and J. Morais. *Phys. Rev. B*, 0506729v4, 2005.

[69] K. Inomata, S. Okamura, M. Kikuchi, N. Tezuka, M. Wojicik, and E. Jedryka. *J. Phys. D: Appl. Phys.*, 39:816–823, 2006.

[70] Y. Sakuraba, M. Hattori, M. Oogane, Y. Ando, H. Kato, A. Sakuma, T. Miyazaki, and H. Kubota. *Applied Physics Letters*, 88:19258, 2006.

[71] N. Tezuka, N. Ikeda, S. Sugimoto, and K. Inomata. *Japanese Journal of Applied Physics*, 46:454–456, 2007.

[72] B. Balke, S. Wurmehl, G. H. Fecher, C. Felser, H.-J. Lin, M. C. M. Alves, F. Bernadi, and J. Morais. *Applied Physics Letters*, 90:172501, 2007.

[73] T. M. Nakatani, A. Rajanikanth, Z. Gercsi, Y. K. Takahashi, K. Inomata, and K. Hono. *Journal of Applied Physics*, 102:033916, 2007.

[74] V. Niculescu, J. I. Budnick, W.A. Hines, and K. Raj. *Physical Review B*, 19:452–464, 1979.

[75] S. Wurmehl, J. T. Kohlhepp, H. J. M. Swagten, B. Koopmans, M. Wojcik, B. Balke, C. G. F. Blum, V. Ksenofontov, G. H. Fecher, and C. Felser. *Applied Physics Letters*, 91:052506, 2007.

[76] Benjamin Balke. *Heulser alloys*. PhD thesis, Johannes Gutenberg-Universität in Mainz, 2007.

[77] S. Wurmehl, G. H. Fecher, H.C. Kandpal, V. Ksenofontov, and C. Felser. *Applied Physics Letters*, 88:032503, 20006.

[78] J. Kübler, A. R. Williams, and C. B. Sommers. *Phys. Rev. B*, 28:1745, 1983.

[79] H. Ebert. volume 535 of *Lecture Notes in Physics*, pages 191 – 246. Springer-Verlag, Berlin, Heidelberg, 1999.

[80] H. Ebert. *The Munich SPR-KKR package, Version 3.6*. http://olymp.cup.uni-muenchen.de/ak/ebert/SPRKKR. 2005.

[81] H. Ebert, J. Minar, and V. Popescu. volume 580 of *Lecture Notes in Physics*, pages 371 – 385. Springer-Verlag, Berlin, Heidelberg, 2001.

[82] H. Behrens and M. Haak. *J. Non-Cryst. Solids*, 353:4743–4752, 2007.